Influence of Surface Coating on the Degradation Properties of Metallic Orthopaedic Implants

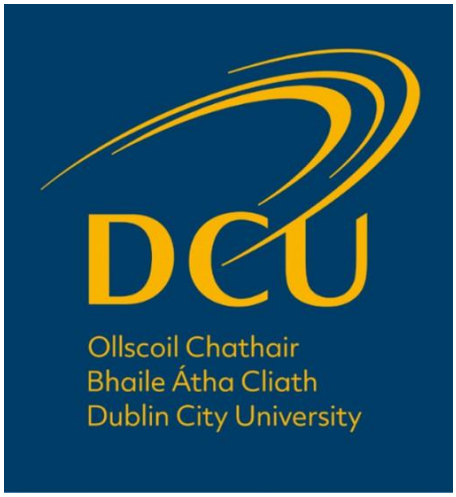

Beth Macaulay, BSc

Submitted for the degree of Master of Engineering

School of Mechanical and Manufacturing Engineering, Dublin City University

Supervised By:

Professor Nicholas Dunne

Dr Tanya Levingstone

January 2025

Declaration

I hereby certify that this material, which I now submit for assessment on the programme of study leading to the award of Master of Engineering, is entirely my own work, and that I have exercised reasonable care to ensure that the work is original, and does not to the best of my knowledge breach any law of copyright, and has not been taken from the work of others save and to the extent that such work has been cited and acknowledged within the text of my work.

Signed: Beth Macaulay

ID: 20215683

Date: 25/8/2025

Table of Contents

Declaration ii

Table of Contents iii

List of Figures vii

List of Tables ix

Abbreviations x

Abstract: Influence of Surface Coatings on the Degradation Properties of Metallic Orthopaedic Implants – Beth Macaulay. 1

Acknowledgements 2

1 Introduction and Literature Review 3

1.1 Bone 4

1.1.1 Structure of the Bone 4

1.1.2 Bone Matrix 5

1.1.3 Bone Cells 6

1.1.4 Osteons 8

1.2 The Bone Remodelling Process 9

1.2.1 Activation 10

1.2.2 Resorption 11

1.2.3 Reversal 11

1.2.4 Formation 11

1.2.5 Termination 11

1.3 Fracture Healing and Repair 13

1.3.1 Indirect Healing 13

1.3.2 Direct Healing 15

1.3.3 Factors Affecting Fracture Healing 17

1.4 Orthopaedic Implants 19
1.4.1 Classification of Orthopaedic Implants 20
1.4.2 Orthopaedic Implant Materials 23
1.4.3 Considerations of Implant Materials 23
1.4.4 Metals 26
1.4.5 Magnesium 28
1.4.6 Ceramics 28
1.4.7 Calcium Phosphate Coatings 30
1.4.8 Octacalcium Phosphate (OCP) 32
1.4.9 Calcium Phosphate Coating Methods 33
1.5 Summary 36
1.6 Project Aims and Objectives 36
2 Materials and Methods 38
2.1 Octacalcium Phosphate Synthesis 38
2.1.1 Synthesis 38
2.1.2 Filtration 39
2.1.3 Weighing 39
2.1.4 Characterisation 40
2.2 Design of Experiment (DOE) 40
2.2.1 Preparation of Metallic Implants 44
2.2.2 Preparation of Sodium Dihydrogen Phosphate Anhydrous solution 44
2.2.3 Preparation of Calcium Acetate Monohydrate solution 45
2.2.4 Reaction 45
2.2.5 Characterisation 46
2.2.6 Optimal Run 46
2.3 Degradation Study 47

2.3.1 Preparation of Hank's Balanced Salt Solution 47
2.3.2 Magnesium Sample Preparation 47
2.3.3 Degradation Testing 48
2.3.4 Analysis 49
2.3.5 Degradation of Magnesium by Mass Loss 50
2.3.6 Analysis of Sample Surface 51
2.4 Characterisation 52
2.4.1 ATR-FTIR 52
2.4.2 Scanning Electron Microscopy and Electron Dispersive X-Ray 52
2.4.3 X-ray Diffraction 52
2.4.4 Optical Profilometry 53
3 Chapter 3: Results and Discussion 54
3.1 Octacalcium Phosphate Synthesis 54
3.1.1 ATR-FTIR 54
3.1.2 SEM 55
3.2 Design of Experiment Study 57
3.2.1 Response 1: %OCP 61
3.2.2 Response 2: Ca:P Ratio 64
3.2.3 Response 3: Coating Thickness 71
3.2.4 Optimisation 78
3.3 Optimal Run 80
3.3.1 SEM 80
3.3.2 EDX 80
3.3.3 XRD 81
3.3.4 Optical Profilometry 82
3.3.5 Model Accuracy 83

3.4 Degradation Study 85
3.4.1 Adhesion Testing 85
3.4.2 Mass Loss 87
3.4.3 pH 89
3.4.4 SEM 91
3.4.5 XRD 99
3.5 Summary 103
4 Conclusions and Further Research 104
References 107
Appendix A
Design of Experiment Solutions A
Design of Experiment Factors G
Design of Experiment Point Prediction H
Design of Experiment Build Information H

List of Figures

Figure 1: Cross section of the humerus bone showing the location of the articular cartilage, periosteum, endosteum, medullary cavity, and blood supply. (Original design created in Biorender by the author). 5
Figure 2: The differentiation pathways that can be taken from mesenchymal stem cells to osteoblasts [26]. Original design created in Biorender by the author. 8
Figure 3:The differentiation pathways that can be taken from a haematopoietic stem cell to an osteoclast [26]. Original design created in Biorender by the author. 8
Figure 4: A cross-section of compact bone featuring the osteon and the blood vessels, osteocytes, and lamellae that are contained within it [38], [39] Original design created in Biorender by the author. 9
Figure 5: The configuration of the bone remodelling "cutting cone" in cortical bone, showing the location of bone cells within the mechanism [49]. 12
Figure 6: The bone remodelling process, showing each of the stages of the cycle: activation, resorption, reversal, formation, and termination [25], [43]. Original design created in Biorender by the author. 12
Figure 7: Shown here are the different stages of indirect fracture repair, highlighting the outer layer of the periosteum (P), new woven bone formation (W), and cartilage undergoing ossification (C) [60]. 15
Figure 8: Photomicrograph of gap healing at 8 weeks, showing the woven bone formed in the gap (A) at a right angle to the original bone cortex (B). Cutting cone remodelling to replace the woven bone with correctly aligned lamellar bone can be seen (C) [60]. 17
Figure 9: (A) Total hip replacement, showing the configuration of the stem, femoral head, liner, and acetabular shell. (B) Composition of the total knee replacement, demonstrating the positioning of the femoral component, insert, and the tibial component [72]. 21
Figure 10: Temporary implants - (A) Plates, (B) screws, (C) pins, (D) cerclage wires, and (E) intramedullary rods used in fracture fixation [74]. 22
Figure 11: Crystal structure of hydroxyapatite [158]. 31
Figure 12: Crystal structure of alpha-TCP and beta-TCP [159]. 32
Figure 13: Crystal structure of octacalcium phosphate.[160] 32
Figure 14: Classification of adhesion test results for test method A [188]. 50
Figure 15: ATR-FTIR spectrum of OCP synthesised in-house. 55
Figure 16: SEM image of OCP synthesised in-house, at 500 X magnification. 56
Figure 17: SEM image of OCP synthesised in-house, at 5000 X magnification. 56
Figure 18: Effect of pH on %OCP. 63
Figure 19: Effect of surface roughness on % OCP. 63
Figure 20: Effect of pH on Ca:P ratio. 66
Figure 21: Effect of the interaction between pH and concentration on Ca:P ratio. 67
Figure 22: Effect of the interaction between pH and digestion time on the response of Ca:P ratio. 68
Figure 23: Effect of the interaction between concentration and digestion time on Ca:P ratio. 69
Figure 24: Effect of surface roughness on Ca:P ratio. 70

Figure 25: Effect of the interaction between the surface roughness and temperature on the response of the coating thickness. 74
Figure 26: Effect of the interaction between digestion time and concentration on the response of the coating thickness. 75
Figure 27: Effect of the interaction between the surface roughness and flow rate on the response of the coating thickness. 76
Figure 28: Effect of concentration on coating thickness. 77
Figure 29: Representative SEM image of the OCP coatings at 500x produced using the optimal run sample (Scale bar 10 µm). 80
Figure 30: EDX of the optimal run samples. 81
Figure 31: XRD spectrum of the optimal run coating. 82
Figure 32: Optical profilometry profile of the optimal run. 83
Figure 33: Adhesion test results for OCP coated WE43 Mg-alloy samples, tested according to ASTM D3359-22 Test Method A. 86
Figure 34: Mass loss over time of coated and uncoated WE43 samples during degradation. 87
Figure 35: Rate of degradation over time for coated and uncoated WE43 samples. 88
Figure 36: pH change over time for coated and uncoated WE43 samples. 89
Figure 37: SEM image at 400x of OCP-coated WE43 before degradation (scale bar 50 µm). 92
Figure 38: SEM image at 400x of OCP-coated WE43 samples after 1 day of immersion in HBSS (scale bar 50 µm). 93
Figure 39: SEM image at 400x of OCP-coated WE43 after 4 days of immersion in HBSS (scale bar 50 µm). 94
Figure 40: SEM image at 400x of OCP-coated WE43 samples after 7 days of immersion in HBSS (scale bar 50 µm). 95
Figure 41: SEM image at 400x of uncoated WE43 samples after 1 day of immersion in HBSS (scale bar 50 µm). 96
Figure 42: SEM image at 400x of uncoated WE43 samples after 4 days of immersion in HBSS (scale bar 50 µm). 97
Figure 43: SEM image at 400x of uncoated WE43 samples after 7 days of immersion in HBSS (scale bar 50 µm). 98
Figure 44: XRD spectrum of OCP-coated WE43 prior to immersion in HBSS. 99
Figure 45: XRD spectrum of OCP-coated WE43 after 1 day of immersion in HBSS. 100
Figure 46: XRD spectrum of OCP-coated WE43 after 4 days of immersion in HBSS. 101
Figure 47: XRD spectrum of OCP-coated WE43 after 7 days of immersion in HBSS. 102

List of Tables

Table 1: Design of Experiment inputs. 42
Table 2: Reagents used in the production of HBSS. 47
Table 3: Optical profilometry scanning parameters. 54
Table 4: Responses for each run in the DOE study. The results presented are the mean value of three measurements. 58
Table 5: Analysis of variance (ANOVA) of the response of %OCP. 61
Table 6: Fit statistics of the response of percentage OCP. 62
Table 7: ANOVA for the response of Ca:P Ratio. 65
Table 8: Fit statistics of the response of Ca:P ratio. 66
Table 9: ANOVA for the response of the coating thickness. 72
Table 10: Fit statistics for the response of coating thickness. 73
Table 11: The five most desirable solutions proposed by the DOE study. 79
Table 12: EDX results for the optimal run. 81
Table 13: XRD results for the optimal run. 82
Table 14: Inputs and predicted results for the optimal run. 84
Table 15: Predicted VS actual results for the optimal run and the percentage error. 84
Table 16: XRD results of OCP-coated WE43 prior to immersion in HBSS. 99
Table 17: XRD results of OCP-coated WE43 after 1 day of immersion in HBSS. 100
Table 18: XRD results of OCP-coated WE43 after 4 days of immersion in HBSS. 101
Table 19: XRD results of OCP-coated WE43 after 7 days of immersion in HBSS. 102

Abbreviations

ATR-FTIR Attenuated total reflectance-Fourier transform infrared spectroscopy

ATZ Alumina-toughened-zirconia

BMD Bone mineral density

BMP Bone morphogenic protein

BMU Bone multicellular unit

CaP Calcium phosphate

CAM Calcium acetate monohydrate

DOE Design of experiment

EDX Energy-dispersive X-ray spectroscopy

FDA Food and Drug Administration

HAp Hydroxyapatite

HBSS Hank's balanced salt solution

HCl Hydrochloric acid

IFM Interfragmentary movement

IGF Insulin-like growth factor

IL Interleukin

NaOH Sodium hydroxide

OCP Octacalcium phosphate

PTH Parathyroid hormone

RFMS Radio frequency magnetron sputtering

SBF Simulated body fluid

SDPA Sodium dihydrogen phosphate anhydrous

SEM Scanning electron microscopy

α-TCP Alpha-Tricalcium phosphate

β-TCP Beta-Tricalcium phosphate

TGF-β Transforming growth factor-Beta

TNF-α Tumour necrosis factor-Alpha

Y-TZP Yttria-tetragonal zirconia polycrystal

ZTA Zirconia-toughened alumina

Abstract: Influence of Surface Coatings on the Degradation Properties of Metallic Orthopaedic Implants – Beth Macaulay.

Magnesium has proved to be a good candidate as an orthopaedic implant due to its tensile strength, weight-bearing ability, cytocompatibility, and biodegradability. However, magnesium degrades too rapidly *in vivo* to match bone growth rate, which can lead to pain, inflammation, and implant failure.

Calcium phosphate-based coatings offer a possible mechanism to reduce the degradation of magnesium implants *in vivo* while promoting bone growth. Octacalcium phosphate is a precursor to hydroxyapatite, the calcium phosphate phase that forms the mineral component of bone. This project aims to design and characterise an octacalcium phosphate coating and apply it to magnesium alloy WE43 specimens using an immersion method, then investigate the degradation of the coated implants in simulated physiological conditions.

Octacalcium phosphate was synthesised using the dropwise addition of calcium acetate monohydrate to a sodium dihydrogen phosphate anhydrous solution. An immersion process for coating metallic implants was developed by submerging the implant in the stirred octacalcium phosphate reaction solution for the duration of the reaction. A design of experiment approach was then used to investigate the optimal parameters of the coating process. The resulting optimised coated magnesium specimens underwent a degradation study in Hank's balanced salt solution at 37°C. The degradation of the implants was quantified by measuring the mass loss of magnesium throughout the degradation. SEM and XRD spectroscopy were used to investigate the formation of an apatite on the implant's surface. The coating method produced a pure octacalcium phosphate coating on the WE43 samples with a calcium/phosphate ratio of 1.33, and good adhesion and a thickness of 1.802 μm. The degradation study showed that the octacalcium phosphate coating significantly reduced the degradation of magnesium and the octacalcium phosphate coating fully transformed into hydroxyapatite after seven days of immersion in Hank's balanced salt solution.

Acknowledgements

I would like to extend my immense gratitude to those who helped me throughout my completion of this thesis. Firstly, I would like to thank my supervisors, Prof Nicholas Dunne and Dr Tanya Levingstone, for their continued support and guidance throughout this project. I would also like to thank Dr Robert Flavin and those at PBC Biomed Ltd, namely Gerard Insley and Antzela Tzagiollari for sharing their expertise and equipment with me. And to my fellow students in the MEDeng group who constantly provided both academic and emotional support, you have my utmost gratitude.

I would also like to thank my family and friends. To Oisín, for his constant encouragement, support, and lifts to campus. To Megan, for her constant handholding, even from Rotterdam, and most importantly, to my parents, for convincing me not to give up time and time again, and for their financial support, without which this thesis would not be possible. This is all for Paddy and Patricia.

Lastly, I would like to thank I-Form, Science Foundation Ireland, and PBC Biomed for their financial support for this project.

1 Introduction and Literature Review

For every minute that passes, eight new fracture cases arise in the European Union [1]. Fractures and joint replacements continue to be one of the most common reasons for hospital visits in Ireland, with nearly 4,000 cases attributed to hip fractures alone in 2022 [2]. The orthopaedic implant market is fast growing, expected to reach 37.76 billion USD by 2034, due to an increase in the average life expectancy and, with it, an increase in age-related diseases such as osteoporosis and arthritis [3]. Often, fractures due to trauma are minimal and can heal themselves over time, usually with the help of stabilising casts made of fibreglass or plaster of Paris. However, sometimes the breakages are more traumatic and require surgery to stabilise the fracture with orthopaedic implants. In addition to fractures, hip and knee arthroplasties have a high incidence rate in Irish hospitals. These surgeries require the total replacement of the joint with a reconstructive implant comprised of metal, ceramic, or plastic components. 93% of primary hip replacement and 98% of primary knee replacement patients between 2014-2024 were diagnosed with osteoporosis. As it is estimated that there are over 200,000 people in Ireland living with osteoporosis today, this is an area of significant concern for the biomedical research community [1], [4], [5].

Orthopaedic implants are an important area of biomedical research as they have increased in necessity and can greatly improve quality of life [5]. This thesis focuses on orthopaedic implants made from magnesium, a relatively new area of study in the field, as the literature suggests it has promising osteoconductive properties while being naturally biodegradable in the body [6], [7]. To attempt to control the degradation of magnesium, this project looks at octacalcium phosphate (OCP) as an implant coating. OCP is another relatively new area of research and it demonstrates promising results of osteoconductivity *in vitro* and *in vivo*, with multiple methods investigated for applying this coating to orthopaedic implants [8].

To understand what makes a successful implant, it is important to have a strong foundation of knowledge in not only the recent history of the field of orthopaedic implant research, but also in the biology and chemistry of the human bone and how it repairs itself. This thesis aims

to cover the necessary background information required, extensively review the current literature on metallic orthopaedic implants and calcium phosphate coatings, and identify gaps in the research. The goal of this project is to identify and trial a novel approach to coating magnesium implants that reduces the degradation of magnesium while promoting hydroxyapatite formation *in vitro*.

1.1 Bone

Bone is the primary component of the skeleton, along with connective tissue, cartilage, tendons, ligaments, and bone marrow [9], [10]. It is a calcified, living tissue that has many functions and takes on different formations to carry them out [11]. The primary functions of bone are to support the weight of the body, facilitate movement, and protect the internal organs [12]. Bones also have the added function of storing bone marrow, which produces red blood cells, and maintains mineral homeostasis in the body. Our bones meet together in the body to form joints, which allow the body to perform complex movements, such as bending and rotating. These bones are connected and held together by ligaments and cushioned by a layer of cartilage between the bones known as “articular cartilage”. The presence of this cartilage allows bones to move freely without rubbing or damaging each other [13].

1.1.1 Structure of the Bone

Bone is comprised of two major types of tissues: a dense outer tissue, known as compact or cortical bone, and an inner core of spongy or cancellous bone. The compact bone forms the tough exterior of bone that surrounds the medullary cavity in the centre of the bone, which contains bone marrow and cancellous bone. It is the combination of properties of both these hard and soft tissues that give bone its strength and fracture resistance. The yield stress of compact bone (50 MPa) is comparatively higher than that of cancellous bone (30 MPa). Correspondingly, cortical bone exhibits a higher Young's modulus compared to cancellous bone (10-30 GPa and 0.3-22.3 GPa, respectively), with this measure of elastic stiffness—defined as the ratio of stress to strain in the linear elastic region—underscoring the predominant load-bearing role of cortical tissue. The Young’s modulus of cortical bone is higher in the longitudinal direction (11-21 GPa) than the transverse direction (5-13 GPa) [14], [15], [16]. The relative quantities of compact and cancellous bone vary depending on the type

of bone and its shape. For example, long bones, such as the femur, have more cancellous bone and marrow than flat bones.

In all areas except the location of a joint, bones are surrounded by the periosteum, a fibrous membrane that supplies the bone with blood vessels and nerves and facilitates the connection of bones to ligaments and tendons. Similarly, the endosteum lines the inside of the medullary cavity. Both membranes contain blood cells and bone cells and can act as a starting point for new bone and, in the case of the endosteum, new marrow formation [17], [18].

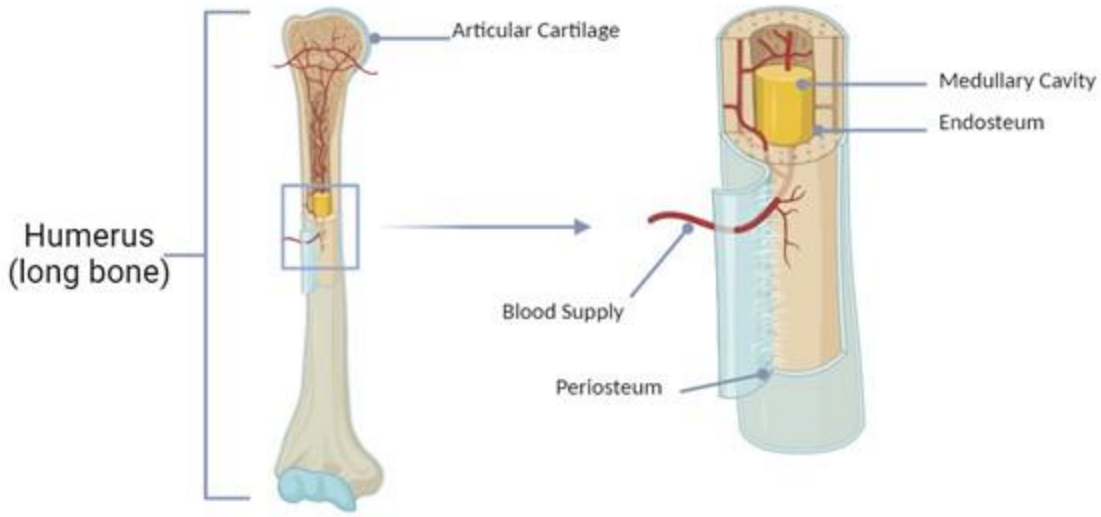

Figure 1: Cross section of the humerus bone showing the location of the articular cartilage, periosteum, endosteum, medullary cavity, and blood supply. (Original design created in Biorender by the author).

1.1.2 Bone Matrix

Bone tissue is formed by bone matrix, which is a composite material secreted by osteoblast cells that is made up of both organic and inorganic components. The organic matrix makes up approximately 20% of the wet weight of bone and is comprised primarily of collagen, a fibrous protein with a rope-like structure made up of amino acids. In addition to collagen, 10% of the organic matrix is made up of non-collagenous proteins such as fibronectin, osteopontin, and bone sialoprotein, along with proteoglycans such as decorin and biglycan [19].

The collagen in the organic matrix provides bone with its flexibility, whereas the addition of minerals from the inorganic matrix to the collagen provides bone with its stiffness. Without the inorganic component, bone tissue would be too flexible and unable to support the full weight of the body. Conversely, without collagen, the bone would be brittle and break easily under light pressure. It is the combined matrices that give bone its toughness to protect and support the body. The inorganic matrix, the hard, mineralised component of bone, consists mostly of the crystalline calcium phosphate phase hydroxyapatite [$Ca_{10}(PO_4)_6OH_2$]. It makes up 65–70% of the wet weight of bone. The inorganic matrix also serves as the body's ion reservoir, storing approximately 99% of calcium, 85% of phosphorus and 40-60% of sodium and magnesium in the body. These ions form crystalline structures surrounding and within the collagen fibres to combine and give bone the strength it needs to support the body [20].

1.1.3 Bone Cells

In embryonic formation, stem cells divide numerous times and eventually differentiate into all different types of tissue cells, going on to produce tissues such as bone, tendons, , cartilage, blood, and so on [21]. Mesenchymal stem cells can be found in the bone marrow and have the ability to differentiate into many different cell types including myocytes (muscle cells), adipocytes (fat cells), and osteoblasts (bone-forming cells). They can be found within these tissues in the adult body [22], [23]. Haematopoietic cells, on the other hand, are another type of stem cell that can develop into all types of blood cells including monocytes, which can eventually develop into osteoclasts (bone resorbing cells) [24], [25], [26]. Both of these stem cells can be found in the bone marrow. There are four significant cells involved in the formation, maintenance, and remodelling of the bone: osteoprogenitor cells, osteoclasts, osteoblasts, and osteocytes, and each of these began from one of the stem cells mentioned above [17].

Osteoprogenitor cells, also known as osteogenic or bone-forming cells, are stem cells found on the endosteum and periosteum membranes as well as within the bone itself. They are derived from mesenchymal stem cells during embryonic bone formation. Osteoprogenitor cells can differentiate into osteoblasts and eventually osteocytes, after being triggered to do so by mechanical stresses, injuries, or diseases, which initiate the bone remodelling process

[17], [27]. They can also differentiate into chondrocytes (cartilage-producing cells) when exposed to growth factors. Recent evidence suggests that hypertrophic chondrocytes can also differentiate into osteoblasts [28], [29].

Osteoblasts are single-nucleated cuboid cells that are responsible for building bone. They do this by secreting osteoid, which is an unmineralised organic tissue containing collagen, proteoglycans, and glycoproteins. This tissue becomes mineralised by the addition of calcium and phosphate ions to the osteoid matrix. These ions are already present in the surrounding extracellular matrix and are actively taken into the osteoid by the osteoblast itself. Once inside the matrix, the calcium and phosphate ions deposit as hydroxyapatite crystals within the collagen fibres of the osteoid. The osteoblasts repeat this process and produce layers of mineralised bone tissue in the form of lamellae in the lamellar bone matrix [17], [30].

Osteoclasts are large, multinucleated cells that are derived from haematopoietic stem cells, and their primary function is to break down and resorb bone when the remodelling process is triggered. Osteoclasts reside on the surface of the bone tissue in 50 μm deep depressions known as Howship's lacunae. The osteoclast releases protons using a H+ATPase pump, which acidifies and degrades the mineralised bone tissue. Multiple osteoclasts seal off the area of resorption, creating a microenvironment and ensuring that no healthy bone is destroyed unintentionally. After degradation, the dissolved bone is absorbed by the osteoclast and removed to the extracellular space. When the bone matrix is dissolved, growth factors are released that incite osteoblasts to build new bone at the resorption site, completing the remodelling process. Calcium and phosphate ions are also released from the bone into the blood, regulating the levels of the minerals in the body [17], [31].

Osteocytes are mature osteoblasts that are encased by bone matrix secreted in the remodelling process. They are abundant in bone tissue and serve an essential function by facilitating communication between other bone cells through an interconnecting network of canaliculi. Osteocytes can signal the initiation of the bone remodelling process and facilitate mineral homeostasis by releasing molecules that trigger the response of osteoclasts and osteoblasts. The osteocyte can also regulate the metabolism by producing hormones such as

insulin-like growth factor-1 (IGF-1) and sclerostin, which regulate glucose and phosphate levels, respectively [17], [32], [33].

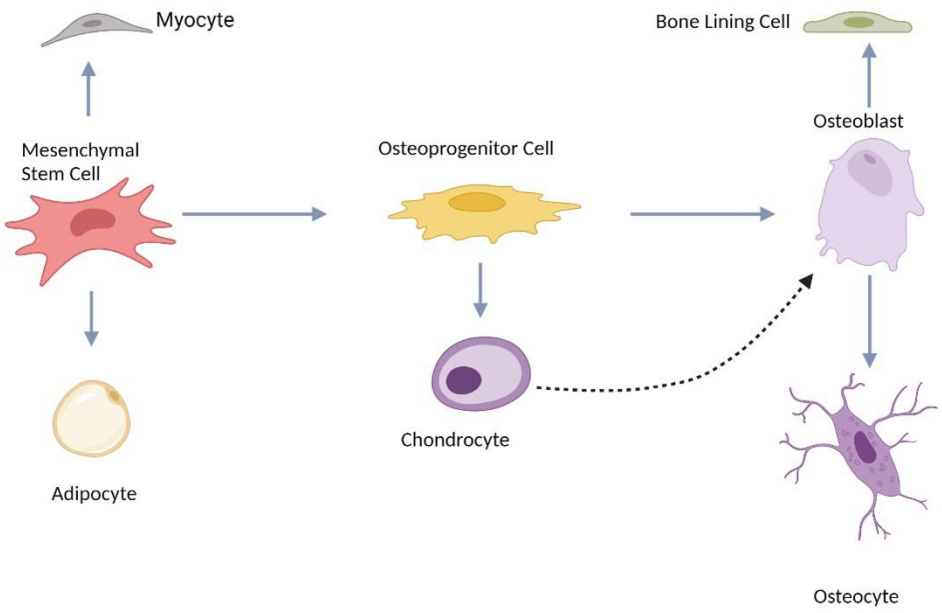

Figure 2: The differentiation pathways that can be taken from mesenchymal stem cells to osteoblasts [26]. Original design created in Biorender by the author.

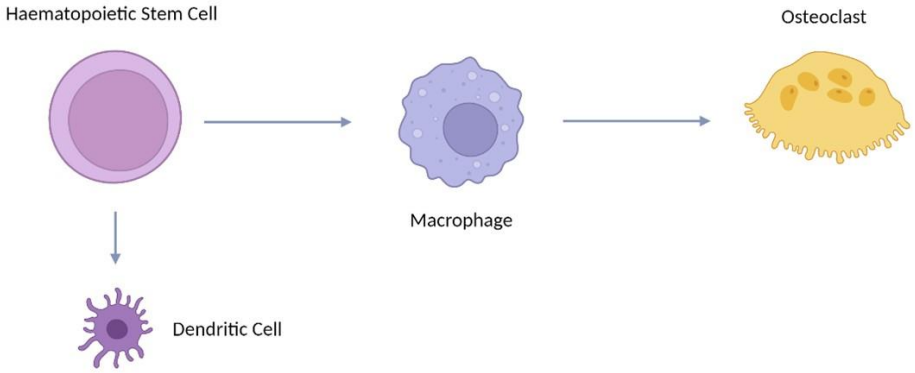

Figure 3:The differentiation pathways that can be taken from a haematopoietic stem cell to an osteoclast [26]. Original design created in Biorender by the author.

1.1.4 Osteons

Compact bone is arranged in closely packed, repeating cylindrical functional units called osteons - or "Haversian Systems" - that form parallel to each other and mainly in the long axis of the bone. The osteons consist of concentric layers of compact bone matrix known as "lamellae" of which there can be up to 20 at 3-7 µm thick and residing within them are

osteocytes. The lamellae are arranged surrounding a central “Haversian canal” that contains blood vessels and nerves that run throughout the bone and nourish the surrounding tissue and cells. The blood vessels in the Haversian canals are interconnected by capillaries that reside in Volkmann’s canals, or “canaliculi”, small channels in the bone that run obliquely through the osteons. Osteons are constantly being remodelled as a response to the mechanical stress that they endure [34], [35], [36], [37], [38].

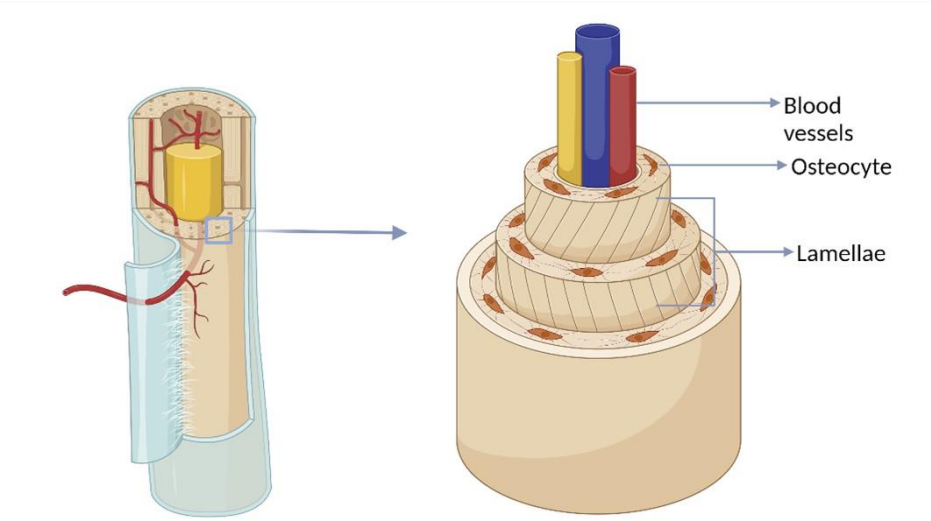

Figure 4: A cross-section of compact bone featuring the osteon and the blood vessels, osteocytes, and lamellae that are contained within it [38], [39] Original design created in Biorender by the author.

1.2 The Bone Remodelling Process

Throughout life, bone goes through repeated growth, modelling, and remodelling. In childhood and adolescence, the bones grow both radially and longitudinally, with the latter occurring at the growth plates, where cartilage proliferates at either ends of the long bones [40]. The bone remodelling cycle, as defined by Frost, is a highly regulated process of replacing old, damaged bone with newly formed bone and is a continuous mechanism occurring constantly in the body [41]. The remodelling cycle can be triggered locally by mechanical stress on a specific site in the bone resulting in osteocyte apoptosis, leading to the release of paracrine factors which recruit osteoclast and osteoblast precursors to the remodelling site. Remodelling can also be triggered systemically by changes in hormone levels such as

parathyroid hormone, requiring calcium to be liberated from calcium stores in the bone. By this pathway, the bone remodelling process does not occur at a specific site. Wolff's Law, developed by anatomist and surgeon Julius Wolff, states that the bone will adapt to the degree of mechanical loading under which it is placed. This means that bone will be deposited and reinforced in the areas of greatest stress through the mechanism of bone remodelling. Conversely, a decrease in stress on the bone will cause the bone to weaken overtime. The duration, magnitude, and rate of forces applied to the bone determine how the integrity of the bone is altered [26], [42], [43]. The methods by which damaged bone is replaced and the time this process takes is important to consider when designing biodegradable orthopaedic implants.

The cycle takes place in the bone multicellular unit (BMU), which consists of osteoclasts, osteoblasts, and blood supply from the surrounding capillaries. The lifespan of the unit itself is longer than the cells contained within it, and, therefore, requires constant replenishment of these cells [26]. The structure and composition of the BMU are dependent on its location - in compact bone, the osteoclasts in the BMU form a “cutting cone” that bores into the bone, removing damaged bone and laying new, healthy bone behind it (Figure 5). In cancellous bone, the BMU acts on the surface forming Howship’s lacunae, which are then resorbed and refilled with healthy tissue. However, the remodelling process is the same in both types of bone [26], [44].The bone remodelling process is divided into several overlapping stages - activation, resorption, reversal, formation, and termination – which take place over approximately 120-200 days [26], [44] (Figure 5, Figure 6).

1.2.1 Activation

The remodelling cycle is activated either by osteocytes or by fluctuating hormones, depending on whether the remodelling is to take place locally or systemically. In local remodelling, osteocyte apoptosis caused by microdamage to the bone leads to the recruitment of osteoblast and osteoclast precursor cells from the circulatory system to the area of damage. The bone lining cells then separate, exposing the surface of the bone, and form a covering over the resorption site. Pre-osteoclast cells bind to the bone matrix to form a sealing zone, which isolates the resorption site and ensures no healthy bone is affected [26], [44].

1.2.2 Resorption

Osteoclasts in the resorption site secrete protons to dissolve the bone mineral. They also release proteases to break down the collagenous organic bone matrix. When sufficient resorption has taken place, the osteoclasts undergo pre-programmed apoptosis to prevent excess bone resorption [26], [44].

1.2.3 Reversal

In reversal phase, it is thought that mononucleated cells of an osteoblastic lineage, known as "reversal cells," resorb unmineralised organic matrix in the remodelling site and deposit a mineralised matrix known as a "cement line", which enhances osteoblastic adherence. It has been postulated that the cells involved in the reversal phase are involved in sending and receiving the signals that couple the bone resorption phase to the formation phase. However, the exact mechanism of this and the specific cell signals are not yet known [26], [44], [45], [46], [47], [48], [49].

1.2.4 Formation

During the bone formation phase, osteoblasts secrete collagenated organic matrix, which is then mineralised by the deposition of hydroxyapatite crystals amongst the collagen fibrils. The mineralisation process is regulated by the control of calcium and phosphate concentrations, both locally and systemically, and by mineralisation inhibitors such as osteopontin and pyrophosphate [26], [44].

1.2.5 Termination

When mineralisation is complete, the bone remodelling process is terminated when osteocytes secrete antagonists to osteogenesis. The osteoblasts in the remodelling site have one of three fates: differentiate into bone lining cells on the surface of the bone, become enveloped in the bone matrix and differentiate into osteocytes, or undergo apoptosis [26].

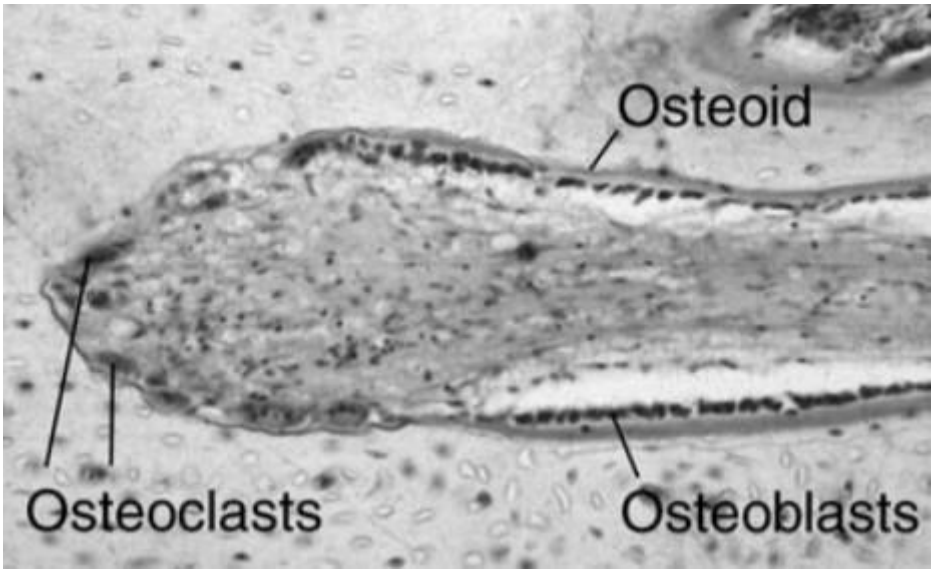

Figure 5: The configuration of the bone remodelling "cutting cone" in cortical bone, showing the location of bone cells within the mechanism [49].

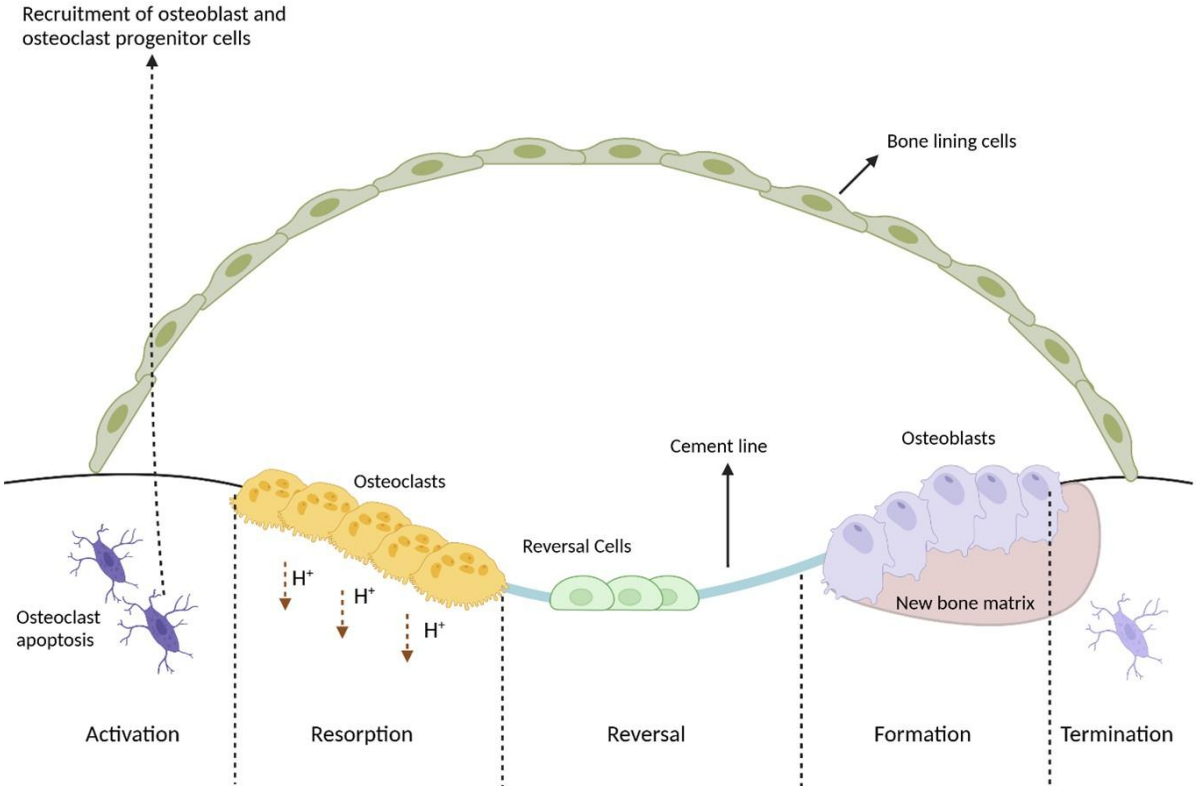

Figure 6: The bone remodelling process, showing each of the stages of the cycle: activation, resorption, reversal, formation, and termination [25], [43]. Original design created in Biorender by the author.

1.3 Fracture Healing and Repair

The body's method of healing fractured bone is a well-orchestrated process that involves multiple cell types, cytokines, chemokines, and growth factors. This process mirrors many of the formative events that occur during embryonic formation. For this reason, and because bone is one of the few tissues that heal without forming a scar, the process of fracture healing is often considered to be a form of tissue regeneration [50]. The majority of all fractures do not require surgical intervention – if the skin and soft tissue surrounding the fracture remains intact, and the bone fragments are still in alignment, the fracture can be stabilised with casts or braces, and a process known as indirect healing takes place. However complex fractures, fractures through joints, fractures with extensive soft tissue damage, and open and infected fractures necessitate stabilisation with orthopaedic implants and fixations [51].

1.3.1 Indirect Healing

The most common form of fracture healing is known as indirect or secondary fracture healing and involves both endochondral and intramembranous bone healing. It is enhanced by micro-motion and weight-bearing. However, too much motion and weight will lead to delayed healing or even non-union. The process of indirect healing involves four phases: haematoma formation, callus formation, bone formation, and bone remodelling [50], [52].

Immediately following the trauma causing the fracture, an inflammatory response is triggered. A haematoma is formed between and around the fracture and within the medulla from the periphery and intra-medullary blood and bone marrow cells. This forms a scaffold for a soft callus to form. Proinflammatory molecules such as tumour necrosis factor-α (TNF-α) and interleukin 1 (IL-1), IL-6, IL-11, and IL-18 are released. These factors are responsible for the recruitment of inflammatory cells and the promotion of angiogenesis [50], [53], [54], [55], [56].

Following the haematoma formation, a fibrin-rich granulation tissue develops. Fibrin is an insoluble protein that is produced by fibrinogen, a soluble protein found in blood plasma, at the site of tissue damage. The fibrin molecules then combine to form a mass of long threads that intertwine with platelets, resulting in a spongey formation that hardens into a blood clot

[57]. Within this fibrin-rich granulation tissue, cartilage forms in between the ends of the fracture and at external and periosteal sites. This cartilaginous tissue grows into a soft callus, providing a stable structure to the fracture site. This has been shown to occur approximately 7-9 days post-trauma in animal models. Concurrently, intramembranous ossification occurs adjacent to either end of the fracture, eventually bridging together to form a hard callus that provides rigidity and weight-bearing ability to the fracture site [50], [53], [54], [55], [56], [58].

As the chondrocytes in the callus proliferate, they become hypertrophic, and the extracellular matrix calcifies. This occurs as the mitochondria of the chondrocytes accumulate calcium from the fracture environment. The calcium granules are then transported to the extracellular matrix where they precipitate with phosphate and form mineral deposits, which initiate homogenous nucleation and lead to the formation of apatite crystals. As the cartilage is calcified and replaced with woven bone, the callus becomes harder and more mechanically rigid. This is followed by the bone remodelling process, where osteoclasts resorb the bony hard callus and replace it with lamellar bone. Bone remodelling is induced by electrical polarity created when pressure is applied to a crystalline environment. For this reason, a gradual increase in load must be placed on the healing fracture to ensure the bone heals correctly [50], [59]. The stages of indirect fracture healing can be seen in histological samples (Figure 7).

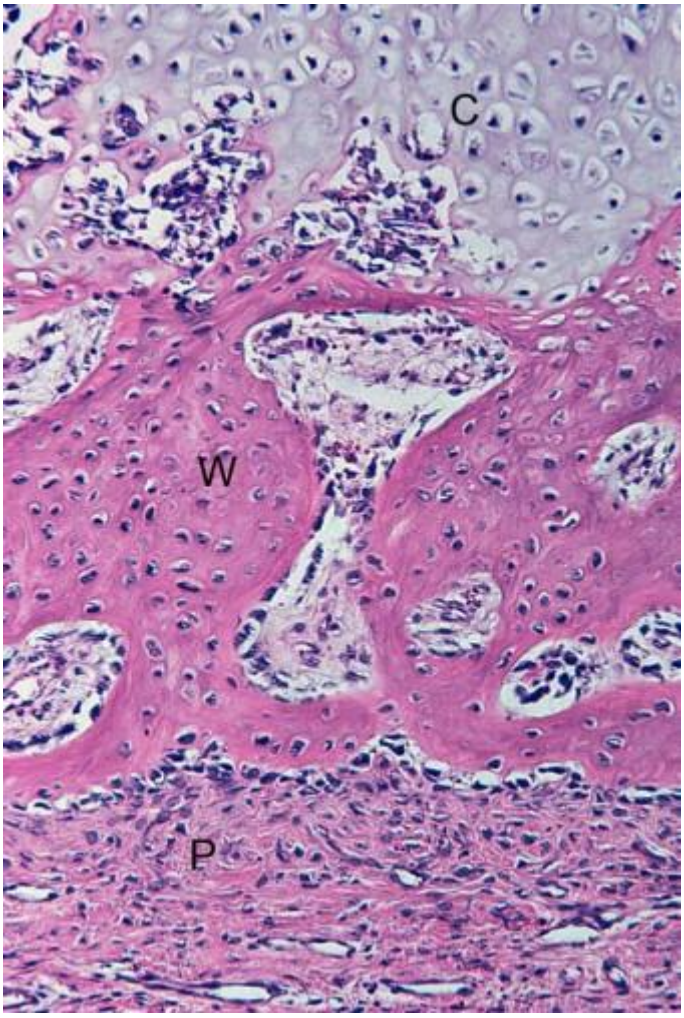

Figure 7: Shown here are the different stages of indirect fracture repair, highlighting the outer layer of the periosteum (P), new woven bone formation (W), and cartilage undergoing ossification (C) [60].

1.3.2 Direct Healing

As opposed to indirect healing, direct healing requires the surgical reduction and stabilisation of the fracture using implants so that there is little to no gap formation in the fracture. Direct healing can occur by either contact healing or gap healing, depending on the distance between the fracture ends [55], [60].

Contact healing, sometimes referred to as primary bone repair, occurs when the gap between the fracture ends is less than 0.01 mm and the interfragmentary strain is less than 2% [50], [55], [56], [60]. Orthopaedic implants are used to reduce the strain and bring the fracture ends together so that bone on one side of the cortex is in direct contact with bone on the other side. When the fracture has been stabilised under these conditions, the reparative

process can begin. Cutting cones form at the fracture ends. Osteoclasts resorb damaged and necrotic bone, creating cavities which are later filled with new bone by the osteoblasts. This process results in the restoration of the haversian systems in the axis of the breakage simultaneously with the bridging of the fracture, which allows for the blood vessels to heal and penetrate the bone to provide blood and nourishment. The bridging bone will later undergo remodelling resulting in complete fracture repair without the formation of a callus [55], [60].

Similarly, gap healing involves the same processes of bridging the bone and haversian system remodelling, however, these processes do not occur simultaneously. Gap healing occurs under different conditions – when the fracture gap is larger than that of contact healing, but smaller than 1 μm [52], [60]. The fracture is bridged by a woven bone scaffold which begins to form from the bone marrow and is slowly replaced by lamellar bone beginning after approximately two weeks (Figure 8). This lamellar bone is aligned perpendicularly at right angles to the longitudinal axis of the bone. The lamellar bone subsequently undergoes the remodelling process to form correctly aligned mature bone with organised haversian systems and vasculature [55], [58], [60], [61], [62].

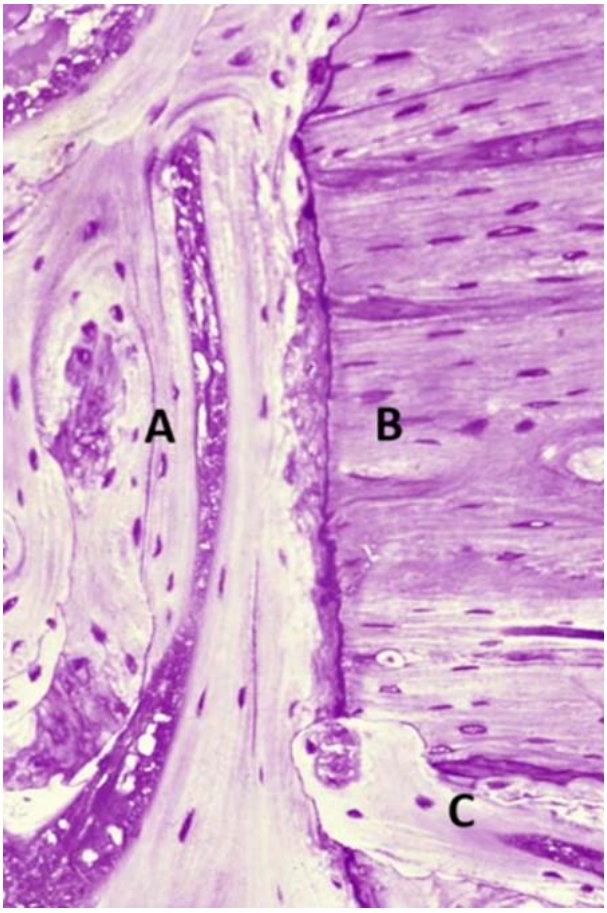

Figure 8: Photomicrograph of gap healing at 8 weeks, showing the woven bone formed in the gap (A) at a right angle to the original bone cortex (B). Cutting cone remodelling to replace the woven bone with correctly aligned lamellar bone can be seen (C) [60].

1.3.3 Factors Affecting Fracture Healing

Fracture healing and the factors that affect it are crucial to consider when designing orthopaedic implants. Fracture repair is influenced by a combination of internal and external elements. Internally, the body's ability to create the optimal environment plays a crucial role. This can be influenced by a myriad of factors such as age, hormones, vitamin and mineral deficiencies, diseases, and lifestyle. Osteoporosis, which is on the rise as life expectancy increases, causes the bone to become fragile and porous due to an imbalance between bone resorption and bone formation in the remodelling cycle. This not only leads to the bones becoming highly susceptible to fractures but also leads to delays in fracture healing [60], [63]. This is likely due to the body's decreased ability to produce osteoblasts from mesenchymal stem cells as it ages.

Hormones play a key role in maintaining the overall health of the body, acting as chemical messengers that facilitate most physiological processes. Oestrogen influences various cellular mechanisms in the bone remodelling and healing processes as it promotes osteoblast activity, aids in both the synthesis and mineralisation of collagen, and regulates the expression of growth factors involved in bone repair such as TGF-β [50], [55]. A decrease in oestrogen levels during menopause can cause the body to become prone to developing osteoporosis. Parathyroid hormone (PTH) is essential to the fracture healing and bone remodelling process as it stimulates osteoblast activity. Deficiency in PTH can be a result of many conditions, such as hypoparathyroidism, some cancers, and vitamin D and magnesium deficiency [55], [60], [62], [63].

Patients with diabetes mellitus are particularly prone to fractures and impaired bone healing. Diabetes can cause a decrease in bone mineral density (BMD) resulting in a condition known as osteopenia, a precursor to osteoporosis.[56], [64], [65] There is also evidence that diabetes can hinder cartilage formation in healing fractures as it decreases chondrocyte differentiation and proliferation. Diabetes is associated with chronic low-grade inflammation in the body which can lead to elevated levels of TNF-α, a pro-inflammatory cytokine which is normally expressed in the event of a fracture. In diabetic animal studies, increased TNF-α expression has been shown to cause the rapid removal of cartilage, accompanied by an increase in the number of osteoclasts in the diabetic bone callus [62], [66].

Infection at the fracture site can significantly impact bone healing. The incidence of fracture-related infection for open fractures is approximately 20%. [67] Infection in the setting of an open fracture can be due to multiple factors, both internal and external. The risk factors include aspects of patient lifestyle such as obesity and smoking, but often infection is introduced to the fracture due to the contamination of wounds and traumatised soft tissue. Infection at the fracture ends will delay or prevent fracture healing. For example, staphylococcus aureus can invade osteoblast cells and bypass immune detection. While inside the osteoblast, S. aureus will produce toxic byproducts that induce cellular apoptosis and necrosis. Bacteria can thrive on orthopaedic hardware, forming biofilms that are resistant to systemic antibiotics due to the lack of blood supply and, therefore, immune response in the

area. As such, these biofilms harbouring bacterial colonies require surgical intervention to be cleared. Failure to eradicate the infection can lead to continued bone and tissue destruction, abscesses in the bone, and the loosening of orthopaedic hardware [51], [67], [68].

The external factors influencing fracture healing involve the interfragmentary movement (IFM) and stability of the fracture. Small axial interfragmentary movements have been shown to induce callus formation and promote healing in animal models with small fracture gaps [51]. However, when the gap is larger, reduction of the gap with stable fixation to achieve a smaller IFM is necessary for correct healing. Large IFM due to low stabilisation delays bony bridging of the fracture and causes tissue strain and hydrostatic pressure in the fracture site that can hinder the vascularisation of the fracture. Overly stiff fixation that does not allow for IFM can suppress callus formation, but this can be compensated for by applying external IFM [51], [52], [56], [69], [70].

1.4 Orthopaedic Implants

Orthopaedic implants are a common surgical method for the treatment of bone injuries or diseases requiring reconstructive repair. In fracture repair, they are surgically implanted at injury sites to provide support and structure for the bone to allow it to heal with correct alignment. Orthopaedic implants are also used to replace joints such as the knee or hip when they become inflamed or disabled due to illness or injury. The shape of an implant is specific to its function, and the efficacy is highly dependent on the materials used and the dimensional accuracy of the implant [71], [72]. In order to effectively design an orthopaedic implant, it is necessary to first understand how the bone remodels and repairs itself. It is also critical to research by which methods fractures can be repaired surgically as well as what orthopaedic implants are commonly used and how they can be improved upon.

1.4.1 Classification of Orthopaedic Implants

Orthopaedic implants can be classified in two ways: permanent and temporary. Permanent implants are expected to stay in the body and serve their function throughout the lifespan of the patient. This includes implants used for reconstructive procedures such as hip, knee, ankle, and shoulder joint replacements. Hip and knee prostheses, in particular, have undergone extensive research and development as these joints carry the full weight of the body and are more likely to wear out as patients age [64], [73], [74]. As load-bearing and frequent movement are necessary for these joint replacements, the implants are very difficult to design and optimise. The progress in knee joint prostheses has been slower than that of the hip as the biomechanics of knee movement are particularly complex. A typical hip replacement consists of a stem inserted into the femur, a femoral head, a liner, and an acetabular shell. The femoral head is fitted on top of the stem, and a liner is placed between the shell and the head to protect it from wear. The knee replacement prosthetic is usually composed of a femoral component, an insert to protect from wear and provide a smooth gliding surface, a tibial tray, and a patellar component. It is imperative that these joint replacements not only mimic the movement and load-bearing ability of the original joints, but also have greater wear resistance. The ultimate goal of these implants is to eliminate pain and discomfort and to allow the patient to live a normal life [72], [75], [76], [77].

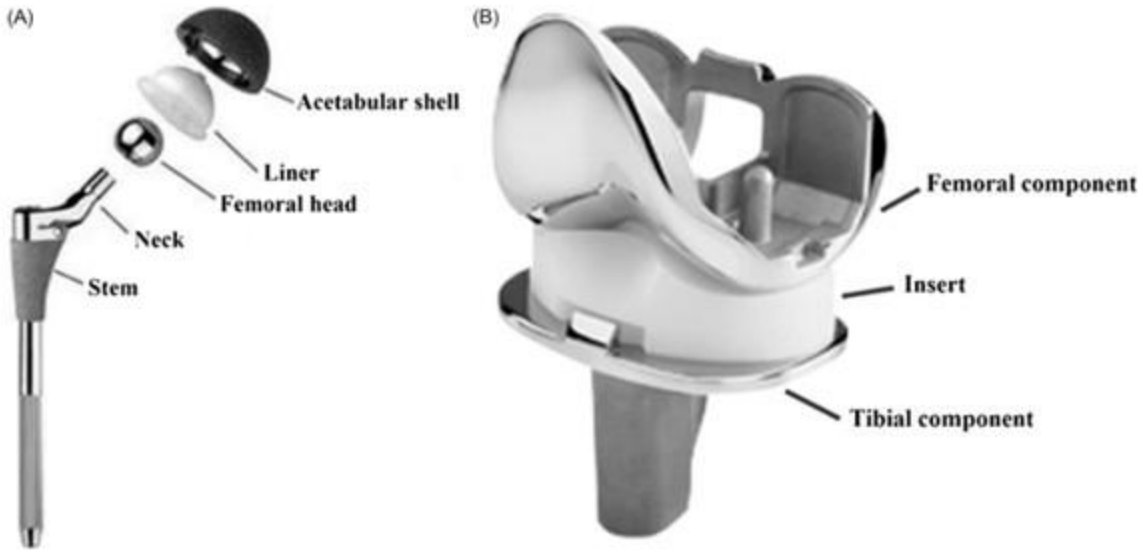

Figure 9: (A) Total hip replacement, showing the configuration of the stem, femoral head, liner, and acetabular shell. (B) Composition of the total knee replacement, demonstrating the positioning of the femoral component, insert, and the tibial component [72].

Permanent implants are also used for reconstructive purposes. For example, spine implants are used to correct the alignment of the spine in such cases as scoliosis patients.[78] The surgical procedure for this condition can take many forms depending on the age of the patient and the degree of spinal curvature. The most common procedure in adults is the posterior approach, in which two or more vertebrae are fused using bone grafts or ceramic material grafts. This is to inhibit independent movement of the vertebrae and prevent further curvature. Subsequently, metal rods are placed on either side of the fused vertebrae and are secured in place with screws or wires. The rods help to correct and stabilise the spinal curvature while the vertebrae are fusing. These implants generally stay in the patient's body permanently after the fusion process is complete as the bones often grow around the implants. Removing the implants would require a subsequent surgery, which puts the patient at further risk. As orthopaedic implants are manufactured using durable and biologically inert materials, a removal surgery is generally not carried out, save for cases of infection or implant failure [72], [78], [79], [80].

Temporary orthopaedic implants are used to repair fractured bones during the healing process. These generally take the form of plates, screws, cerclage wires, pins, and

intramedullary nails and are designed to serve for a short period and be removed when the healing process is complete [72]. Plates are used to compress broken bone fragments together to facilitate the natural healing process, and are fixed in place with screws and pins. The plates are designed in a variety of shapes and sizes according to their specific applications and have pre-drilled holes for the screws and pins. Screws are often used in conjunction with other implants, such as plates, to fix them to the fractured bone. However, they can also be used by themselves to fix broken fragments. Similarly, pins can be used to fix other implants to the bone or used alone to repair bones under a relatively weak force. Metal cerclage wires are lightweight and flexible, making them very versatile implants. They can be utilised to stabilise and align fractures where the bone has broken into multiple fragments, and to stabilise spiral fractures. Intramedullary rods are long metal rods that are inserted into the medullary cavity of long bones to immobilise the bone in the case of a severe fracture. They are anchored to the bone by screws or pins, which are inserted into pre-drilled holes in the intramedullary rod. This method of stabilising open fractures is generally preferred over external fixation as it has a significantly lower incidence of infection and malunion [72], [74], [75], [76], [81], [82], [83], [84].

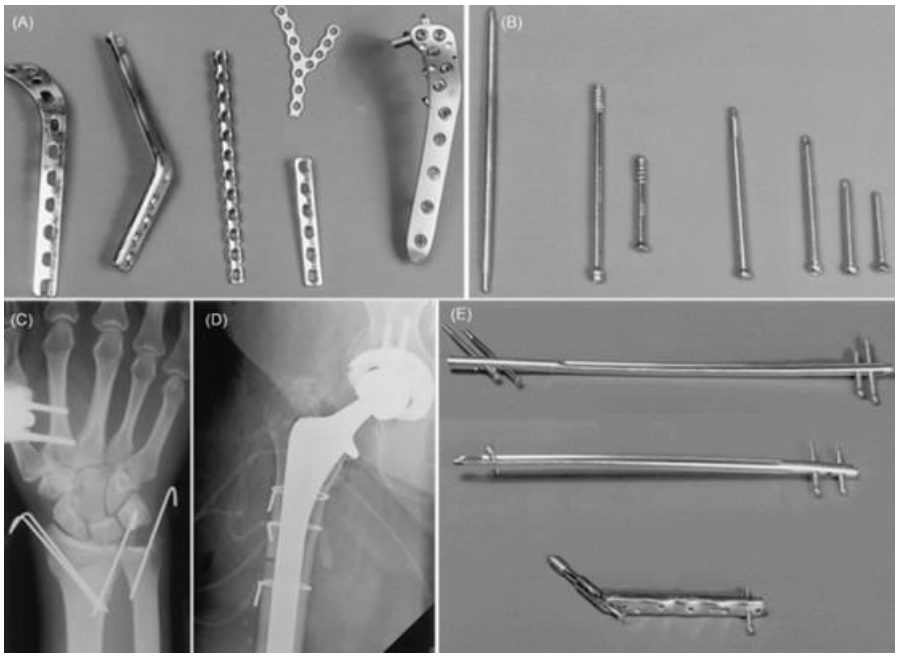

Figure 10: Temporary implants - (A) Plates, (B) screws, (C) pins, (D) cerclage wires, and (E) intramedullary rods used in fracture fixation [74].

1.4.2 Orthopaedic Implant Materials

Orthopaedic implants can be made from metal, ceramic, or polymer materials, depending on their function. Metallic implants, such as titanium or surgical steel, are used for high load-bearing and reconstructive applications, such as rods to stabilise the spine in scoliosis patients [85]. Ceramic implants, however, may not possess the high mechanical strength of metals like titanium, but can have better tribological properties and are less likely to wear. They are often used as adhesive cement or coatings for metallic implants. Polymers are commonly used as interposition-based cementing materials between bone and implant in hip and knee arthroplasties. They generally have high wear resistance and low frictional properties [72], [77], [86], [87], [88].

1.4.3 Considerations of Implant Materials

The purpose of orthopaedic implants is to restore the structure and functionality of injured joints and bones. The implants must possess desirable characteristics such as mechanical stability, corrosion resistance, wear resistance, and biocompatibility. The ability of the implant to deliver these requirements is highly dependent on the materials from which the implants are made.

The yield strength, tensile strength, fracture toughness, and Young's modulus are important mechanical properties to consider when designing and choosing an orthopaedic implant. Young's modulus describes the relative stiffness of a material and can be calculated by the ratio of stress to its corresponding strain value. The resulting constant of proportionality is the modulus of elasticity or Young's modulus (E). A stiffer material will have a higher Young's modulus than a flexible material [89], [90]. It is important to consider this when designing an orthopaedic implant because if Young's modulus of the implant material is much higher than that of bone, it can lead to a condition known as "stress shielding". This condition leads to a loss of bone (osteopenia) when a rigid implant is removed from the bone, as the implant had assumed the majority of the load and stress placed on the bone during the healing process. The imbalance in load distribution diminishes the mechanical stimulation necessary to stimulate adequate fracture repair and bone remodelling, leading to increased bone resorption. This results in bone that may have increased porosity and higher fracture

potential. Stress shielding often leads to loosening of the implant due to increased resorption around the implant site, necessitating subsequent surgery to replace the implant [72], [89], [91].

The yield strength of an orthopaedic implant material refers to the stress level at which permanent (plastic) deformation will occur [92]. The yield strength of the implant material must be high enough to prevent bending or warping of the implant during regular use and physiological loads. The tensile strength of an implant represents the maximum stress the implant can endure in a single incident before it cracks or fractures. This is important to consider as the implant should be able to withstand extreme forces and trauma. [93], [94] The fracture toughness of an implant is another critical mechanical property to consider. The fracture toughness is a measure of the implant material's ability to resist fracture propagation under cyclic or repetitive loading, such as walking and running. The process of implant failure depends on the stress state of the implant system as well as whether the microstructure of the material renders it ductile, brittle, or semi-brittle [85], [92]. As a general rule, a ductile material will yield before fracture, while brittle materials fracture before yield. A semi-brittle material offers a certain amount of plastic deformation before fracturing [92]. Hence, it is important to consider these mechanical properties when designing or choosing an orthopaedic implant material, depending on its intended purpose [85], [89], [91], [92], [93], [94], [95], [96], [97].

The corrosion resistance of an implant material describes the tendency of a material to corrode in a physiological environment. Human body fluids consist of various ions such as sodium, potassium, magnesium, chloride, phosphate, and bicarbonate ions, as well as amino acids, proteins, and dissolved oxygen. These chemicals can initiate electrochemical corrosion on the surface of the implant, which can lead to damage of the implant, release of implant debris, and fluctuation of the pH of the surrounding area. Acidification of the physiological environment can accelerate the corrosion process and can lead to inflammation in the area. For metallic implants, corrosion can be characterised as pitting, crevice, galvanic, intergranular, stress-corrosion cracking, corrosion fatigue, and fretting corrosion, the latter of which is a particular concern for load-bearing implants. Fretting corrosion occurs at the

interface between implant components due to cyclic loading, allowing body fluids to enter small gaps in the implants. It presents as pits or grooves in the implant surrounded by corrosion products. Corrosion leads to the degradation of implants, compromising the structural integrity of the implant and resulting in premature failure [72], [96], [98].

Wear refers to the removal of material from a surface and is a common problem in the field of orthopaedics and biomedical engineering. Wear between the joints is prevented naturally by cartilage, which secretes fluid during loading. Cartilage-on-cartilage contact is natural in a healthy body, however when the cartilage and synovial fluid become degraded due to trauma or diseases such as arthritis, bone contact can occur. This leads to pain and inflammation [92], [94], [96]. Wear is a problem for orthopaedic implants as it can lead to the release of wear debris particles into the nearby tissues, resulting in inflammation and immune response, bone and tissue damage, and potential implant failure or rejection. Lubrication, the use of a film or layer to separate opposing surfaces during motion, is crucial to consider at any implant-on-implant or implant-on-bone interface. As well, a material with high wear resistance is desired for orthopaedic implants. The wear resistance is dependent on Young's modulus, tensile strength and yield strength of a material [72], [92], [95], [96].

Biocompatibility is defined by the US Food and Drug Administration (FDA) as "the ability of a device material to perform with an appropriate host response in a specific situation"[99] and is the most important factor to consider for all kinds of medical implants. Implants must be made from nontoxic materials to prevent activating the immune system and inducing a hypersensitivity or allergic reaction. In the case of orthopaedic implants, even implants made from inert materials can produce toxic corrosion or wear byproducts when in the physiological environment. These toxic particles are considered "foreign bodies" to the immune system and trigger an inflammatory response at the implant-bone interface. This can lead to bone resorption and eventual implant loosening. Therefore, it is critical for the implant material to not only be biocompatible, but also to have high resistance to corrosion and wear [72]. Biocompatible orthopaedic implants can undergo osseointegration, which is the direct structural and functional connection between living bone and the loading surface of the implant [100]. For the majority of orthopaedic implants, this osseointegration is desired as it

can result in better treatment of bone injuries and reduce the potential for implant loosening. Therefore, it is important to consider when designing or choosing an implant material [96], [100], [101], [102], [103], [104], [105].

1.4.4 Metals

Metals are the most common materials used for orthopaedic implants, both permanent and temporary, due to their properties of strength, corrosion resistance, biocompatibility, and fracture toughness. Metallic biomedical implants are generally made from either stainless steel, cobalt alloys, or titanium alloys, all three of which have been approved for orthopaedic implant use by the US Food and Drug Administration [72].

Stainless steel is an iron-based alloy with at least 12% chromium content, which prevents corrosion. The first stainless steel implant was introduced in the 1920s as an orthopaedic implant, and since then, its uses have expanded to a variety of purposes throughout the body, such as cardiovascular stents and cochlear implants. The primary stainless steel alloy used in biological implants is the 316L alloy, whereby the "L" denotes the low carbon content (0.03%). Also known as surgical stainless steel, ASTM International specifies that the 316L alloy contains 18% chromium, 12% nickel, and 3% molybdenum [106]. 316L possesses the mechanical qualities that make it fit for use as an orthopaedic implant. However, it is highly susceptible to stress corrosion and cracking, so it is often limited to use in situations that are not significantly load-bearing for an extended period. Nevertheless, 316L makes up nearly 60% of surgical implants used in the USA [72], [88], [101], [106], [107], [108], [109], [110].

Titanium alloys are commonly used as permanent and load-bearing implants due to their good mechanical properties, biocompatibility, and corrosion resistance. Titanium alloys have been used as orthopaedic implants, dental implants, heart valves and pacemakers, among others. Pure Ti can take the form of a hexagonal close-packed crystal structure (α phase) up to 885°C, and above this temperature, it has a body-centred cubic structure (β phase). Alloys of Ti can be grouped as α alloys, near-α alloys, α-β alloys, and β alloys, based on their microstructure [72]. The most used Ti alloy for orthopaedic implants is Ti-6Al-4V, an α-β alloy. At room temperature, it consists of approximately 90% α phase, which is stabilised by

aluminium, and 10% β phase, which is stabilised by vanadium. The dual-phase microstructure provides a highly desirable balance of strength, ductility, and fatigue resistance [72], [96], [111].

The elastic modulus of Ti-6Al-4V is 110 GPa. This value is closer to the elastic modulus of bone, 10-30 GPa, than other metals used for implants, such as 316L (200 GPa) and cobalt-chromium alloys (200-230 GPa). This closer match reduces the likelihood and severity of stress shielding at the implant site. While Ti-6Al-4V has an impressive strength-to-weight ratio, higher tensile strength (860-100 MPa), higher fatigue strength (620-725 MPa), and higher yield strength (&95-875 MPa) than 316L implants, it also has superior corrosion resistance [111]. This is due to the formation of a protective TiO_2 layer on the implant when exposed to the physiological environment. While 316L and CoCr alloys also form oxide layers on their surfaces, they can be more susceptible to corrosion from the Cl^- ions in body fluids. The TiO_2 layer also contributes to improved biocompatibility, as it prevents ion release from the implant, therefore mitigating an inflammatory response from the body.

The mechanical properties, biocompatibility, and corrosion resistance of a Ti implant are greatly influenced by the addition of other elements in the alloys. While Ti-6Al-4V is the most popular Ti alloy for orthopaedic uses, other alloys are being studied as alternatives. The elastic modulus of TI-6Al-4V is closer to the bone than many other available metal implant materials, however the relatively high value of 110 GPa does not eliminate the possibility of stress shielding. Due to their significantly different composition to bone, osseointegration and biocompatibility of Ti is compromised. It has been shown that while bone can form around the Ti implant, there is no strong chemical bond between the implant and bone. Also, the Al and V present in the Ti-6Al-4V are generally considered toxic materials and could potentially cause adverse reactions in the body. For these reasons, many alternative Ti alloys have been studied – for example, the Ti-15Mo (β alloy) and Ti-35Nb-7Zr-5Ta (β alloy) show lower elastic moduli at 78 GPa and 55 GPa, respectively, and possess greater osseointegration with no toxic elements in the alloys. The research into improving Ti orthopaedic implants is ongoing. However, Ti-6Al-4V remains the most commonly used Ti implant to date [72], [96], [111], [112], [113], [114].

1.4.5 Magnesium

Magnesium and its alloys are a relatively new area of research in the field of metallic orthopaedic implants. Their most attractive properties include biodegradation and osseointegration properties. Magnesium, naturally found in the body, is inert and highly biocompatible. It actively encourages bone growth as it stimulates osteoblast proliferation and differentiation, enhances the production of BMP-2, and upregulates osteogenic markers by releasing $Mg2^{+}$ ions. However, its mechanical properties are limited. Mg alloys have a good elastic modulus of 41-45 GPa, lower than that of both 316L and Ti alloys, but their yield strength (65-100 MPa) and ultimate tensile strength (135-285 MPa) are significantly lower than their competitors. This can limit their use away from load-bearing applications [110], [115], [116], [117].

As magnesium naturally degrades in the body, corrosion resistance is not a factor that is generally considered for their use as implants. Instead, researchers have studied how to use the corrosion to their advantage. An implant that fully degrades over time in the body would eliminate the need for a subsequent surgery to be removed, avoiding further surgical risks for the patient. Furthermore, with its superior osteogenic properties and osseointegration, the Mg implant could enhance the repair and growth of bone as it is gradually dissolved and replaced with new bone. However, strict control of this degradation is paramount. As Mg degrades in an aqueous solution, it releases hydrogen gas which can irritate and interfere with tissue healing. Also, the degradation must be controlled to ensure the implant does not fully degrade before the healing process has been completed. Alloying elements and surface modifications, such as calcium phosphate coatings, have been studied as methods to control the rate of degradation of Mg in the physiological environment, as well as to enhance their mechanical properties [118], [119], [120], [121], [122], [123], [124].

1.4.6 Ceramics

Ceramics used in the field of orthopaedics can be classified in two ways: bioinert and bioactive. Bioinert ceramics have demonstrated excellent wear resistance, compressive strength, and biocompatibility. The most common bioinert ceramic materials used in orthopaedic implants include alumina (Al_2O_3), and zirconia (ZrO_2), which have been used for

musculoskeletal applications since 1960 [72], [125]. Alumina has merits such as high hardness (15 – 20 GPa), high scratch resistance, low friction coefficient (0.55), and chemical stability, due to the strong ionic and covalent bonds between the Al^{3+} and O^{2-} ions [72], [126], [127]. It also has high surface wettability due to easy bonding with proteins and water molecules. However, the major disadvantage of alumina is that it has relatively low tensile (249.5 MPa) and flexural strength (265 – 338 MPa), and its brittle nature makes it prone to fracture under high mechanical loads [72], [127], [128].

Pure zirconia can exist as monoclinic, tetragonal, and cubic crystals, depending on the temperature. Below 1170°C it is monoclinic and at that temperature it will transform to the tetragonal phase, and to the cubic phase at approximately 2370°C. Upon these phasic transformations, the volume and shape of the zirconia will change. Therefore, other elements are often added to zirconia to increase transformation toughening, improve mechanical properties, and to make it suitable for use in biomedical applications. Through this process of research and development, yttrium-stabilised zirconia, or yttria-tetragonal zirconia polycrystal (Y-TZP) has become one of the most used zirconia-based ceramics for joint arthroplasty components. Y-TZP has better fracture and flexural strength (886 – 1526 MPa and 1300 – 1500 MPa, respectively) compared to alumina and has a similar Young's modulus to Ti alloys (210 GPa) [129], [130]. However, femoral head components made from Y-TZP showed significant ageing and low-temperature degradation, leading to microcracks and roughening [72], [125], [131], [132], [133]. In more recent times, composite materials known as dispersion ceramics have been studied to improve the mechanical properties of alumina and zirconia. These dispersion ceramics include zirconia-toughened-alumina (ZTA) and alumina-toughened-zirconia (ATZ), with ZTA demonstrating more favourability in orthopaedic applications. The combination of alumina and zirconia in general, along with other additives, combines the strengths of each ceramic while seemingly counteracting the weaknesses of one another [72], [125], [132], [134].

In clinical practice, bioinert ceramics are most often used as bearing surfaces, for example in total joint arthroplasty. Alumina and zirconia are commonly used in hip and knee arthroplasties as they have low friction coefficients, therefore releasing fewer particles

caused by abrasive wear than metallic materials. They are also biologically inert, meaning they do not produce a substantial immunological response or rejection. As well, ceramic particles are less cytotoxic than metal particles. Ceramics also have higher wettability and lower biofilm production compared to metals. Ceramics are often considered as an alternative implant material to metals if a patient has a metal allergy. Currently, there is only one full ceramic total knee arthroplasty implant on the market (BPK-S INTEGRATION Ceramic, Peter Brehm GmbH) constructed from a ceramic material known as BIOLOX® Delta, which is made from an alumina matrix with tetragonal zirconium oxide (ZTA) distributed uniformly throughout [125], [131], [132], [134], [135], [136], [137], [138].

1.4.7 Calcium Phosphate Coatings

Calcium phosphates (CaPs), bioactive ceramics, have emerged as an important area of study in the advancement of orthopaedic implants. They show promising results as coatings on metallic orthopaedic implants. They are biocompatible, closely mimicking the inorganic component of bone, and have proven to be osteoconductive in numerous studies [139], [140], [141]. They also provide an interface between the implants and the surrounding natural bone tissue and can reduce the degradation of metallic implants, significantly enhancing the biological performance of metallic implants, and making them very desirable candidates for orthopaedic and dental clinical applications. The application of CaPs is limited to their use as coatings and cements for implants, as their low ductility and weak ionic bonds make them unsuitable as bulk implant materials [125], [131], [142], [143], [144], [145].

The most studied CaPs for use as a coating on orthopaedic implants include hydroxyapatite (HAp), α and β tricalcium phosphate (α-TCP, β-TCP), and octacalcium phosphate (OCP), which are defined by their crystal structure and calcium to phosphate ratio (Ca/P) (Figure 11, Figure 12, Figure 13). Synthetic HAp ($Ca_{10}(PO_4)_6(OH)_2$), which has a Ca/P ratio of 1.67, is chemically very similar to the inorganic bone mineral. Natural bone contains calcium-deficient HAp which has a Ca/P ratio of 1.37-1.87 and includes significant amounts of carbonate (4-8 weight %) and trace elements such as magnesium, sodium, and potassium. Synthetic HAp also typically has higher crystallinity, in which the crystals form well-defined hexagonal structures. As an implant coating, HAp has an exceptional ability to bond directly to bone, leading to

enhanced osseointegration. It has also been shown to reduce the degradation of metallic implant materials *in vitro* [146], [147], [148], [149]. Similarly, α-TCP, which has a monoclinic crystal structure, has shown exceptional biological activity when applied as a coating, and in physiological conditions undergoes hydrolysis to form calcium-deficient hydroxyapatite. However, the high solubility of α-TCP can lead to rapid degradation in physiological conditions, raising concern that the coating may degrade prematurely and impact the functionality of the implant. While α-TCP has limitations to consider as an implant coating, it has been used successfully in clinical applications as bone cement [150], [151]. β-TCP, which crystalises in a rhombohedral form, has similar biocompatibility and osteoconductive properties to HAp and α-TCP but has a moderate dissolution rate which forms a balance between stability and biological activity. For these reasons, β-TCP has proven useful as bone graft substitutes [131], [142], [148], [152], [153], [154], [155], [156], [157]

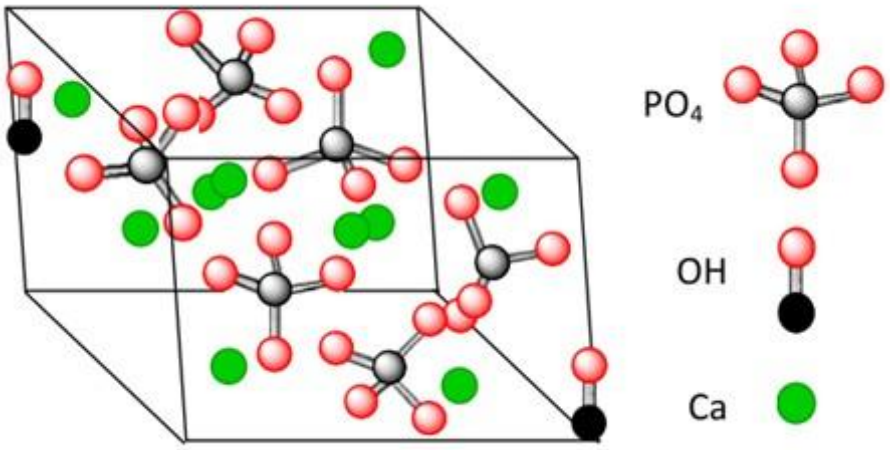

Figure 11: Crystal structure of hydroxyapatite [158].

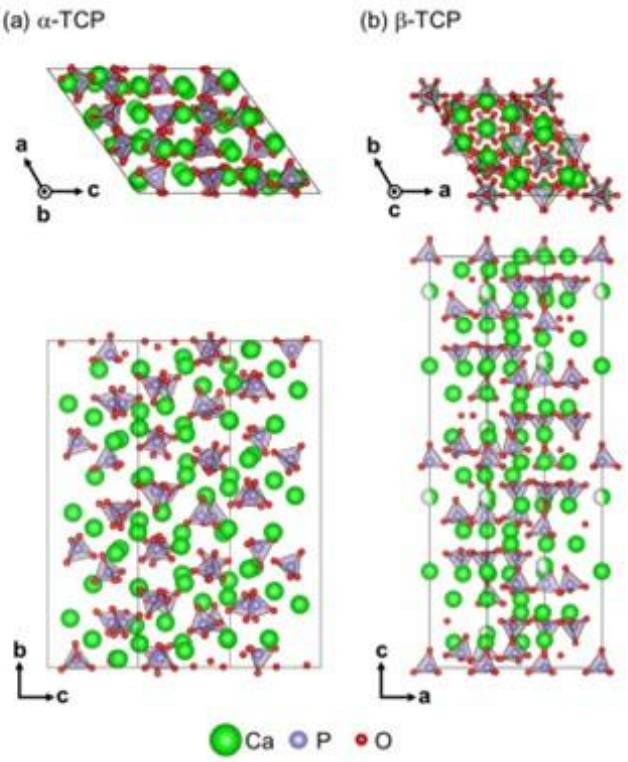

Figure 12: Crystal structure of alpha-TCP and beta-TCP [159].

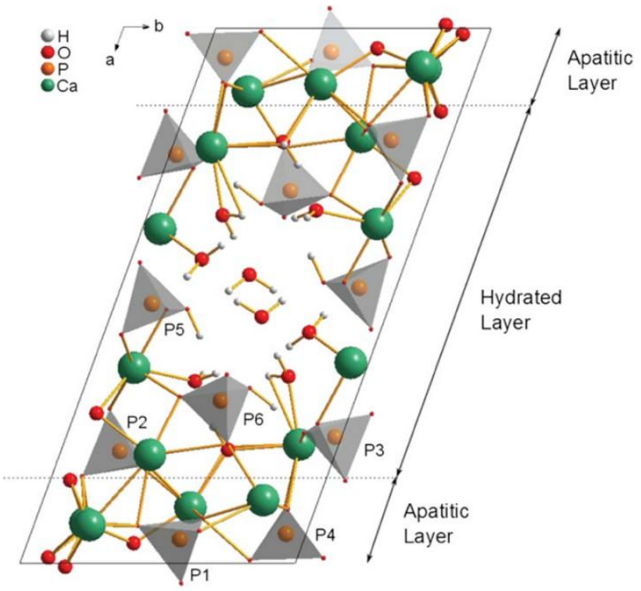

Figure 13: Crystal structure of octacalcium phosphate.[160]

1.4.8 Octacalcium Phosphate (OCP)

OCP ($Ca_8H_2(PO_4)_6{\cdot}5H_2O$) demonstrates superior osteoconductive traits compared to HAP and offers more controlled dissolution compared to α-TCP. The crystal structure of OCP (Figure 13) is comprised of alternating hydrated and apatite layers, closely resembling the structure found in developing bone tissue. This enables OCP to effectively facilitate ion exchange and

cellular interactions, surpassing that of HAp and TCP. Due to the structure of OCP, it is a precursor of biological apatite crystals in bone and tooth. While both OCP and β-TCP have moderate rates of dissolution in physiological conditions, OCP's dissolution mechanism more closely resembles that of the bone remodelling process. As well, OCP shows enhanced protein and cellular attachment compared to HAp and TCP [157], [161], [162], [163]. It has been demonstrated that osteoblasts align on the surface of OCP and initiate new bone deposition using a structure composed of OCP particles and non-collagenous proteins, which is nearly identical to the components of bone nodules described by Bernard and Pease [161], [164], [165].

OCP can exhibit variations in stoichiometry due to excess hydrogen, resulting in the non-stoichiometric formula of $Ca_{16}H_{4+x}(PO_4)_{12}(OH)_x{\cdot}(10\text{-}x)H_2O$, which closely resembles the structure of HAp. This results in the Ca/P ratio of OCP ranging from 1.23-1.37, but is commonly observed at 1.33. OCP's unique crystal structure creates an effective barrier against magnesium implant corrosion in physiological conditions due to the hydrated layers in the crystal lattice. This unique characteristic results in superior degradation protection compared to HAp. It is for these reasons that OCP is considered a very promising candidate as a coating and is the focus of this study. The limitations of OCP as an implant coating must be considered, however. The performance of the OCP coating is significantly dependent on the coating thickness, adhesion, and phase purity, all of which are controlled by the method used to apply the coating [161], [162], [166].

1.4.9 Calcium Phosphate Coating Methods

CaP coatings can be applied to implants physically and chemically. A widely used physical technique is plasma spraying, in which the CaP powder is injected into a high-temperature plasma jet which melts the particles before spraying them on the implant surface. This method generally produces favourable results such as high adhesion strength and controllable coating thickness, however the high temperatures used in this process can lead to phase decomposition, changing the crystalline structure of the CaP and therefore the characteristics and performance of the coatings. This makes it unsuitable for use with CaPs that exist at lower temperatures, such as OCP and HAp. Also, cracks and delamination may

occur in the CaP coatings during the heating and cooling processes involved in plasma deposition [87], [142], [167], [168], [169]. Radio frequency magnetron sputtering (RFMS) is another physical method of applying CaP coatings. In this method, the coating is applied by sputtering the CaP particles with accelerated argon ions, producing uniform and dense coatings with high adhesion strength and phase purity. The structure, morphology, and Ca/P ratio of the resulting coating can be considerably influenced on the radio frequency power discharge density, working gas atmosphere, deposition time, and electrical substrate bias of the deposition process. However, it can be difficult to accurately control the phase of the CaP coating produced. Also, the instrumentation required for both plasma deposition and RFMS method can be expensive and it can be difficult to coat implants with irregular geometries, therefore limiting the availability of this method for commercial use [72], [142], [169], [170], [171].

Chemical methods, or wet deposition methods, are increasingly popular areas of study for coating CaPs as they are generally inexpensive, relatively simple to carry out, and can apply the coating to irregular implant geometries. One popular method is the biomimetic approach, which aims to recreate the method in which mineral tissues are formed in the body, resulting in coatings closely resembling natural bone. In the biomimetic method, the metal implant is immersed in a simulated body fluid (SBF) that is supersaturated with respect to calcium phosphate under physiological conditions [172], [173], [174]. Barrère *et al.* demonstrated a biomimetic method that produced OCP on Ti6Al4V plates. In this method, the plates were pretreated by being soaked in an SBF solution for 24 hours, which produced a dense and uniform amorphous calcium phosphate coating on the plates. Subsequently, the pretreated plates were immersed again in SBF for 48 hours, during which the initial coating partially dissolved and induced the nucleation and growth of OCP on its surface. The results were favourable, producing a uniform coating consisting of 100% pure OCP at 55 µm thick [175].

Similar methods were used to produce a HAp coating on Ti6Al4V plates and porous tantalum cylinders showing favourable results [148]. This study, however, used a reactor in which the SBF solution was constantly refreshed, and the pH was kept constant in acidic conditions with the addition of CO_2 gas to the main supersaturation solution for apatite crystal growth. This

was necessary due to the low solubility of HAp and the limited concentration range for the metastable phase of SBF. This process resulted in a thick and homogenous carbonate-containing HAp coating that closely resembles bone [148]. As of yet, the biomimetic method has not been successful in producing other calcium phosphates as coatings, as they do not typically precipitate under physiological conditions, unlike OCP and HAp. The biomimetic method has many advantages: it is a low-temperature process that is suitable for the precipitation of heat-sensitive substrates, it forms osteoconductive apatite with good bioactivity and resorption characteristics, it produces evenly deposited coatings regardless of implant geometry, and it can incorporate additives that can further induce bone growth. However, this method can be time-consuming, difficult to scale up to a manufacturing level, and is limited in its production of CaP phases [124], [148], [172], [174], [176].

Electrochemical deposition of calcium phosphate coatings is another coating method that has been well studied. The process involves manipulating the pH of the immersion solution to induce controlled mineral formation on the surface of metallic implants by applying a cathodic potential to the implant surface. This releases hydroxide ions throughout the solution, elevating the pH which triggers the precipitation of calcium phosphate from the solution [177], [178]. Thanh *et al.* demonstrated a HAp coating deposited on the surface of 316L samples using the electrochemical deposition method. This study produced a homogenous HAp coating on the surface of the 316L sample which showed good bioactivity in *in vitro* tests with SBF. The study also found that the characteristics of the resulting coating are dependent on the concentration and ratio of calcium and phosphate in the electrolyte solution, the pH of the solution, the processing temperature, and any additives in the coating [178]. The main advantage of the electrochemical deposition method is the control over the coating thickness, composition, and crystallinity by adjusting the experimental parameters. This process also operates at relatively low temperatures, preventing thermal degradation of the calcium phosphates, as well as possessing the ability to coat structures with complex geometries. However, it can be difficult to obtain the optimal parameters to produce the desired coating characteristics, as even small variations in the parameters can significantly impact the coating. It has also been suggested that this method can impart defects onto the coating, as the production of hydrogen gas from the charged implant can block the formation

of the coating in some areas, which can also affect the coating adhesion [146], [177], [178], [179], [180].

1.5 Summary

Magnesium-based materials are generating considerable attention as biodegradable orthopaedic implants. Compared to other implant materials, such as titanium and stainless steel, magnesium and its alloys are biodegradable. This eliminates the necessity, trauma, and risks associated with a subsequent implant removal surgery. Magnesium implants have excellent mechanical properties, low density, and the ideal Young's modulus for orthopaedic implants. However, the major limitation of Mg-based implants is the undesirable accelerated rate of corrosion in physiological conditions. Therefore, much focus has been spent on controlling the degradation rate of Mg-based implants.

Considering the requirement for bioavailability and osteoconductive potential, calcium phosphates make good candidates for surface coatings of Mg-based implants. OCP is generally considered to have the most favourable characteristics compared to other CaPs, such as HAp and β-TCP. OCP shows superior osteoconductive properties, mimicking the mineral deposition process of natural bone formation, and has demonstrated an ability to control the degradation of magnesium implants *in vitro*. However, it must be noted that the currently available coating methods have many limitations and can produce ineffectual coatings. Going forward, the focus of research in this area must be directed towards developing a cost-effective, relatively simple method of applying OCP to metallic substrates that produce a uniform coating with a high OCP percentage and good adhesion properties to effectively control the degradation of magnesium-based implants.

1.6 Project Aims and Objectives

The overall goal of this research is to develop and characterise an OCP-based coating using an immersion-based technique that effectively controls the degradation rate of magnesium-based implants. This study aims to investigate a novel coating method based on the LeGeros

method for OCP synthesis [181]. This method involves the direct precipitation of OCP on the surface of magnesium-based implants, which can be performed without the need for expensive or complex equipment. The parameters of this method were optimised using a Design of Experiment (DOE) approach, where the influence of temperature, concentration, flow rate, digestion time, and pH on the coating thickness and phase purity of the coating were analysed. The samples produced in this study were subjected to degradation tests to examine the effect of the coating on the rate of magnesium corrosion in simulated physiological conditions.

2 Materials and Methods

2.1 Octacalcium Phosphate Synthesis

Octacalcium phosphate was synthesised on a five-litre scale using the method provided by PBC Biomed Ltd, based on the method described by LeGeros (1985) [181]. Prior to commencing CaP synthesis, the pH meter and peristaltic pump were calibrated. The pH meter (WTW inoLab pH 720) was calibrated according to the manufacturer's instructions using pH buffers 4, 7, and 9. To calibrate the peristaltic pump, marprene tubing (Watson-Marlow Thermoplastic Marprene Tubing, 1.5m length 3.2mm diameter, Fisher Scientific) was placed into the pump head of the peristaltic pump (Watson Marlow, Sci-Q 323 U) and clamped. The inlet was submerged in a small beaker of deionised water, and the outlet was placed over the open mouth of a small empty beaker. The pump speed was measured against a timer and adjusted until a flow rate of 8 mL/min was achieved.

2.1.1 Synthesis

2500 mL of deionised water was added to a clean, dry 5L glass beaker on a magnetic hotplate stirrer (Fisherbrand ARE 5 Hotplate Stirrer). A 4 cm stir bar was added to the beaker before heating to 67° C while stirring at a medium setting. The temperature of the solution was monitored throughout using a thermocouple (PICOLOG T8 Thermocouple and PICOLOG software) to ensure the temperature remained consistent at 67°C +/- 2°C. 8.9985 g (0,075 moles) of sodium dihydrogen phosphate anhydrous (Fisher Scientific, CAS 7558-80-7) was weighed (Mettler Toledo Standard LA Analytical Balance) and added to the 5L beaker and allowed to dissolve completely. The pH of the sodium phosphate solution was recorded to be at pH 4.

2500 mL of deionised water was added to a 3L beaker with a 4 cm stir bar on a magnetic stir plate. The solution was stirred at a medium setting but was not heated. 17.618 g (0.01 moles) of calcium acetate monohydrate (Honeywell Fluka, CAS 5743-26-0, Fisher Scientific) was

added to the 3 L beaker and allowed to dissolve completely before being removed from the stir plate. The pH of this solution was recorded at pH 7.

The inlet of the Marprene tubing was submerged into the calcium acetate monohydrate solution and the outlet of the tubing was positioned above the sodium dihydrogen phosphate anhydrous solution so that it was at the top and centre of the mouth of the beaker. The positioning of the tubing was secured throughout the reaction with a retort stand.
The peristaltic pump was switched on to start the reaction. The time the first drop of the calcium acetate monohydrate solution hit the surface of the sodium dihydrogen phosphate anhydrous solution was noted, as well as the time precipitation was first noticed. The reaction proceeded until the entirety of the calcium acetate monohydrate solution had been transferred to the sodium dihydrogen phosphate anhydrous solution (approximately five hours), at which point the reaction vessel was removed from the heating stir plate and allowed to stand at room temperature until cool enough to touch.

2.1.2 Filtration

The Buchner filtration apparatus was prepared and connected to a built-in laboratory vacuum pump. The filter paper (Sartorius Quantitative grade 392 Filter Papers 185mm) was cut to size and placed in the Buchner funnel before being sprayed with a small amount of deionised water. The vacuum pump was switched on and the contents of the reaction vessel were carefully filtered until the filter paper was at capacity. The product on the filter paper was rinsed several times with deionised water in the funnel before being removed from the funnel and placed on a large weigh boat. This was repeated with new filter papers until all the products had been filtered. The filter papers containing the product were then placed in an oven (SciQuip Oven-140HT) at 55°C to dry.

2.1.3 Weighing

After 24 hours of drying, the filter papers were removed from the oven, and all product was transferred to a pre-weighed weigh boat and weighed on the mass balance. The product was returned to the oven to dry for another 24 hours or until the loss on drying was less than 5%.

Once the product had dried, the final weight was recorded before being transferred to an airtight container and stored in a desiccator with silica gel.

2.1.4 Characterisation

The powdered product was observed using FTIR and SEM (as described in sections 2.4.1 and 2.4.2, respectively) and characterised based on documented OCP characteristics from the existing scientific literature.

2.2 Design of Experiment (DOE)

Design of experiment (DOE) software (Design-Expert 13) was used to investigate the parameters to produce the optimal OCP-coated stainless steel samples using the OCP synthesis method described in section 2.1. In this method, the stainless steel samples were placed directly into the reaction vessel in which OCP was being synthesised. This resulted in OCP forming on the surface of the stainless steel samples as a coating.

The varied inputs included were the temperature of the reaction, the pH of the reaction, the concentration of reagents, the flow rate of CAM to SDPA, the digestion time after the reaction had finished, and the surface roughness of the stainless steel samples used. These values were varied with high, medium, and low values based on the literature of similar experiments involving coating a metallic implant with a calcium phosphate coating [148], [175], [181], [182], [183], [184], [185]. The responses examined were the % of OCP, the calcium-to-phosphate ratio, and the thickness of the coating, as these properties can impact the performance of the coating. A Box-Behnken design was used, and 51 runs were performed in which 316L implants were coated with OCP using the inputs specified by the model, as detailed in Table . Design points were also added to aid in establishing the reliability of the model [148], [175], [181], [183], [184], [185], [186]

Following completion of the DOE study, the models generated for each response were used to optimise the process. The desired outcomes of the optimisation were to maximise the percentage of OCP in the coating, to obtain a Ca:P ratio of 1.33 and to maximise the coating

thickness. 316L samples were used in the DOE as an alternative to magnesium-based samples due to the abundant availability and cost-effectiveness of 316L. The optimal parameters defined by this study were then applied to WE43 magnesium alloy samples which were investigated further.

Table 1: Design of Experiment inputs.

	Inputs					
Run	**Temp (°C)**	**pH**	**Conc. (mol/L)**	**Flow Rate (mL/min)**	**Digestion Time (hr)**	**Surface Roughness**
1	70	4	0.04	2	0.5	Medium
2	53.5	7	0.06	4	0	Medium
3	53.5	4	0.04	4	1	Low
4	37	5.5	0.06	4	0.5	High
5	53.5	5.5	0.06	6	0.5	Low
6	37	5.5	0.04	2	1	Medium
7	53.5	5.5	0.06	2	0.5	High
8	53.5	5.5	0.06	2	0.5	Low
9	53.5	5.5	0.04	4	0.5	Medium
10	70	5.5	0.04	2	1	Medium
11	70	7	0.04	2	0.5	Medium
12	53.5	4	0.04	4	0	High
13	70	5.5	0.04	6	1	Medium
14	53.5	4	0.04	4	0	Low
15	70	5.5	0.02	4	0.5	Low
16	53.5	4	0.06	4	0	Medium
17	70	5.5	0.06	4	0.5	Low
18	53.5	7	0.02	4	1	Medium
19	37	7	0.04	6	0.5	Medium
20	70	5.5	0.04	6	0	Medium
21	53.5	5.5	0.02	6	0.5	High
22	37	4	0.04	2	0.5	Medium
23	53.5	7	0.04	4	0	High
24	53.5	4	0.06	4	1	Medium

25	70	4	0.04	6	0.5	Medium
26	53.5	7	0.04	4	0	Low
27	70	5.5	0.04	2	0	Medium
28	53.5	7	0.06	4	1	Medium
29	53.5	7	0.04	4	1	High
30	53.5	5.5	0.02	6	0.5	Low
31	37	5.5	0.04	2	0	Medium
32	53.5	7	0.04	4	1	Low
33	53.5	4	0.02	4	0	Medium
34	53.5	5.5	0.02	2	0.5	High
35	53.5	7	0.02	4	0	Medium
36	37	5.5	0.04	6	0	Medium
37	53.5	4	0.04	4	1	High
38	37	5.5	0.02	4	0.5	Low
39	70	5.5	0.02	4	0.5	High
40	53.5	5.5	0.04	4	0.5	Medium
41	70	5.5	0.06	4	0.5	High
42	37	4	0.04	6	0.5	Medium
43	37	5.5	0.02	4	0.5	High
44	37	5.5	0.04	6	1	Medium
45	53.5	5.5	0.06	6	0.5	High
46	70	7	0.04	6	0.5	Medium
47	53.5	4	0.02	4	1	Medium
48	37	7	0.04	2	0.5	Medium
49	37	5.5	0.06	4	0.5	Low
50	53.5	5.5	0.02	2	0.5	Low
51	53.5	5.5	0.04	4	0.5	Medium

2.2.1 Preparation of Metallic Implants

Cleaning and Mounting

The stainless steel 316L samples (12 x 12 x 2 mm) were cleaned with acetone in an ultrasonic bath (VWR USC 500T) for 15 minutes and then rinsed with deionised water before being mounted in epoxy resin to facilitate surface roughness treatments. According to the DOE, to achieve the required surface roughness values the samples underwent one of three different surface roughness treatments: sandblasting, grinding with silicon carbide (SiC) paper, or being left untreated as-machined.

- Sandblasting resulted in a Ra value of approximately 3.5 µm, and was designated as "high" in the DOE.
- Grinding with p60 SiC paper resulted in a Ra value of approximately 1.89 µm and was designated as "medium" in the DOE.
- The samples that were cleaned but left untreated as-machined were not mounted in resin, had an approximate Ra value of 0.28 µm and were designated as "low" in the DOE.

SiC Paper

The clean 316L samples were wet ground against p60 grit silicon carbide paper (MetPrep 200mm SiC paper, TMQ) for two minutes per sample using metallographic grinding and polishing equipment (Metkon Instruments FORCIPOL Metallographic Grinding & Polishing Machine).

Sandblasting

The clean 316L samples were each sandblasted for 60 seconds with silicon carbide (grit size 60) using sandblasting machinery (HBM sbc 110 blast cabin) at an incidence of 30 cm.

2.2.2 Preparation of Sodium Dihydrogen Phosphate Anhydrous solution

250 mL of deionised water was placed into a 1 L beaker (reaction vessel) on a heating stir plate. A 4 cm stir bar was added, and the solution was heated to the temperature specified by the DOE using a thermocouple while being stirred at a medium setting.

Sodium dihydrogen phosphate anhydrous (SDPA) was weighed according to the molarity specified by the DOE run and was added to the 1 L beaker and allowed to dissolve completely. The pH of this solution was then adjusted using the dropwise addition of 2M sodium hydroxide (NaOH) or 2M hydrochloric acid (HCl), depending on the pH required in the DOE run.

2.2.3 Preparation of Calcium Acetate Monohydrate solution

250 mL of deionised water was added to a clean, dry 1 L beaker containing a 4 cm stir bar and was stirred at a medium setting on a magnetic stir plate. This solution was not heated. Calcium acetate monohydrate (CAM) was weighed by the molarity specified by the DOE. This was added to the beaker and allowed to dissolve completely. The solution was then removed from the stir plate, and the stir bar was removed.

2.2.4 Reaction

Using clean forceps, three prepared 316L specimens were carefully placed at the bottom of the beaker containing the SDPA solution. Care was taken to place the specimens so that they would not interfere with the magnetic stir bar.

The peristaltic pump was calibrated to the flow rate specified in the DOE run. The inlet of the Marprene tubing was submerged in the CAM solution, while the outlet was placed at the centre of the mouth of the beaker containing the SDPA solution. The SDPA solution was allowed to reach the designated temperature before the peristaltic pump was switched on and the reaction commenced. The temperature and pH were monitored and kept constant throughout the reaction.

The reaction finished when the final drop of CAM had been added to the reaction vessel. The reaction vessel was then removed from the heat and the stir bar was carefully lifted from the beaker. At this point, digestion was carried out for the specified time in the DOE by leaving the reaction vessel to stand, covered by parafilm, for the specified time.

The 316L specimens were then carefully removed using clean forceps and placed on a glass tray. The remaining product was then filtered using a Buchner apparatus. The metallic specimens and the powdered product were placed in the oven to dry at 55°C for 48 hours or until the powder showed less than a 5% loss on drying. The powdered product was transferred to an airtight container and stored in a desiccator containing silica gel. The coated 316L samples were stored in 3 x 4 well plates.

2.2.5 Characterisation

The coated 316L specimens were then examined using SEM, EDX, XRD analysis, and optical profilometry (as described in sections 2.4.2, 2.4.3, and 2.4.4, respectively). All three samples in each run were measured three times for every analytical method. The mean results were then entered into the DOE.

2.2.6 Optimal Run

Following optimisation of the process using the DOE software, an optimal run was carried out by creating a coating on 316L samples using the optimal parameters as defined by the DOE. The optimal run is a proof-of-concept experiment to investigate if the optimal parameters determined by the DOE software produce the predicted optimal results. The optimal run samples were characterised using SEM, EDX, XRD, and optical profilometry (as described in sections 2.4.2, 2.4.3, and 2.4.4, respectively) to confirm the predictions of the DOE.

2.3 Degradation Study

2.3.1 Preparation of Hank's Balanced Salt Solution

A clean, dry 1 L beaker was placed on a magnetic stir plate. To this beaker, 800 mL of deionised water was added along with a magnetic stir bar and stirred until all reagents had completely dissolved. Once the solution had finished mixing, it was transferred to a clean, dry 1 L volumetric flask and made up to the mark with deionised water before being stopped and inverted. The prepared Hank's balanced salt solution (HBSS) was then transferred to a sterilised 1 L glass bottle and refrigerated until ready to use in degradation testing.

The reagents used in the preparation of HBBS are listed in Table . All reagents used in this process were supplied by Sigma-Aldrich.

Table 2: Reagents used in the production of HBSS.

Reagent	**Amount used (mg)**	**CAS number**
Sodium chloride	8000	7647-14-5
Potassium chloride	400	7447-40-7
Sodium bicarbonate	350	177-55-8
Magnesium chloride hexahydrate	100	7791-18-6
Magnesium sulfate heptahydrate	100	10034-99-8
Calcium chloride	140	10043-52-4
Disodium phosphate	60	7558-79-4
Potassium dihydrogen phosphate	60	7778-77-0
D-(+)-glucose	1000	50-99-7

2.3.2 Magnesium Sample Preparation

12 mm x 12 mm x 13 mm ingots of magnesium alloy WE43 were supplied by Dr Mert Celikin of the School of Mechanical and Materials Engineering, University College Dublin. The

magnesium ingots were cut into 24 samples of 12 mm x 12 mm x 3.25 mm with a hand-held saw before being mounted in epoxy resin (Araldite DBF Epoxy resin, TMQ) (Araldite HY951 Hardener, TMQ). The mounted samples were then ground with P60 SiC paper until the surface of the magnesium was exposed, before being wet ground with P800 and P1200 respectively for 120 seconds each to achieve the desired surface roughness Ra value of 0.28 µm. The samples were then placed in a solution of acetone and cleaned in an ultrasonic bath for 15 minutes before being rinsed with ethanol and dried to completion with a hairdryer to prevent oxidation of the magnesium sample. This process had no observable impact on the magnesium samples. The samples were then coated with OCP using the optimal method specified by the DOE. Prior to degradation testing, three coated samples were prepared for coating adhesion testing to examine the adhesion strength of the coating to the magnesium substrate.

2.3.3 Degradation Testing

Following the ASTM-G31-72 [187] standard to measure the degradation of magnesium when immersed in simulated physiological conditions, 20 mL of Hank's Balanced Salt Solution (HBSS), a buffered salt solution, is needed per 1 cm^2 of exposed magnesium. When mounted in resin, the exposed surface area of the magnesium samples was 1.44 cm^2. The volume of HBSS required to perform the degradation testing was 28.8 mL per sample. The samples were placed in polypropylene containers with 28.8 mL of HBSS and placed in an incubator at 37°C +/- 1 °C. According to the ASTM-G31-71 standard, there is no minimum required surface area of the metallic sample for this method.

The 24 samples were organised into two groups: uncoated and coated, with nine samples in each group undergoing degradation testing. Three coated and three uncoated samples were kept as undegraded controls for comparison. Each sample was uniquely labelled. The samples underwent degradation testing for seven days at three different time points: 24 hours, four days, and seven days. Three samples from each group were removed from the incubator at each time point, at which point the incubation medium was extracted from the container using a pipette and placed into a separate container ahead of analysis. The magnesium

samples were carefully removed, rinsed with deionised water and dried in the incubator before being examined.

2.3.4 Analysis

Before Degradation

Before coating the samples, the mass of each sample was measured using a mass balance (Mettler Toledo Standard LA Analytical Balance). The coated and uncoated samples were analysed before degradation testing using SEM, XRD, and optical profilometry (as described in sections 2.4.2, 2.4.3, 2.4.4, respectively). Adhesion strength testing was also conducted to determine the bond strength between the coating and the Mg substrate. The pH of the immersion medium for each sample was measured before and after the degradation.

Adhesion Testing

The tape test for coating adhesion was performed according to ASTM D3359-22 [188]. Following test method A, an X-cut (13 x 13 mm) was made through the coating to the magnesium specimen using a razor blade (ASTRA Superior Platinum, Amazon). Pressure-sensitive tape (CAPITOL Adhesive Tape, product code: 2306, CAPITOL) was applied over the cut and then removed. The quality of the adhesion is assessed on a 0-5 scale, as shown in Figure 14.

Classification		Surface of "X" - Cut from which flaking/peeling has occurred
5A	No peeling or removal	None
4A	Trace peeling or removal along incisions or at their intersection	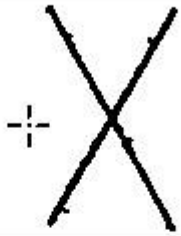
3A	Jagged removal along incisions up to 1/16" on either side	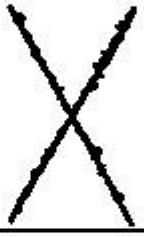
2A	Jagged removal along most of incisions up to 1/8" on either side	
1A	Removal from most of the area of the X under the tape	
0A	Removal beyond the area of the X	

Figure 14: Classification of adhesion test results for test method A [188].

2.3.5 Degradation of Magnesium by Mass Loss

After degradation, the corrosion products were removed by placing the samples in a chromic solution (200 g/L CrO_3 and 10 g/L $AgNO_3$) (Chromium (VI) oxide, CAS 1333-82-0, Sigma-Aldrich) (Silver nitrate, CAS 7761-88-8, Sigma-Aldrich) for 5 minutes in an ultrasonic bath at

room temperature, followed by rinsing with deionised water to remove the corrosion by-products before being left to dry at room temperature. The samples were then weighed using a mass balance. The mass of the samples before and after degradation were compared.

The average rate of degradation was measured by the loss of magnesium from the sample, which was determined using the following equation:

$$D_r = \frac{KW}{ATD}$$

Where D_r is the average rate of degradation (mm/year), K is a constant equal to 8.76 x 10^4, W is the mass loss of magnesium (g), A is the exposed surface area of the sample (cm^2), T is the exposure time of the sample to the HBSS (hours), and D is the density of the material (1.8 g/cm^2) [189], [190].

2.3.6 Analysis of Sample Surface

The surface of the degraded samples was analysed using SEM and XRD. The SEM was used to visualise the surface of the sample post-degradation and note any changes to the surface morphology that had occurred (as described in Section 2.4.2). XRD was used to determine any changes in the OCP coating during degradation (as described in section 2.4.3).

2.4 Characterisation

All samples fabricated as part of this project were analysed using the following methods. For each test method, three measurements were taken per sample. The results in this thesis are presented as the mean of three measurements.

2.4.1 ATR-FTIR

Attenuated Total Reflectance Fourier Transform Intra-Red spectroscopy (ATR-FTIR) (PerkinElmer Spectrum 2) analysis was carried out at the Nano Research Facility at DCU to assess the chemical composition of the calcium phosphate coatings. Spectral measurements were recorded over the wavelength range of 400–4000 cm^{-1}. The characteristic peaks for OCP are approximately 1000 cm^{-1}, 960 cm^{-1}, 600 cm^{-1}, 560 cm^{-1}, and 460 cm^{-1}. Each sample was analysed using the computer software of the ATR-FTIR equipment. The resulting spectrum was then examined by comparing characteristic peaks to those cited in the literature to identify key functional groups present in the powdered sample.

2.4.2 Scanning Electron Microscopy and Electron Dispersive X-Ray

The surface morphology and chemical composition of the samples were examined using a scanning electron microscope (SEM) with electron dispersive X-ray (EDX) equipment (Carl Zeiss LS15). The SEM images were taken and observed using the equipment software at 15 kV, while the EDX spectra were analysed using the Point & ID method on AZtecOne (Oxford Instruments) software.

2.4.3 X-ray Diffraction

The phase compositions of the samples were determined using X-ray diffraction with Cu Kα ($\lambda = 0.154$ nm) in a 2θ scanning range of 3.5° to 40°.

All XRD spectra were analysed using Profex software (version 4.3.6) using the software database and compared further to existing literature to confirm the results.

The coated stainless steel samples produced from the DOE were analysed using XRD (Bruker D8 Discovery) at the Applied Physics Research Group at Trinity College Dublin by Dr David Caffrey. The coated stainless steel samples from the optimal run and the coated magnesium samples were analysed using XRD (Bruker D2 Phaser 2nd Gen) at PBC Biomed Ltd in Shannon, Co. Clare.

2.4.4 Optical Profilometry

The surface roughness of the uncoated samples (Ra, µm) and the coating thickness (µm) of the coated samples were obtained using optical profilometry (Bruker Contour GT Optical Profilometer) and analysed using Version64 Map software at the Nano Research Facility at DCU. The samples were analysed using the parameters listed in Table 1. The surface roughness was obtained by quantifying the Ra value, which measures the average deviation from the mean line in a 2D field. The coating thickness was determined from Sa values, which measure the average deviation from the mean line in a 3D field. The coating profile consists of peaks and valleys. Assuming the bottom of the valleys reaches the surface of the implant, the coating thickness can be estimated from the average deviation from the mean line at the bottom of the valleys.

Table 3: Optical profilometry scanning parameters.

Processing Method	VSI
Magnification	5X
Speed	1X
Backscan (μm)	500
Length (μm)	500
Threshold	5%

3 Chapter 3: Results and Discussion

3.1 Octacalcium Phosphate Synthesis

3.1.1 ATR-FTIR

The ATR-FTIR spectrum of a typical sample of OCP powder is shown in Figure 15. The peaks from the graph were compared to the spectra of OCP from the literature to identify the sample. All the peaks labelled in Figure 15 below correspond to the P-O bonds present in the phosphate groups in octacalcium phosphate [$Ca_8H_2(PO_4)_6 \cdot 5H_2O$].

Symmetric stretching, asymmetric stretching, symmetric bending, and asymmetric bending are the four fundamental vibrational modes for phosphate groups [191]. Any tetrahedral molecules or ions, such as the phosphate ion, will exert four vibrational overtones (v1, v2, v3, v4). In the infrared spectrum, the vibrational overtone bands are multiples of the fundamental absorption frequency. The peak at 1024 cm^{-1} is due to the asymmetric stretching of the phosphate group (v3). The peak at 960 cm^{-1} is due to the symmetric stretching vibration (v1), while the peaks at 560 cm^{-1} and 600 cm^{-1} are due to bending vibrations in the v4 degenerate state. A peak at approximately 460 cm^{-1} corresponds to the bending vibration (v2) in the phosphate ion. However, this peak is not strong on the FTIR spectrum for this sample. This may be due to water present in the sample, which can lead to skewed spectra [191], [192], [193], [194].

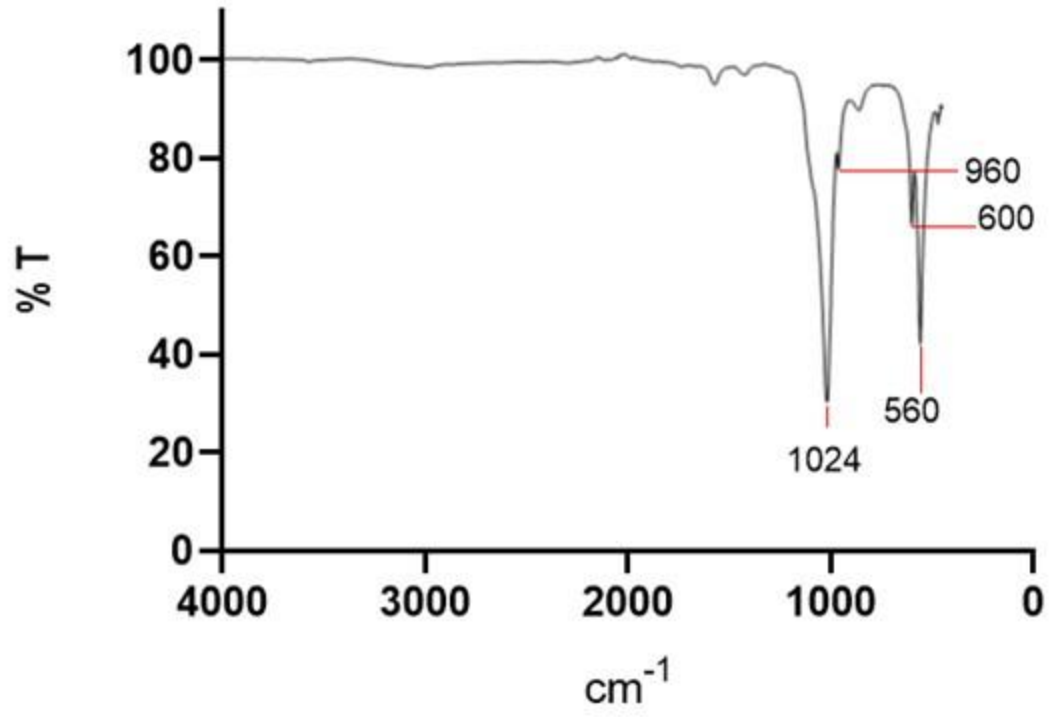

Figure 15: ATR-FTIR spectrum of OCP synthesised in-house.

3.1.2 SEM

As seen in Figure 16 and Figure *17*, a combination of plate and needle-like crystals make up the particle morphology of the OCP powder. The particle morphology of OCP and most calcium phosphates can be strongly influenced by the conditions in which it is synthesised. Barrère *et al.* [195] precipitated OCP on a titanium alloy plate by immersing it in a simulated body fluid solution, showing that the OCP particles had a vertically arranged plate-like morphology. The crystals grew larger and sharper with increased soaking time. In some areas of the OCP coating, the crystals formed a "rosette". Bigi *et al.* [196] reported that OCP was synthesised by the dropwise addition of $Ca(CH_3COO)_2$ to a solution containing Na_2HPO_4 and NaH_2PO_4 at a pH of 5. The resulting crystals had a thin, needle-like morphology in the SEM micrographs. Suzuki *et al.* described the crystal morphology of OCP produced by the LeGeros method as "small acicular and frequently mixed with aggregates of short platy crystals" [157]. The particle morphology observed here agrees with the findings of Suzuki *et al.*, confirming that this method produces OCP with a crystal morphology of mixed needle and plate-like crystals.

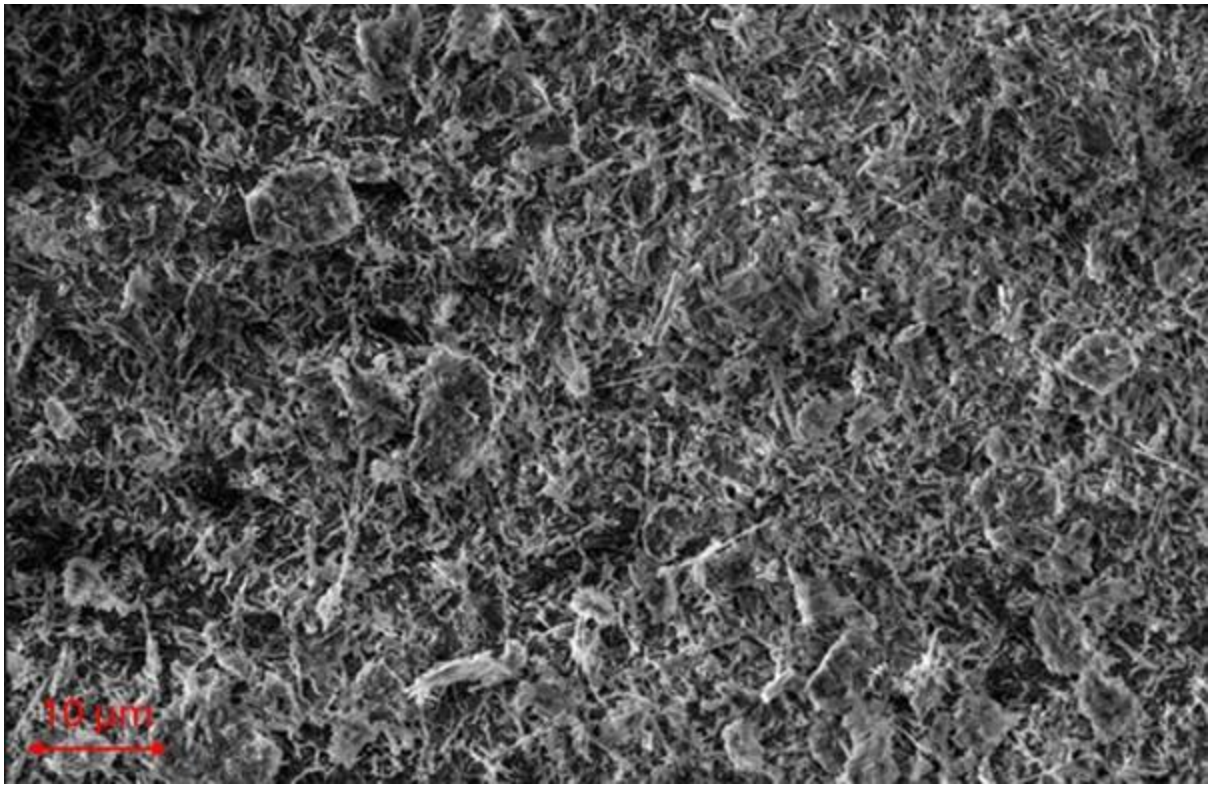

Figure 16: SEM image of OCP synthesised in-house, at 500 X magnification.

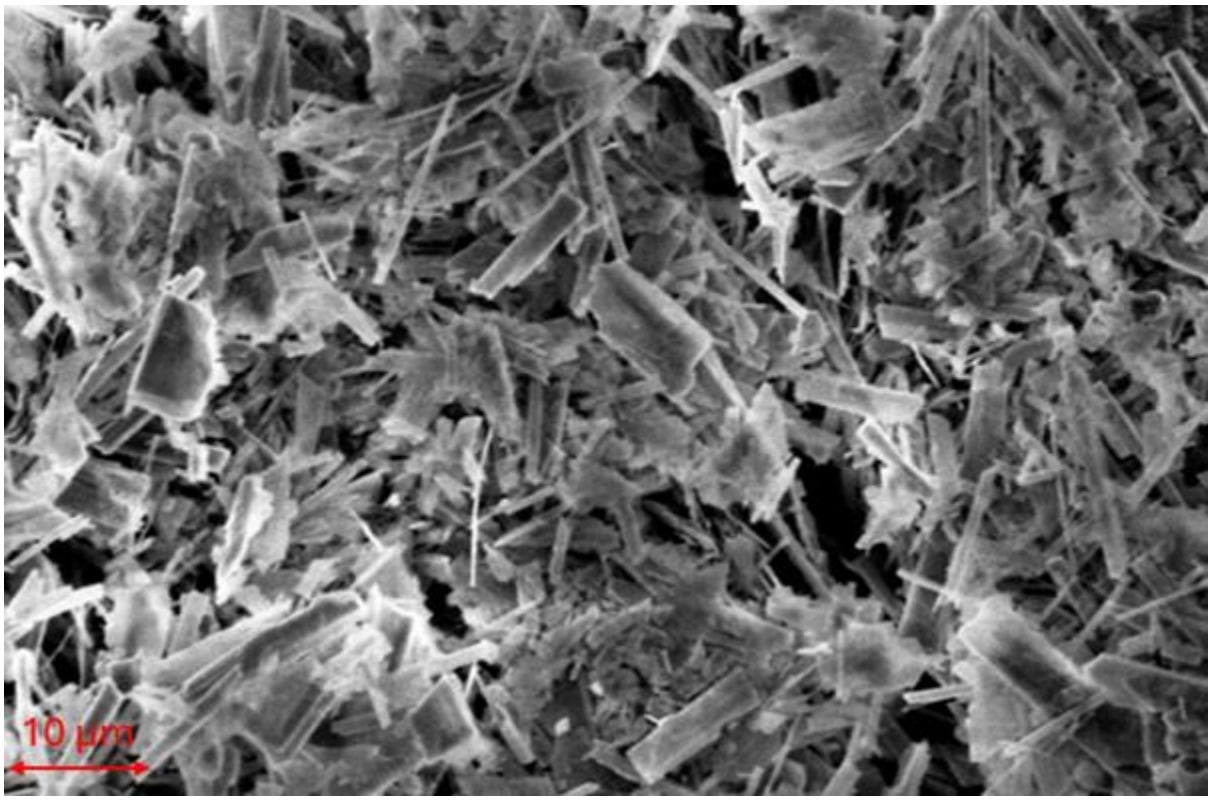

Figure 17: SEM image of OCP synthesised in-house, at 5000 X magnification.

3.2 Design of Experiment Study

Table 1 shows the results for each run in the DOE study. For this study, 316L samples were used as it was a cost-effective alternative to magnesium for the large number of samples used. 316L is also commonly used as an orthopaedic implant material. Three samples in each run were measured three times each for every analytical method – the results presented are the mean values of the data gathered.

Table 1: Responses for each run in the DOE study. The results presented are the mean value of three measurements.

	Inputs						Responses		
Run	**Temp. (°C)**	**pH**	**Conc. (mol/L)**	**Flow Rate (mL/min)**	**Digestion (hr)**	**Surface Roughness**	**OCP (%)**	**Ca:P**	**Thickness (µm)**
1	70	4	0.04	2	0.5	Medium	0 ±0	0.836 ±0	0.910 ±0.204
2	53.5	7	0.06	4	0	Medium	62.3 ±0	1.057 ±0	0.681 ±0.189
3	53.5	4	0.04	4	1	Low	55 ±0	0.941 ±0	0.809 ±0.196
4	37	5.5	0.06	4	0.5	High	41 ±0	0.941 ±0	52.770 ±9.121
5	53.5	5.5	0.06	6	0.5	Low	19 ±0	1.113 ±0	1.502 ±0.895
6	37	5.5	0.04	2	1	Medium	0 ±0	1.13 ±0	16.428 ±3.112
7	53.5	5.5	0.06	2	0.5	High	54.3 ±0	1 ±0	2.415 ±0.684
8	53.5	5.5	0.06	2	0.5	Low	62 ±0	1.312 ±0	42.674 ±2.418
9	53.5	5.5	0.04	4	0.5	Medium	59.4 ±0	1.178 ±0	2.0448 ±0.857
10	70	5.5	0.04	2	1	Medium	59 ±0	0.767 ±0	4.498 ±1.291
11	70	7	0.04	2	0.5	Medium	38 ±0	1.2 ±0	1.870 ±0.706
12	53.5	4	0.04	4	0	High	50.8 ±0	0.952 ±0	2.520 ±0.898
13	70	5.5	0.04	6	1	Medium	60.2 ±0	1.238 ±0	0.836 ±0.154

14	53.5	4	0.04	4	0	Low	54 ±0	0.836 ±0	0.537 ±0.191
15	70	5.5	0.02	4	0.5	Low	69 ±0	1.241 ±0	3.892 ±0.929
16	53.5	4	0.06	4	0	Medium	0 ±0	0 ±0	4.241 ±1.094
17	70	5.5	0.06	4	0.5	Low	81 ±0	1.245 ±0	24.968 ±3.277
18	53.5	7	0.02	4	1	Medium	61 ±0	0.3 ±0	1.581 ±0.339
19	37	7	0.04	6	0.5	Medium	44 ±0	1.175 ±0	14.342 ±4.187
20	70	5.5	0.04	6	0	Medium	32 ±0	1.026 ±0	2.178 ±0.693
21	53.5	5.5	0.02	6	0.5	High	57 ±0	0.856 ±0	2.976 ±0.881
22	37	4	0.04	2	0.5	Medium	0 ±0	0 ±0	5.705 ±1.076
23	53.5	7	0.04	4	0	High	20 ±0	1.151 ±0	6.163 ±1.831
24	53.5	4	0.06	4	1	Medium	0 ±0	1 ±0	38.016 ±5.233
25	70	4	0.04	6	0.5	Medium	60.2 ±0	0.937 ±0	7.336 ±1.145
26	53.5	7	0.04	4	0	Low	71 ±0	1.346 ±0	6.593 ±2.210
27	70	5.5	0.04	2	0	Medium	50.3 ±0	0.315 ±0	6.958 ±1.084
28	53.5	7	0.06	4	1	Medium	95.2 ±0	1.23 ±0	7.255 ±2.199
29	53.5	7	0.04	4	1	High	73 ±0	1.058 ±0	7.728 ±1.162
30	53.5	5.5	0.02	6	0.5	Low	0 ±0	1 ±0	7.574 ±2.123
31	37	5.5	0.04	2	0	Medium	0 ±0	1 ±0	10.39 ±3.250
32	53.5	7	0.04	4	1	Low	67 ±0	0.718 ±0	7.983 ±1.094
33	53.5	4	0.02	4	0	Medium	0 ±0	0.882 ±0	8.455 ±1.160
34	53.5	5.5	0.02	2	0.5	High	34 ±0	1.4 ±0	13.996 ±2.387
35	53.5	7	0.02	4	0	Medium	43 ±0	0.881 ±0	8.969 ±2.107
36	37	5.5	0.04	6	0	Medium	71 ±0	0.959 ±0	3.086 ±0.997

37	53.5	4	0.04	4	1	High	31 ±0	0.975 ±0	9.706 ±2.091
38	37	5.5	0.02	4	0.5	Low	40 ±0	0.826 ±0	9.834 ±0.686
39	70	5.5	0.02	4	0.5	High	0 ±0	0.936 ±0	11.281 ±1.103
40	53.5	5.5	0.04	4	0.5	Medium	0 ±0	1.107 ±0	15.916 ±3.131
41	70	5.5	0.06	4	0.5	High	0 ±0	1.217 ±0	2.263 ±1.080
42	37	4	0.04	6	0.5	Medium	0 ±0	0.817 ±0	1.248 ±0.647
43	37	5.5	0.02	4	0.5	High	0 ±0	0.936 ±0	11.478 ±4.299
44	37	5.5	0.04	6	1	Medium	49.5 ±0	0.861 ±0	11.673 +2.169
45	53.5	5.5	0.06	6	0.5	High	58 ±0	1.056 ±0	11.499 +2.148
46	70	7	0.04	6	0.5	Medium	20 ±0	0.68 ±0	11.595 +0.201
47	53.5	4	0.02	4	1	Medium	14.6 ±0	0.814 ±0	11.967 ±0.204
48	37	7	0.04	2	0.5	Medium	20 ±0	0.6422 ±0	12.177 ±5.190
49	37	5.5	0.06	4	0.5	Low	66.3 ±0	1.274 ±0	16.015 ±3.211
50	53.5	5.5	0.02	2	0.5	Low	63 ±0	1.26 ±0	15.600 ±4.197
51	53.5	5.5	0.04	4	0.5	Medium	46.8 ±0	1.245 ±0	2.050 ±0.181

3.2.1 Response 1: %OCP

ANOVA

Table 2 depicts the analysis of variance (ANOVA) for the response %OCP using a linear model. This table shows the impact each input had on the percentage of OCP in the coating, excluding the interactions between inputs. The impact, or significance, of an input is calculated from the p-value. An input p-value of less than 0.05 indicates that the input has a significant effect on the response, and a model p-value of less than 0.05 indicates that the model is significant.

Table 2: Analysis of variance (ANOVA) of the response of %OCP.

Source	Sum of Squares	Mean Square	F-value	p-value	
Model	9921.93	1653.66	2.57	0.0321	significant
A-Temperature	792.35	792.35	1.23	0.2733	
B-pH	5072.13	5072.13	7.88	0.0074	
C-Concentration	1033.59	1033.59	1.61	0.2118	
D-Flow Rate	339.75	339.75	0.5277	0.4714	
E-Digestion Time	514.30	514.30	0.7988	0.3763	
F-Surface Roughness	2169.80	2169.80	3.37	0.0732	
Residual	28329.64	643.86			
Lack of Fit	26370.52	627.87	0.6410	0.7780	not significant
Pure Error	1959.12	979.56			
Cor Total	38251.58				

The pH had a p-value of 0.0074, suggesting that it was the only input that had a significant effect on the percentage of OCP in the coating. The surface roughness had a p-value of 0.0732, suggesting that it had a moderate effect on the percentage of OCP in the synthesised powder. Values greater than 0.1 indicate that the model inputs are not significant. Therefore, considering the ranges explored in this experiment, the temperature, concentration, flow rate, and digestion time did not significantly affect the percentage of OCP in the coating. The

model suggested that there were no interactions between the inputs that significantly impacted the results.

The Model F-value of 2.57 implies the model is significant. There is only a 3.21% chance that an F-value this large could occur due to noise. The Lack of Fit F-value of 0.64 implies the Lack of Fit is not significant relative to the pure error. There is a 77.80% chance that a Lack of Fit F-value this large could occur due to noise.

Fit Statistics

As evident in Table 3, the predicted R^2 of 0.0047 is in reasonable agreement with the adjusted R^2 of 0.1584; i.e. the difference is less than 0.2. Adeq Precision measures the signal-to-noise ratio. The ratio of 6.101 indicates an adequate signal.

Table 3: Fit statistics of the response of percentage OCP.

Std. Dev.	25.37	**R^2**	0.2594
Mean	38.29	**Adjusted R^2**	0.1584
C.V. %	66.27	**Predicted R^2**	0.0047
		Adeq Precision	6.1006

Model Graphs

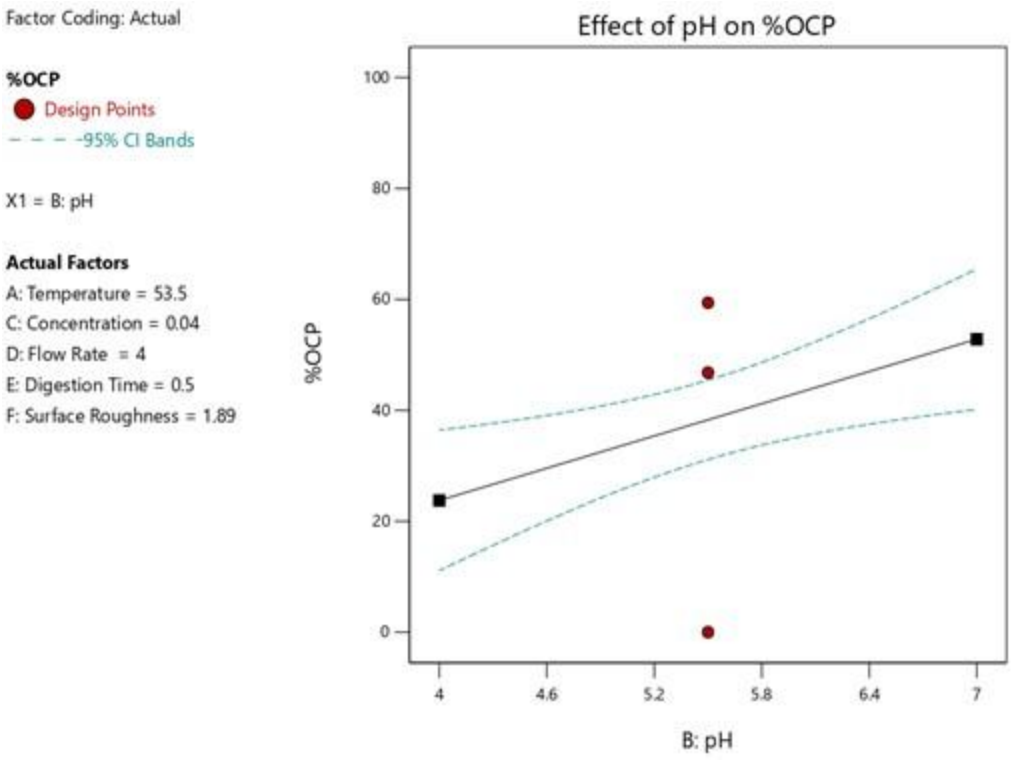

Figure 18: Effect of pH on %OCP.

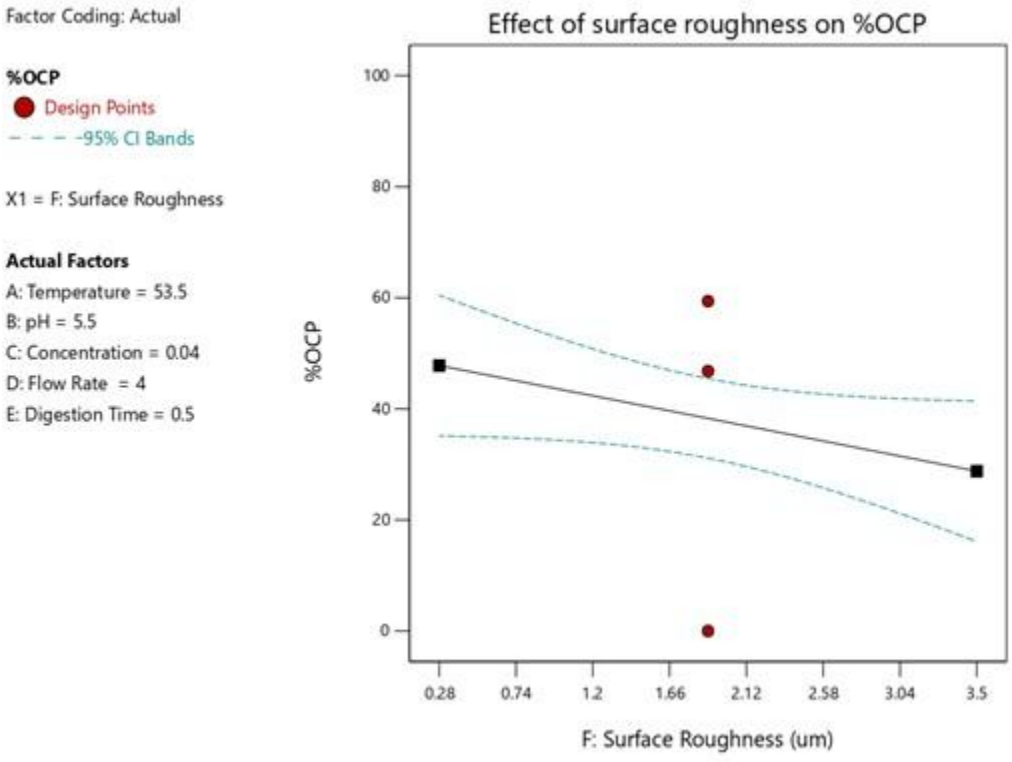

Figure 19: Effect of surface roughness on % OCP.

The model graphs in Figure 18 and Figure 19 illustrate the effect of the pH and surface roughness on the percentage of OCP. The results of this study suggest that the percentage of OCP in the coating increases with the pH of the solution and decreases with the surface roughness value of the implant. The effect of pH on the formation of calcium phosphates has been documented in the literature, and the results of this study agree with the consensus that at higher pH values, the supersaturation of OCP is higher due to the retrograde solubility of OCP, resulting in the precipitation of OCP.[197], [198]

The graph shows that %OCP increases when surface roughness decreases – indicating that the surface roughness of the implant influences the %OCP. The results of the DOE study indicate that the coatings on the as-machined substrates with no surface modifications had the highest % of OCP in their coating. It is widely accepted in the literature that an increase in the surface roughness of an implant increases the phase purity of the calcium phosphate coating applied [199], [200]. The increased surface roughness can increase nucleation sites for OCP and lead to a more favourable interfacial energy, facilitating the formation of phase-pure OCP. However, it has been suggested that the corrosion products on 316L can hinder the formation of calcium phosphates *in vitro* [201], [202]. As 316L produces an oxide layer on its surface that protects it to a degree from corrosion, the removal of this oxide layer from surface treatments may lead the 316L samples to corrode in the immersion solution, releasing ions and corrosion products that affected the phase purity of the surrounding OCP and prevented the formation of a homogenous OCP coating.

3.2.2 Response 2: Ca:P Ratio

ANOVA

Table 4 shows the ANOVA for the response of the Ca:P ratio using a reduced quadratic model suggested by the software. According to the p-values, the responses of B, BC, BE, CE, B^2, and F^2 are significant, meaning the surface roughness, the interaction between concentration and digestion time, and the pH and its interactions with concentration and digestion time had a significant influence on the Ca:P ratio of the coating. The p-values of B^2 and F^2 indicate that

both pH and surface roughness had a non-linear influence on the Ca:P ratio. The p-value of CE indicates that the effect of concentration on the Ca:P ratio changes depending on the digestion time, and vice versa. The p-values of BC and BE indicate that the effect of pH on the Ca:P ratio changes depending on the concentration and digestion time, and vice versa.

Table 4: ANOVA for the response of Ca:P Ratio.

Source	Sum of Squares	df	Mean Square	F-value	p-value	Significance
Model	2.29	9	0.2542	4.69	0.0003	significant
B-pH	0.2498	1	0.2498	4.61	0.0378	
C-Concentration	0.0516	1	0.0516	0.9522	0.3349	
E-Digestion Time	0.0163	1	0.0163	0.3010	0.5862	
F-Surface Roughness	0.0168	1	0.0168	0.3094	0.5811	
BC	0.4060	1	0.4060	7.49	0.0091	
BE	0.2996	1	0.2996	5.53	0.0236	
CE	0.4148	1	0.4148	7.65	0.0085	
B^2	0.3033	1	0.3033	5.60	0.0228	
F^2	0.3134	1	0.3134	5.78	0.0208	
Residual	2.22	41	0.0542			
Lack of Fit	2.21	39	0.0567	11.98	0.0799	not significant
Pure Error	0.0095	2	0.0047			
Cor Total	4.51	50				

The Model F-value of 4.69 implies the model is significant. There is only a 0.03% chance that an F-value this large could occur due to noise. The Lack of Fit F-value of 11.98 implies there is a 7.99% chance that a Lack of Fit F-value this large could occur due to noise. This relatively low probability (<10%) suggests that there is unexplained variation in the model. However, a low pure error value (0.0095), a low lack of fit p-value (0.0799), and a model p-value of 0.0003 indicate that the model is adequate, and the major effects and interactions are captured.

Fit Statistics

Table 5: Fit statistics of the response of Ca:P ratio.

Std. Dev.	0.2328	**R^2**	0.5072
Mean	0.9581	**Adjusted R^2**	0.3991
C.V. %	24.30	**Predicted R^2**	0.3349
		Adeq Precision	11.2737

The Predicted R^2 of 0.3349 is in reasonable agreement with the Adjusted R^2 of 0.3991. The Adeq Precision ratio of 11.274 indicates an adequate signal. Therefore, this model can be used to navigate the design space.

Model Graphs

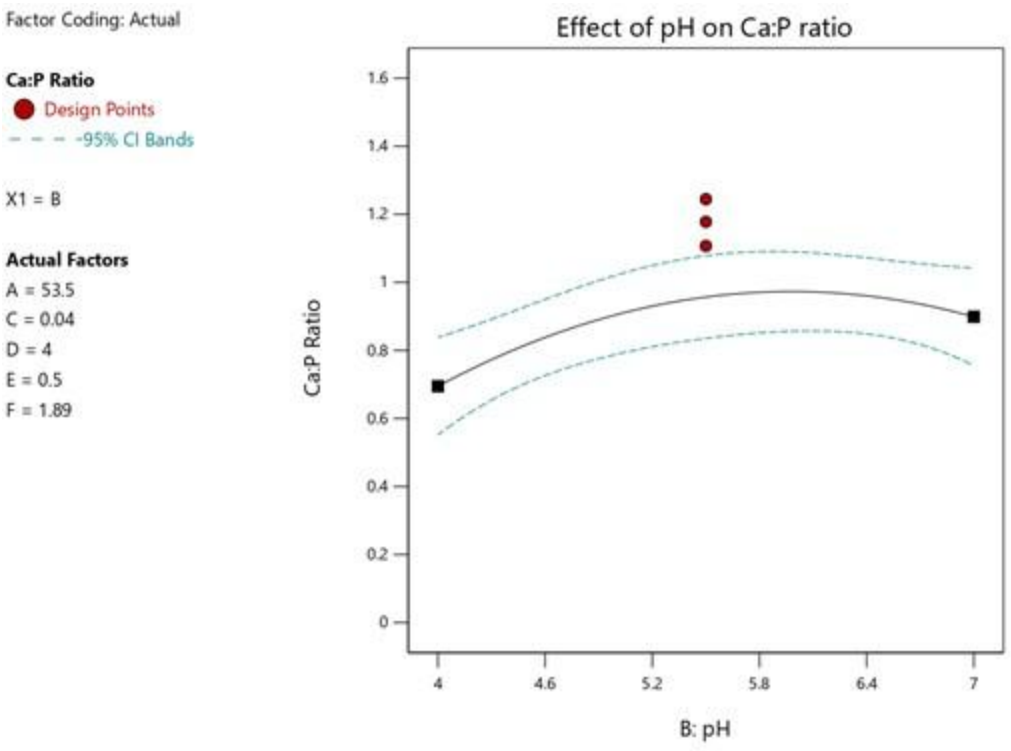

Figure 20: Effect of pH on Ca:P ratio.

Figure 20 shows the relationship between the pH of the immersion solution and the Ca:P ratio of the coating produced. The graph indicates a curved response that suggests a quadratic

relationship, which is evident from Table 4. This suggests that both too low and too high pH values adversely affect the Ca:P ratio, as the Ca:P ratio reaches its maximum point at approximately pH 5.8.

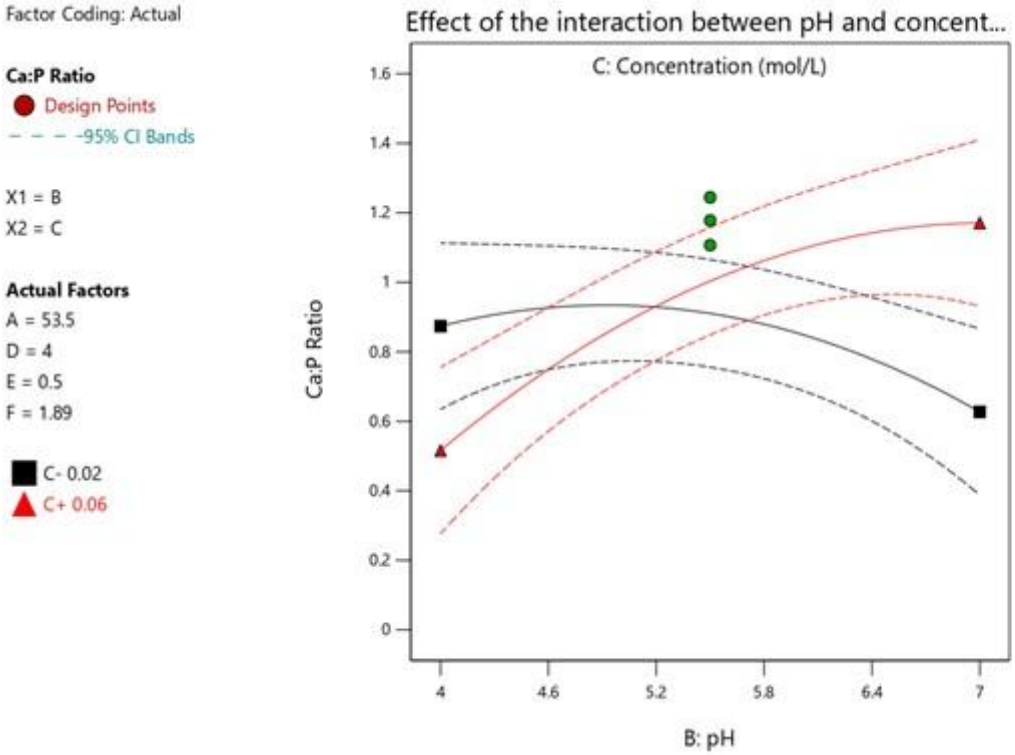

Figure 21: Effect of the interaction between pH and concentration on Ca:P ratio.

Figure 21 shows the interaction between pH and concentration and the influence it has on the Ca:P ratio. As evident from the graph, when the pH is at the lower level of 4, higher concentration (red triangles) leads to a lower Ca:P ratio and a lower concentration (black squares) leads to a higher Ca:P ratio. When pH is high, the opposite is true – a higher concentration gives better results. The lines on the graph intersect around pH 5.2-5.8, showing where this switch occurs. The best results of a Ca:P ratio of 1.33 are achieved by using a high pH with a high concentration, which is supported by the literature [163], [174], [181], [197].

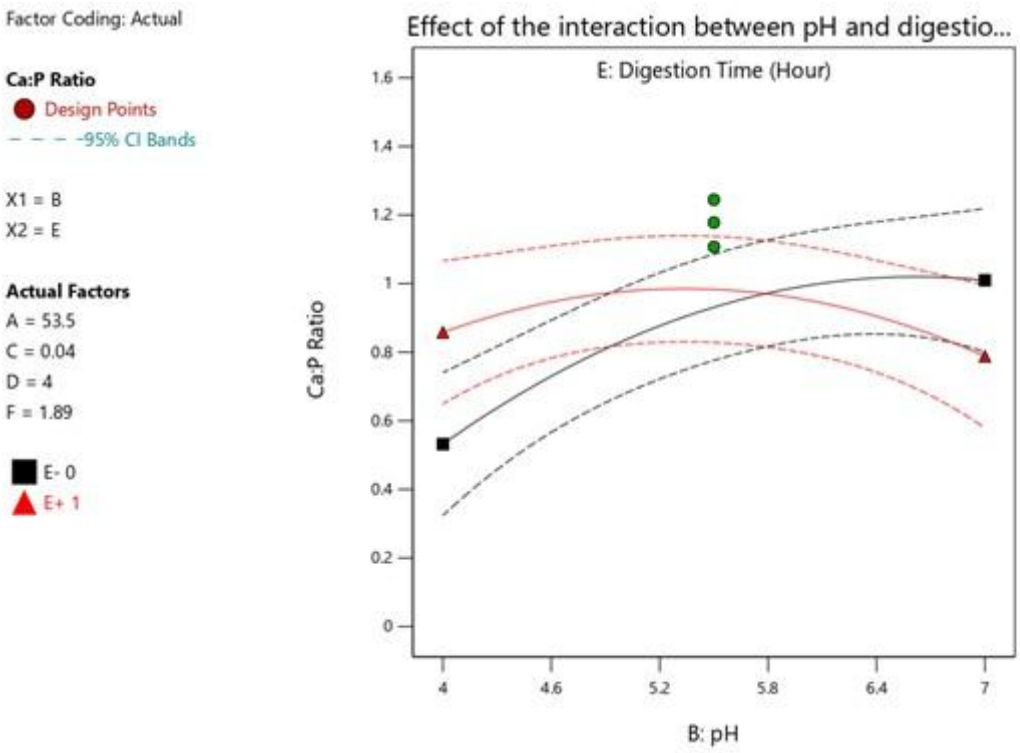

Figure 22: Effect of the interaction between pH and digestion time on the response of Ca:P ratio.

Figure 22 shows the effect of the interaction between pH and digestion time on the response of the Ca:P ratio. When pH is low, a longer digestion time (red triangles) leads to a higher Ca:P ratio, while a shorter digestion time (black squares) results in a lower Ca:P ratio. At higher pH values, the opposite is true. The lines intersect at approximately pH 5.8, indicating a critical transition point – at pH 5.8, the highest Ca:P ratios are observed. The design points (green circles) at pH 5.8 validate the reliability of these results. As well, the confidence intervals (dashed lines) are the narrowest in this region, indicating greater prediction liability.

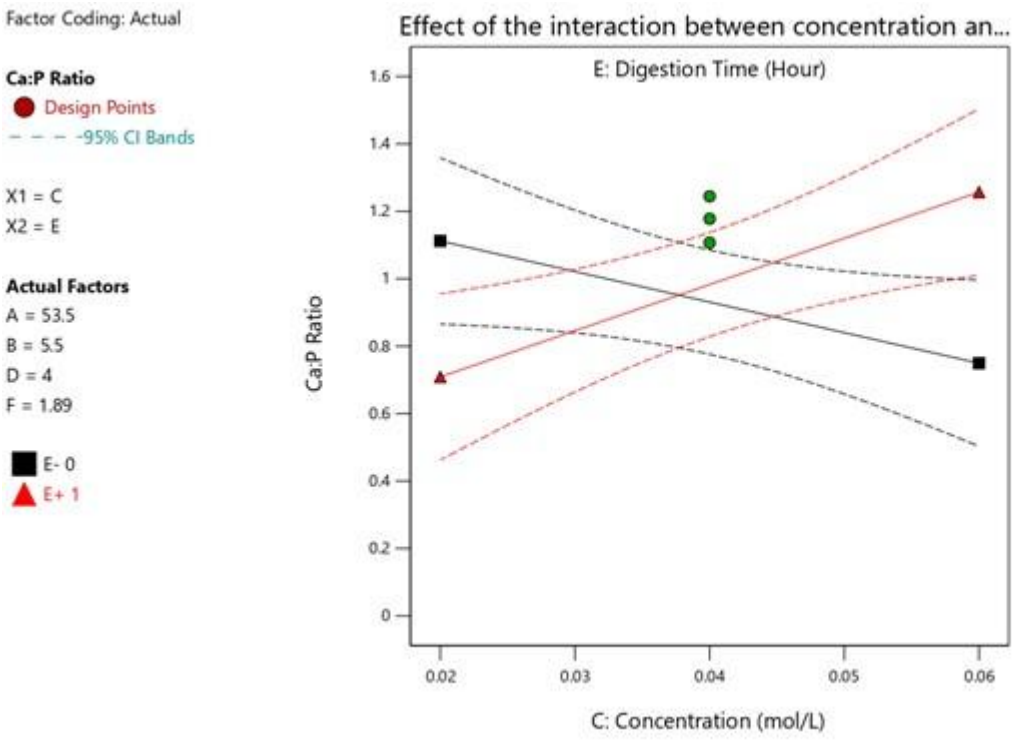

Figure 23: Effect of the interaction between concentration and digestion time on Ca:P ratio.

Figure 23 shows the interaction between concentration and digestion time and its effect on the Ca:P ratio. The graph dictates that at low concentrations (0.02 mol/L), shorter digestion time (black squares) result in a higher Ca:P ratio, and longer digestion time (red triangles) leads to a lower Ca:P ratio. At high concentrations (0.06 mol/L), the trend reverses completely – longer digestion time yields a higher Ca:P ratio and shorter digestion times result in a lower Ca:P ratio. The lines intersect at approximately 0.04 mol/L, suggesting a concentration point where the digestion time has minimal effect. The design points are clustered close to this region, validating the reliability of these results.

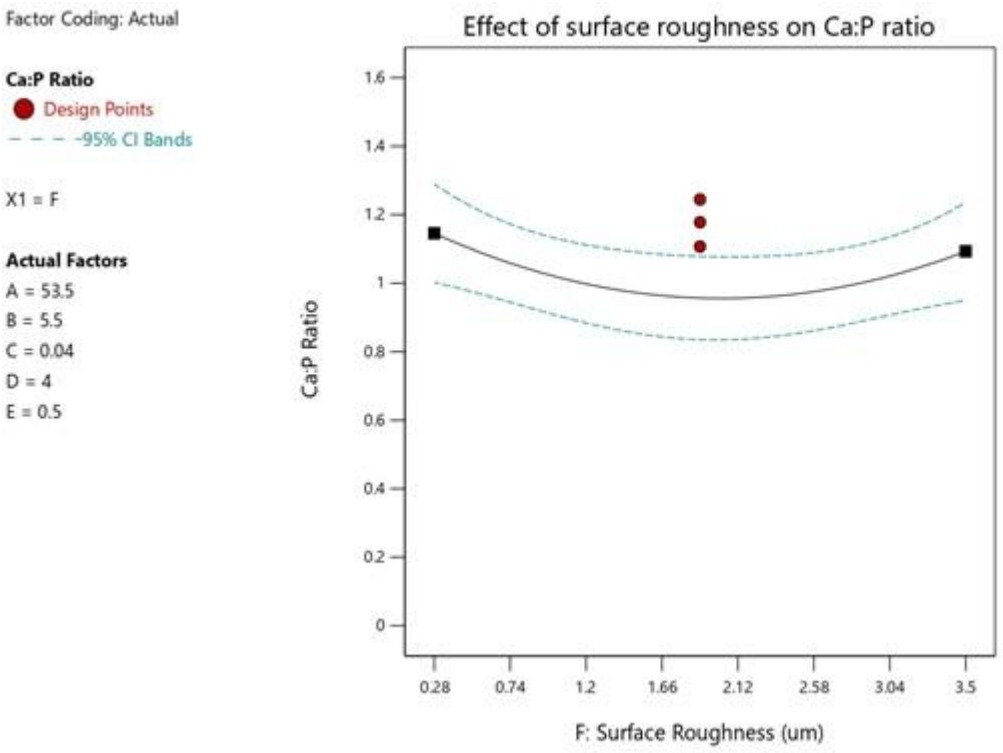

Figure 24: Effect of surface roughness on Ca:P ratio.

The graph in Figure 24 shows the quadratic relationship between surface roughness and Ca:P ratio. The graph shows a subtle U-shaped curve where both very low (0.28 µm, untreated) and very high (3.5 µm, grit-blasted) surface roughness values yield higher Ca:P ratios. However, the design points (red circles) show that the highest Ca:P ratios were obtained at the mid-range surface roughness value (1.89 µm, p60 SiC paper). This discrepancy between the model's prediction (black curve) and the actual experimental data (red circles) suggests that the model is not accurately capturing what occurs at this surface roughness. While it has been established in the literature that the surface roughness of a biomedical implant can have a significant impact on the adhesion of and interaction with calcium phosphate coatings, there is also information to suggest that the surface roughness of an implant can have an impact on the calcium phosphate ratio of the calcium phosphate coating. It has been suggested that an increase in the implant surface area can provide for nucleation sites for calcium phosphate crystal growth, which can in turn increase the Ca:P ratio [203]. The results in Figure 24: Effect of surface roughness on Ca:P ratio. suggest that the Ca:P is highest for the sand-blasted samples, which concurs with the finders of Hung *et. al.* (2017) [204].

3.2.3 Response 3: Coating Thickness

ANOVA

Table 6 shows the ANOVA for the response of the coating thickness using a reduced quadratic model suggested by the software.

Table 6: ANOVA for the response of the coating thickness.

Source	Sum of Squares	df	Mean Square	F-value	p-value	Significance
Model	2414.26	9	268.25	3.62	0.0021	significant
A-Temperature	312.20	1	312.20	4.21	0.0465	
C-Concentration	389.63	1	389.63	5.26	0.0270	
D-Flow Rate	139.10	1	139.10	1.88	0.1781	
E-Digestion Time	138.75	1	138.75	1.87	0.1786	
F-Surface Roughness	0.4229	1	0.4229	0.0057	0.9401	
AF	360.66	1	360.66	4.87	0.0330	
CE	244.51	1	244.51	3.30	0.0766	
DF	279.20	1	279.20	3.77	0.0591	
C^2	549.78	1	549.78	7.42	0.0094	
Residual	3037.80	41	74.09			
Lack of Fit	2909.59	39	74.60	1.16	0.5687	not significant
Pure Error	128.22	2	64.11			
Cor Total	5452.07	50				

The Model F-value of 3.62 implies the model is significant. There is only a 0.21% chance that an F-value this large could occur due to noise. The Lack of Fit F-value of 1.16 implies the Lack of Fit is not significant relative to the pure error. There is a 56.87% chance that a Lack of Fit F-value this large could occur due to noise.

According to the p-values listed in the ANOVA in Table 6, the temperature (A), concentration (C), and quadratic effect of concentration (C^2) have a significant influence on the coating thickness, as does the temperature-surface roughness interaction (AF). The concentration-digestion time (CE) and flow rate-surface roughness interactions showed marginal significance (p=0.0766 and p=0.0591, respectively).

Fit Statistics

Table 7: Fit statistics for the response of coating thickness.

Std. Dev.	8.61	**R^2**	0.4428
Mean	9.51	**Adjusted R^2**	0.3205
C.V. %	90.48	**Predicted R^2**	-0.0018
		Adeq Precision	7.6646

The standard deviation (Std. Dev.) listed in Table 7 has a value of 8.61, indicating that there is high variability in the measurements. The Mean suggests that the average coating thickness over all the experimental responses was 9.51 µm. The coefficient of variation (C.V.%) is 90.48%, which indicates the model had a high variability of coating thickness concerning the mean. This high variation, combined with the Std. Dev. Of 8.61, suggests that the coating thickness is influenced by factors beyond the scope of this model. The R^2 value (0.4428) suggests that the model explains less than half (44.28%) of the variation in responses. When accounting for model complexity, the Adjusted R^2 only accounts for 32.05% of the variation. A negative Predictive R^2 value suggests that the reduced quadratic model used here has poor predictive ability on the results. These findings suggest that although the model identifies some important factors and relationships, the coating thickness control may require the consideration of additional factors or process modifications to improve predictability and reduce variability.

However, despite the limitation of inadequate fit statistics, the overall model is highly significant (p=0.0021) and the lack of fit is insignificant (p=0.5687). Also, the adequate precision (7.66) is above the desired threshold of 4, meaning the model can be used to navigate the design space. Changing to a more complex model, such as a cubic model, could carry the risk of overfitting the data, creating aliasing issues, and making the interpretation of the data more complicated. Similarly, a simpler linear model would ignore the significant quadratic effect (C^2) and input interactions (AF). In summary, a quadratic model was chosen to analyse the coating thickness as it captures important input interactions and effects, and the high C.V.% suggests inherent process variation that would not change with a different

model. This inherent process variation may suggest that the thickness of an implant surface coating depends more on the process with which it is coated than the inputs of the process itself.

Model Graphs

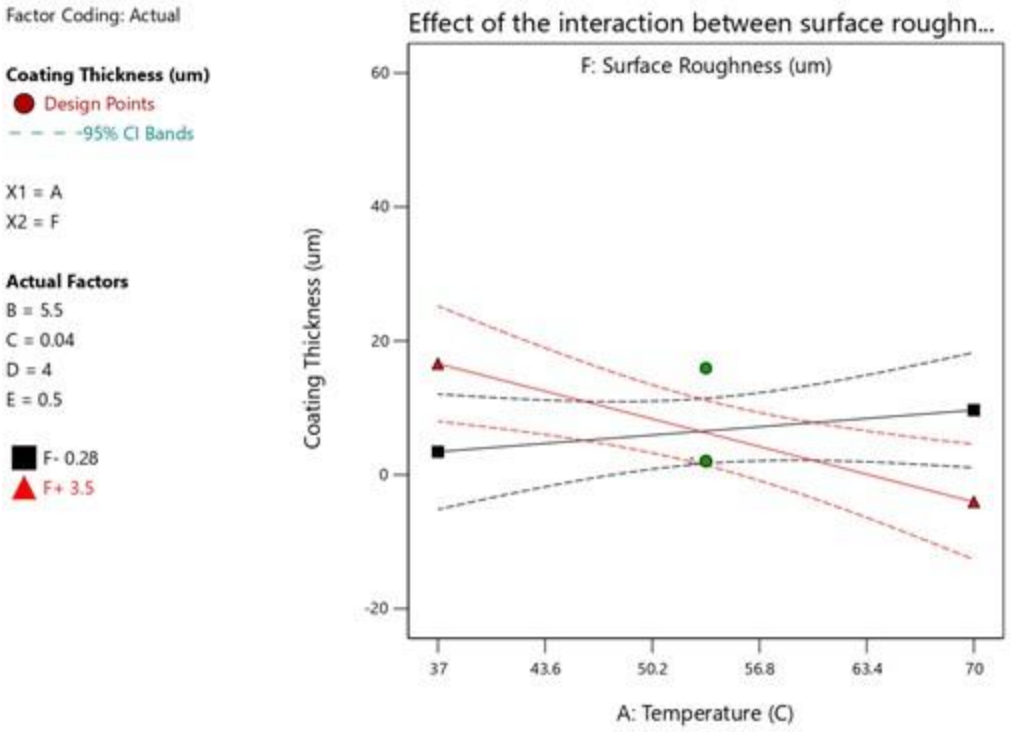

Figure 25: Effect of the interaction between the surface roughness and temperature on the response of the coating thickness.

Figure 25 shows the interaction between the surface roughness and temperature and the effect on the coating thickness. This plot indicates that at high surface roughness (3.5 µm, red triangles), the coating thickness decreases significantly with increasing temperature. At low surface roughness (0.28 µm, black squares), the coating thickness slightly increases with an increase in temperature. The intersection of the lines at 50.2 °C confirms the statistical significance of this interaction and indicates a critical transition point. This plot suggests that the choice of surface roughness should be guided by the operating temperature of the coating process and that operating at the temperature of 50.2 °C may minimise the effects of surface roughness on the coating thickness.

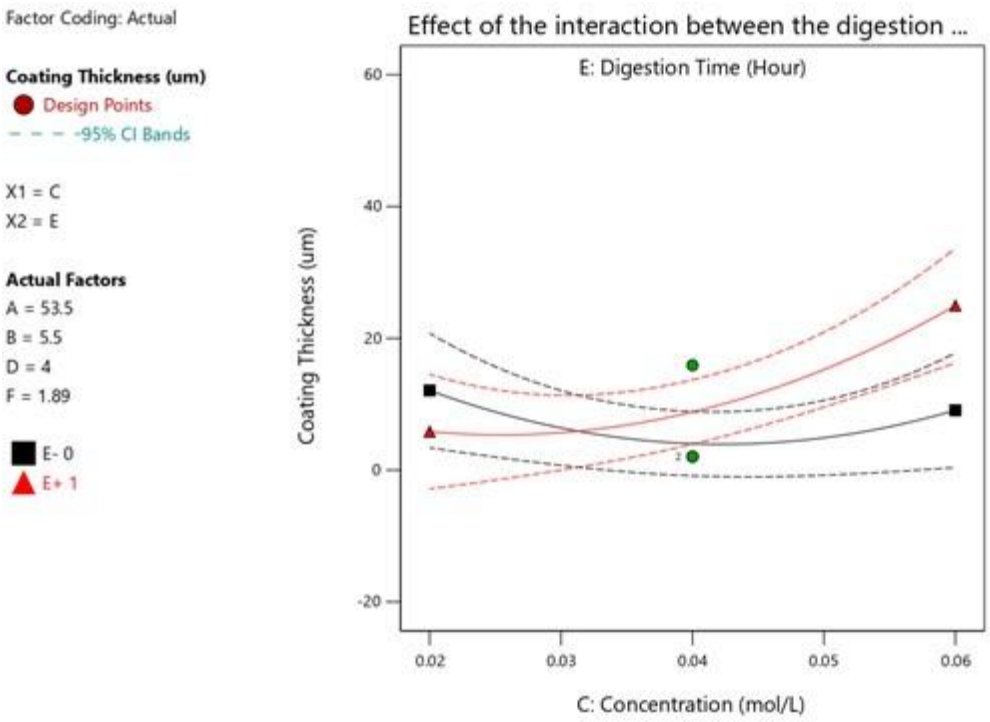

Figure 26: Effect of the interaction between digestion time and concentration on the response of the coating thickness.

The interaction between the digestion time and concentration and the effect this interaction has on the coating thickness is illustrated in Figure 26. The plot shows that at longer digestion times (red triangles), the coating thickness significantly increases with increasing concentration. At shorter digestion times (black squares), there is a moderate change in coating thickness with increasing concentration, showing a slight decrease initially followed by a slight increase. The model predicts an intersection at approximately 0.031 mol/L, at which both high and low digestion times produce the same results. The experimental results (green circles) conducted at the middle values of the inputs show coating thickness values of approximately 15 µm and 2-3 µm, which do not match the predicted values shown by the graph. The variation in results at these two points suggests that there is high variability in the coating process at these conditions, which mirrors the findings from the fit statistics for this model (Table 7).

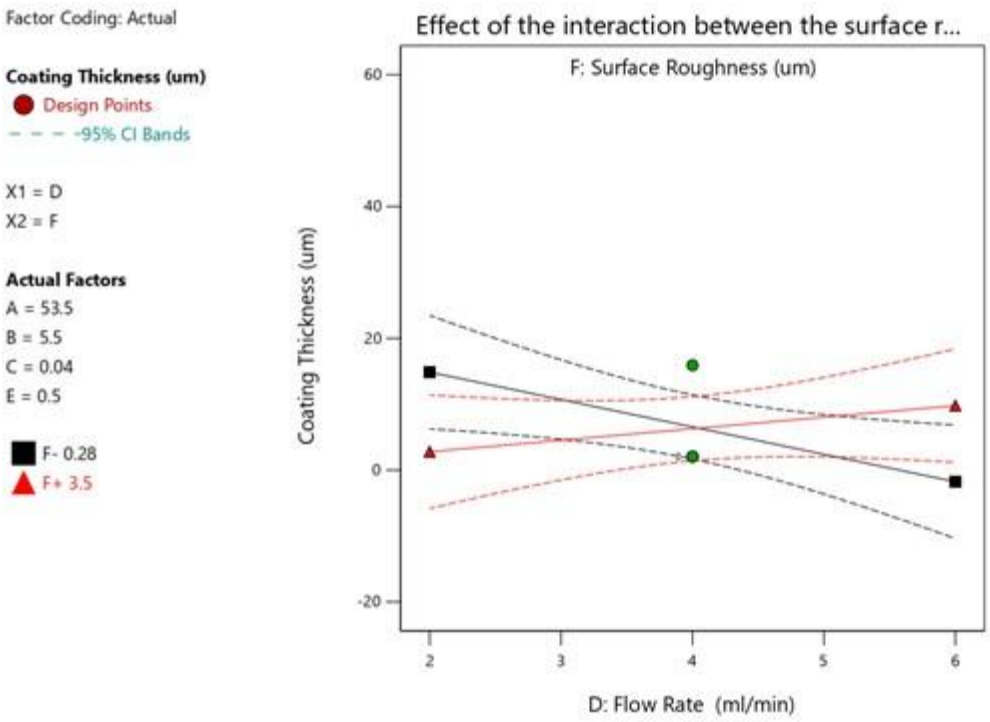

Figure 27: Effect of the interaction between the surface roughness and flow rate on the response of the coating thickness.

Figure 27 shows a complex relationship between the flow rate and the surface roughness and the effect of this interaction on the coating thickness. At low surface roughness (0.28 µm, black squares) the coating thickness decreases with increasing flow rate. At high surface roughness (3.5 µm, red triangles) the opposite is true. The lines intersect at approximately 4 mL/min, at which point either surface roughness value would produce the same results. The experimental design points (green circles) are widespread, suggesting variability in the results obtained at identical conditions. This indicates poor process reproducibility and underlines the inherent variability in the coating process.

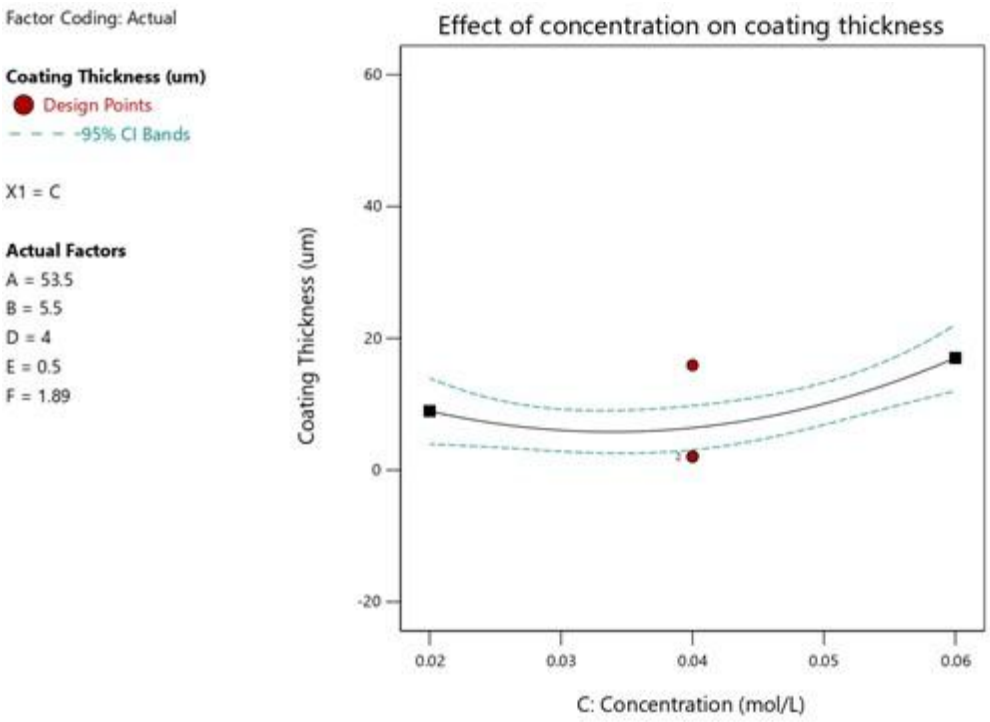

Figure 28: Effect of concentration on coating thickness.

The plot in Figure 28 shows a quadratic relationship between concentration and coating thickness. The curve predicts a slight decrease in coating thickness at low concentrations, a minimum coating thickness at approximately 0.03-0.04 mol/L, followed by an increase in the coating thickness at higher concentrations. Notably, the experimental design points (red circles) show considerable variation at identical conditions. Again, the difference in coating thickness achieved at the centre points reinforces that there is inherent process variability that cannot be predicted by the model.

Previous studies have reported that the coating thickness of HAp coatings increased linearly with the coating time [155]. Habibovic *et al.* used a two-step biomimetic method in which titanium samples were soaked twice in a concentrated SBF solution to achieve a coating thickness of 30 µm that increased with soaking time. Barrère et al. also used a similar method to produce OCP coatings of 55 µm thick that increased with immersion time. However, as the immersion method used in this study has not been reported previously, a direct comparison cannot be found in the literature to support the conclusions of this experiment [148], [175].

3.2.4 Optimisation

Following the development of models for each response, the DOE software was used to optimise the process according to the optimisation criteria detailed in Section 2.2. The optimisation produced 100 solutions to synthesise OCP coatings with the desired outputs of a high percentage of OCP, a Ca:P ratio of 1.33, and a high coating thickness, numbered according to desirability. Solutions 1-5 are presented in Table 8. Solutions 1, 2, 3 and 4 all had the same desirability of 0.933. Minimal differences in the coating properties were observed between these solutions, therefore solution 1 was selected as the optimal process. The optimal coating was then produced using these parameters 316L samples.

Table 8: The five most desirable solutions proposed by the DOE study.

Soln.	Temp. (°C)	pH	Conc. (mol/L)	Flow Rate (mL/min)	Dig. Time (hr)	Ra (µm)	%OCP	Ca:P	Coating Thickness (µm)	Desirability
1	63.083	6.986	0.060	4.706	0.941	0.294	77.425	1.330	12.662	0.933
2	62.954	6.837	0.060	5.143	1.000	0.289	77.330	1.330	12.462	0.933
3	66.171	6.972	0.060	4.081	0.944	0.280	77.304	1.330	12.761	0.933
4	63.536	6.991	0.060	4.842	0.879	0.280	77.398	1.327	12.105	0.933
5	63.419	6.748	0.060	5.416	0.998	0.280	77.185	1.330	12.039	0.932

3.3 Optimal Run

3.3.1 SEM

A representative SEM image of the coating produced from the optimal run is shown in Figure 29. The particle morphology observed was characteristic of OCP, containing plate-like particles and some needle-like particles.

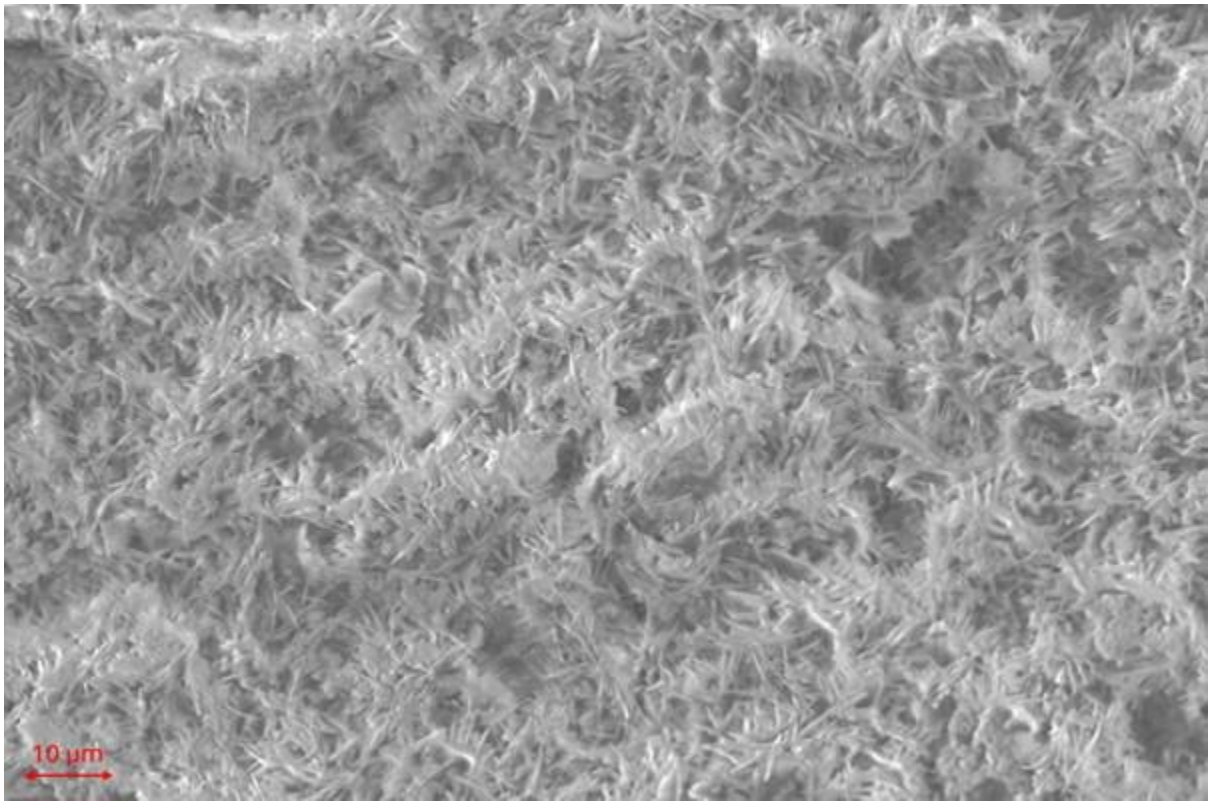

Figure 29: Representative SEM image of the OCP coatings at 500x produced using the optimal run sample (Scale bar 10 µm).

3.3.2 EDX

The results from the EDX scan of the optimal run sample are shown in Figure 30 and Table 9. The elements analysed include those found in calcium phosphates and 316L stainless steel. The presence of Na is likely caused by leftover SDPA from the coating process. The EDX results indicate a Ca:P ratio of 1.28, which is within the range for OCP and close to the optimal Ca:P ratio of 1.33 [205], [206].

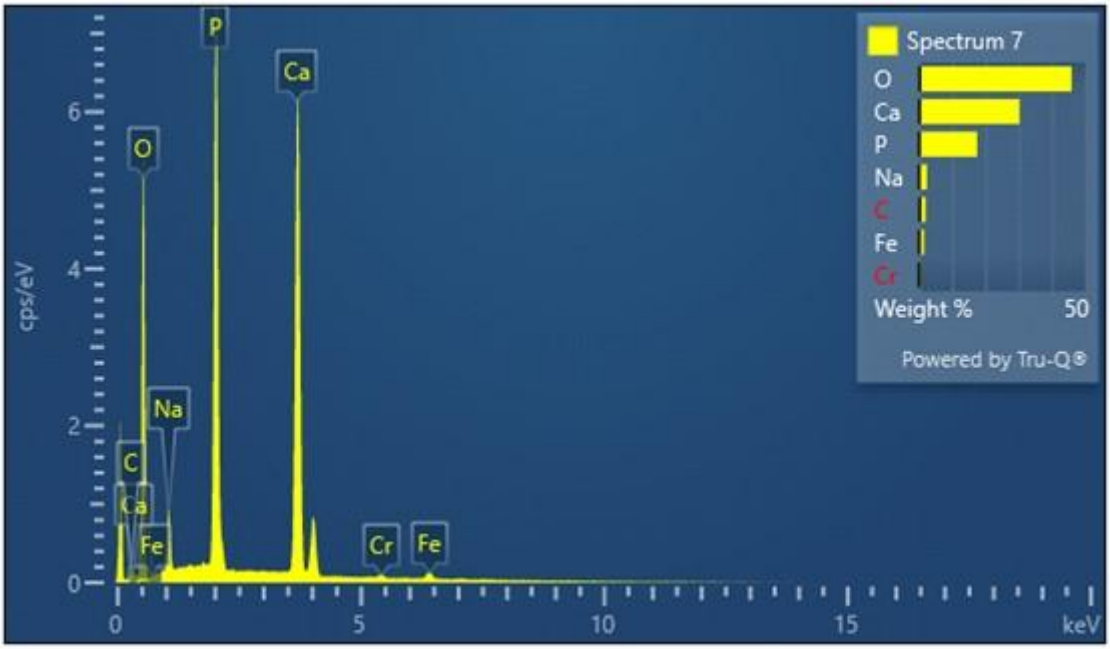

Figure 30: EDX of the optimal run samples.

Table 9: EDX results for the optimal run.

Element	Wt. %
C	15.89
O	35.74
Na	18.61
Al	8.35
Si	1.29
P	4.01
S	0.11
Ca	3.58
Mn	0.23
Fe	8.22
Ni	1.07
Cu	0.4

3.3.3 XRD

The XRD spectrum in Figure 32 below shows the diffraction pattern of the optimal run. The XRD software compared the spectrum to the powder diffraction file database to identify the

calcium phosphate phases present in the coating. The peak observed before 5° 2θ is characteristic of OCP, as is the small peak at approximately 9.4° 2θ. The peaks observed at approximately 44° 2θ are indicative of the 316L stainless steel substrate. The results generated from this spectrum by the XRD software in Table 10 show that the coating is made up entirely of OCP [207], [208], [209].

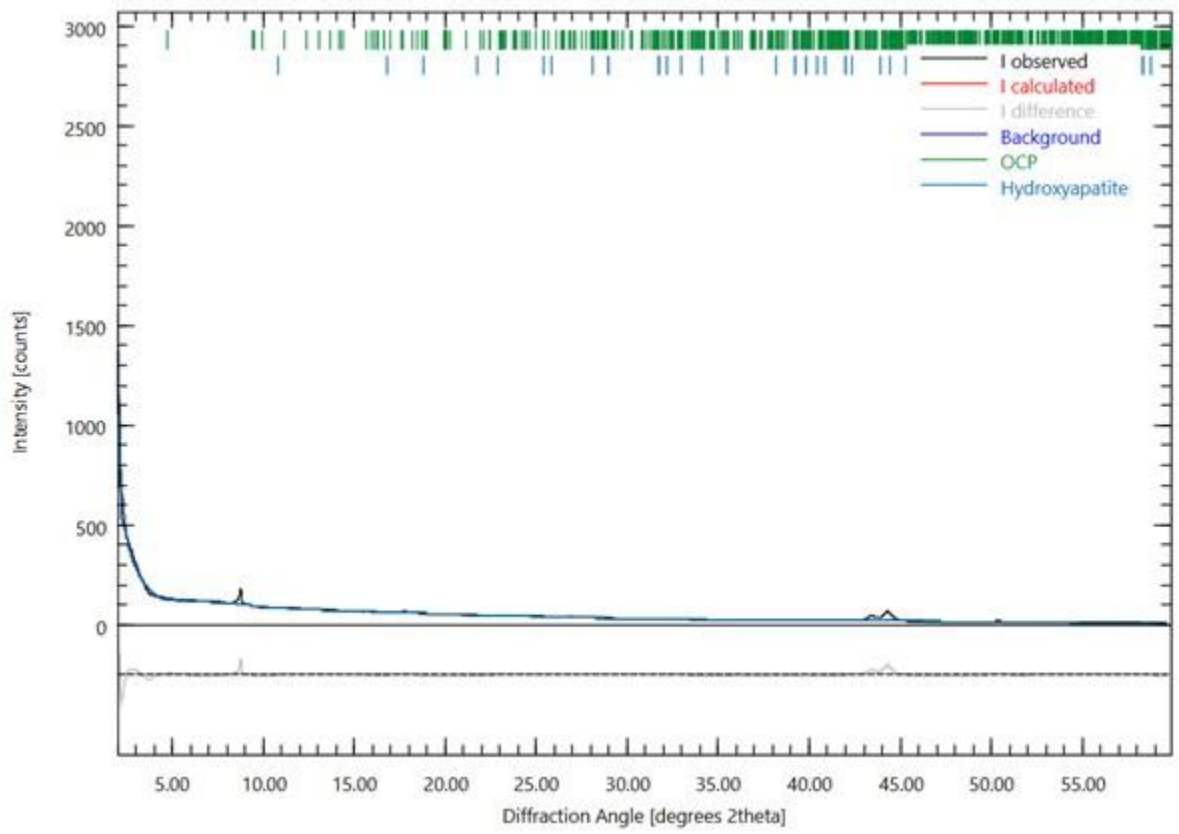

Figure 31: XRD spectrum of the optimal run coating.

Table 10: XRD results for the optimal run.

Parameter	Value
OCP	1.00
Hydroxyapatite	0.00

3.3.4 Optical Profilometry

From the optical profilometry profile in Figure 32, the coating thickness can be estimated from the Sa value. According to the optimal coating parameters suggested in solution 1 of Table 8, the optimal surface roughness suggested was 0.294 µm – this corresponds to the

untreated as-machined 316L samples, which have an average surface roughness of 0.28 µm. As this is a relatively smooth surface, using the Sa values can give a decent estimation of the coating thickness.

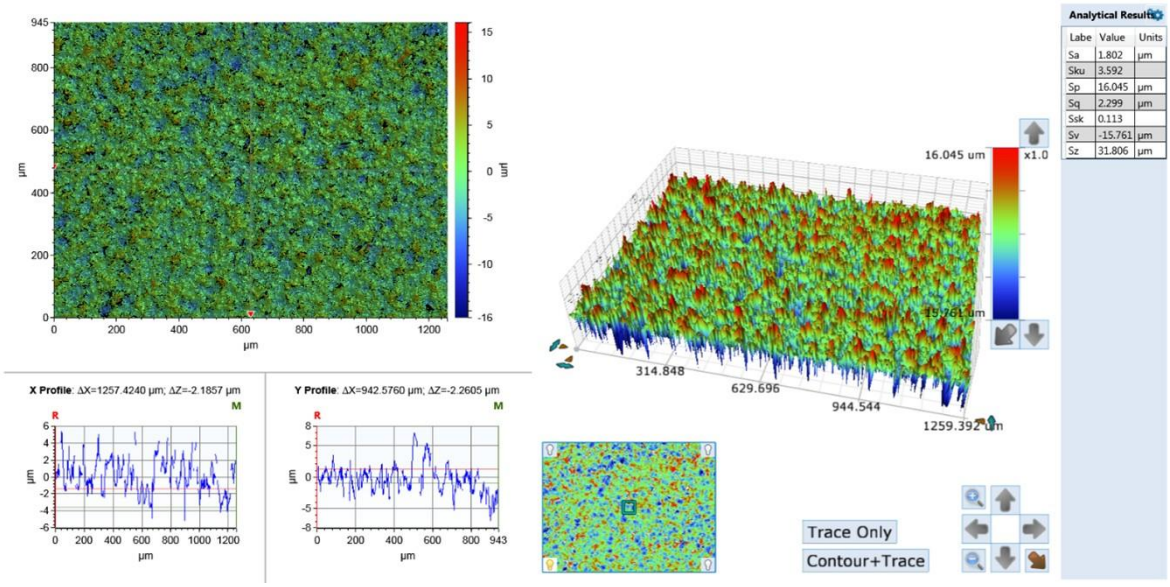

Figure 32: Optical profilometry profile of the optimal run.

The Sa value of the optimal run sample is 1.802 µm, which can be estimated as the coating thickness. The predicted coating thickness for the optimal run was 12.662 µm. As was established earlier, the DOE model is unreliable for predicting the coating thickness of the samples. The Sa value of the optimal run further confirms that the model was unreliable.

3.3.5 Model Accuracy

The parameters and predicted outcomes of the optimal run are presented in Table 11. To calculate the accuracy of the model, the experimental results were compared to the predicted results and the percentage error was calculated. It is evident from Table 12 that the model demonstrates varying levels of predictive accuracy across the different results. While the model shows good predictability for the Ca:P ratio with an error of 3.9%, the reliability decreases significantly for the other results. The model underestimates the predicted percentage of OCP in the coating, giving an error of 22.58%. Most notably, the model significantly overestimates the coating thickness, resulting in an error of 602.66%. The deviations in the predictability suggest that even with quadratic terms included, the model may fail to account for complex interactions or higher-order relationships between the inputs

involved in the coating process. This is possible if slight changes in the inputs drastically affect the responses, resulting in a relationship that cannot be accurately captured by this model.

The implementation of more rigorous control over the inputs may result in a more accurate model. For future studies, a lower variation of the inputs may produce more accurate results. This would be crucial to consider when scaling up the process on an industrial level. Also, the environmental factors such as room temperature and humidity may affect the coating properties that were not accounted for or controlled in this model. For the coating thickness, a higher-order model may result in a lower percentage error as it can account for more complex interactions. However, it is also possible that this method of coating orthopaedic implants does not offer the required control over the thickness of the coating.

Table 11: Inputs and predicted results for the optimal run.

Inputs						**Predicted Results**			
Temp. (°C)	**pH**	**Conc. (mol/L)**	**Flow Rate (mL/min)**	**Dig. (hr)**	**Ra (µm)**	**%OCP**	**Ca:P**	**Coating Thickness (µm)**	**Desirability**
63.083	6.986	0.060	4.706	0.941	0.294	77.425	1.330	12.662	0.933

Table 12: Predicted VS actual results for the optimal run and the percentage error.

	Predicted Results	**Experimental Results**	**% Error**
OCP (%)	77.425	100	22.58
Ca:P Ratio	1.33	1.28	3.9
Coating Thickness (µm)	12.662	1.802	602.66

3.4 Degradation Study

3.4.1 Adhesion Testing

Following completion of the DOE optimal run, the degradation rate of the coatings on WE43 Mg-alloy samples was assessed. The adhesion strength of the coating to the substrate was first assessed using test method A in ASTM D3359-22 [188], as described in Section 2.3.4. The results of the adhesion test for three coated WE43 Mg-alloy samples are shown in Figure 33. The adhesion strength of the coating is an important consideration as a well-adhered coating is more likely to remain intact before and after being placed in the fracture site.

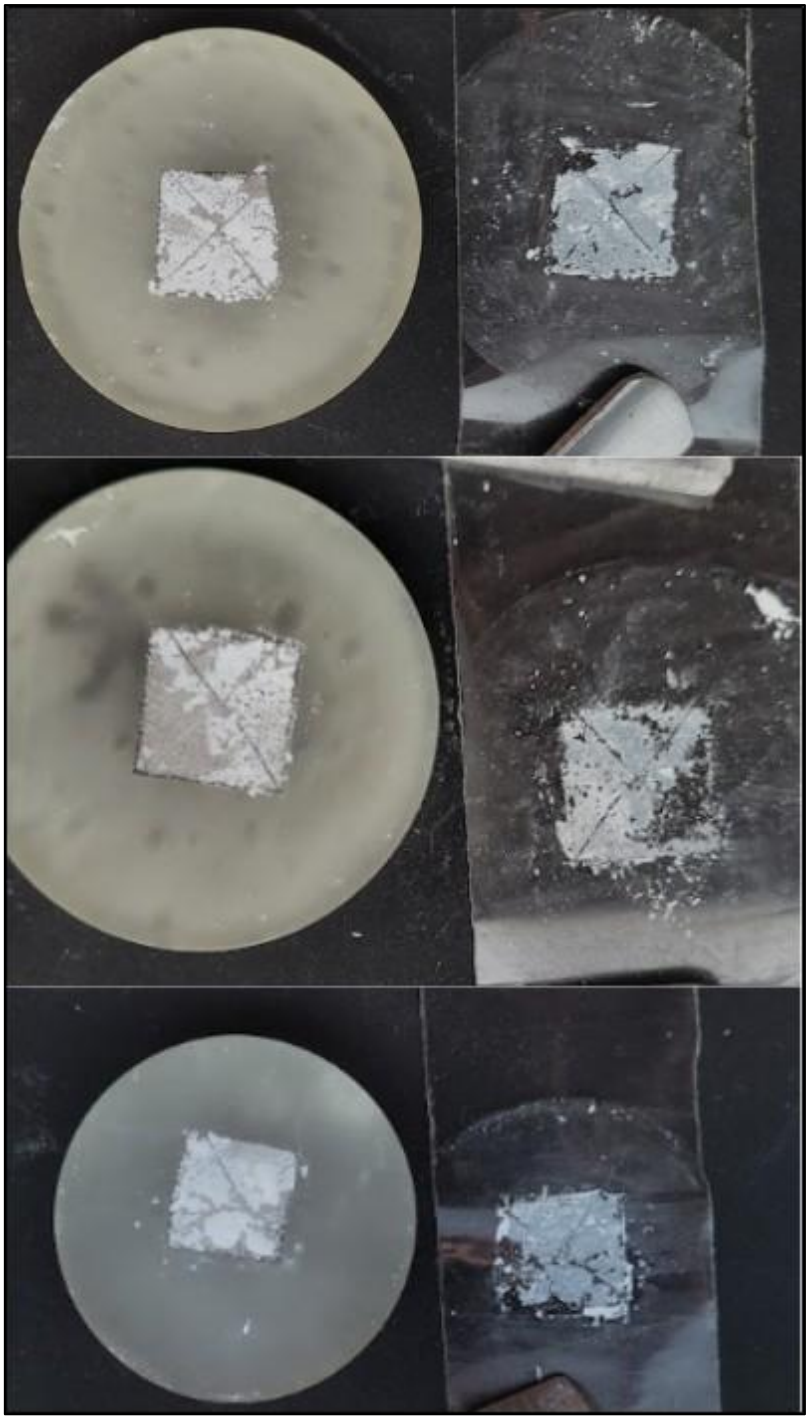

Figure 33: Adhesion test results for OCP coated WE43 Mg-alloy samples, tested according to ASTM D3359-22 Test Method A.

Comparing the results in Figure 33to the classification metric in Figure 14, the coatings were classified as 4A, with trace peeling or removal. It is evident that the top layer of the coating is removed by the pressure sensitive tape, however the base layer of the coating is still in-tact and adhered to the magnesium surface. The tape failed to fully separate the coating from the substrate, therefore indicating that the coating is well adhered to the magnesium sample. This method of determining the adhesion strength of calcium phosphate coatings on metallic

substrates has been used in numerous studies [210], [211], [212]. However, there is considerable variation in the equipment used and the size and shape of the X cut in the coating across the literature. Also, as the results are observed by eye, the classification of the coating adhesion is not definitive and can vary from person to person. A more accurate adhesion test method that should be used in future studies is the scratch test method (ASTM C1624-22) or the shear testing of the adhesion of the coating (ASTM F1044-05) [213], [214], [215].

3.4.2 Mass Loss

The mass loss of the coated and uncoated WE43 samples during degradation was determined by weighing each sample before and after degradation at each time point. The mean results are presented in Figure 34 below, with standard deviation error bars. The rate of degradation over time (mm/year) was calculated using the equation described in Section 2.4 and the results were plotted against the time points of the degradation study in Figure 35.

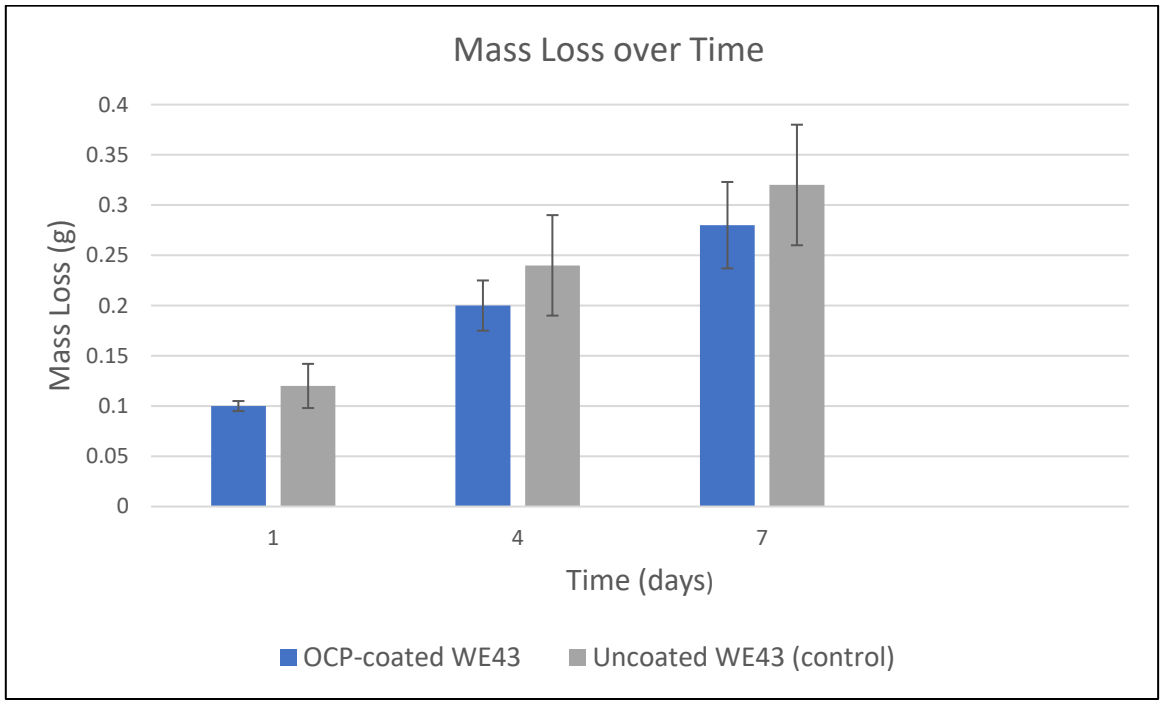

Figure 34: Mass loss over time of coated and uncoated WE43 samples during degradation.

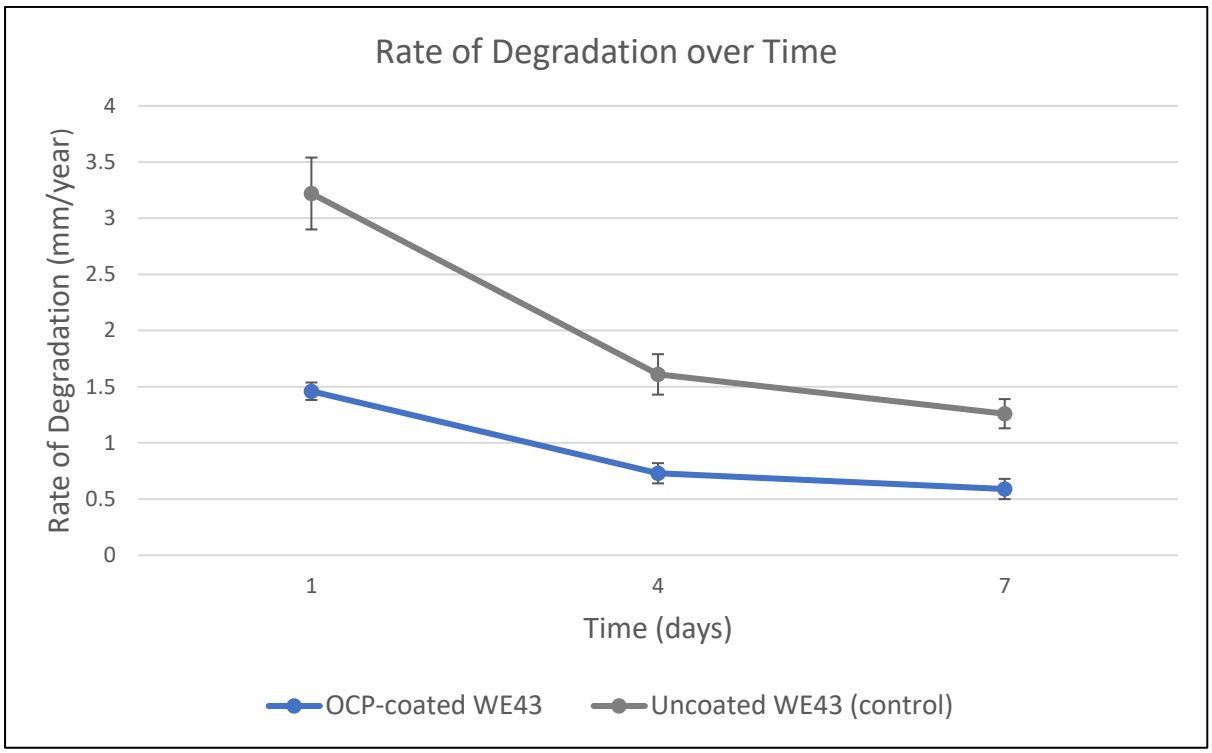

Figure 35: Rate of degradation over time for coated and uncoated WE43 samples.

It can be seen from Figure *34* and Figure 35 that the coating reduces the degradation of the magnesium samples in simulated physiological conditions. These results correspond to those in the literature, confirming that OCP effectively protects against magnesium degradation [144], [156], [216], [217]. The protective effect of the OCP coating is most notable at the beginning of the degradation, and gradually reduces over time. The OCP coating acts as a physical barrier between the magnesium surface and the aqueous environment, slowing down the initial degradation reaction. As the immersion continues, the protective effect of the OCP coating reduces. This can be a result of the physical breakdown of the OCP coating over time. Once the physical barrier of the coating is compromised, the surface of the magnesium comes into direct contact with the aqueous environment, and corrosion occurs. Also, it has been established that OCP converts to HAp in physiological conditions, which is less effective at controlling the rate of magnesium degradation [8], [151], [217], [218], [219], [220].

In this thesis, the degradation study was run for seven days as a proof-of-concept that OCP can reduce the degradation rate of magnesium in simulated physiological conditions. However, in clinical applications, fractures that require surgical implants can take anywhere from twelve weeks to six months to heal fully, and this process can be impacted by a multitude of factors relating to the patient and the individual healing process [221], [222], [223]. For this reason, further degradation studies with a longer immersion period are required to determine if the OCP coating can control the degradation of a magnesium implant and provide sustained bioactive function for the full duration of the fracture healing process.

3.4.3 pH

The pH of the Hank's balanced salt solution was measured before the degradation and at each time point for each sample. The results in Figure 36 represent the mean value for three measurements per sample.

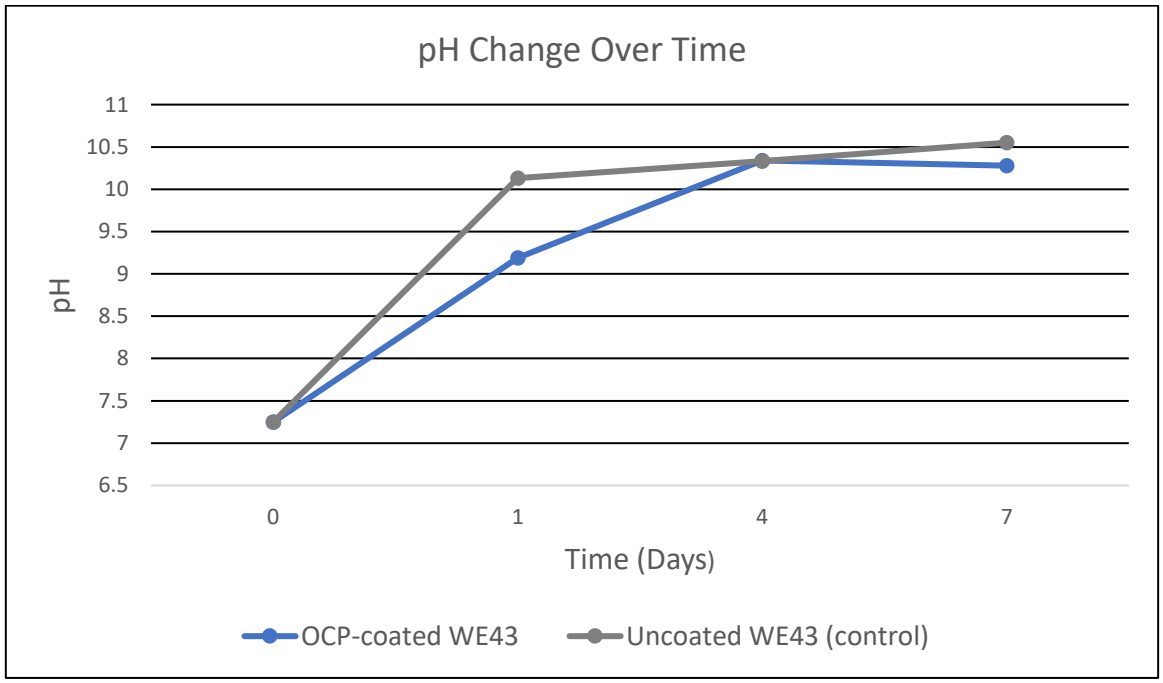

Figure 36: pH change over time for coated and uncoated WE43 samples.

As it is shown in Figure 36 above, both the OCP-coated WE43 and uncoated WE43 samples show an increase in pH of the Hank's balanced salt solution from a neutral pH to alkaline

conditions. This is characteristic of magnesium degradation in physiological solutions. The reaction that takes place in an aqueous solution is as follows:

$$Anodic\ reaction: Mg \rightarrow Mg^{2+} + 2e^{-}$$
$$Cathodic\ reaction: 2H_2O + 2e^{-} \rightarrow 2OH^{-} + H_2$$
$$Product\ formation: Mg^{2+} + 2OH^{-} \rightarrow Mg(OH)_2$$
$$Overall\ reaction: Mg + 2H_2O \leftrightarrow Mg^{2+} + 2OH^{-} + H_2$$

The contact between the surface of the magnesium alloy and an electrolyte-containing aqueous medium, such as Hank's balanced salt solution, leads to high initial corrosion rates. This results in the release of hydrogen gas and the alkalinisation of the surrounding environment. The formed $Mg(OH)_2$ acts as a protective oxide layer on the surface of the magnesium sample that precipitates easily due to its low solubility in water. The $Mg(OH)_2$ layer reduces the rate of degradation of the magnesium to a certain degree. However, in the presence of chloride ions, as in HBSS and a physiological environment, additional reactions occur that lead to the breakdown of this hydroxide layer:

$$Mg(OH)_2 + 2Cl^{-} \rightarrow MgCl_2 + 2OH^{-}$$

The release of OH^- ions in this reaction further contribute to the increase in pH of the immersion medium. As the $Mg(OH)_2$ layer is degraded, the surface of the magnesium layer is exposed once more and the reactions above occur again. This accounts for the further increase in the pH values over time.

The plateau in the pH values at approximately pH 10 observed in Figure 36 can be caused by several mechanisms. A chemical equilibrium of $Mg(OH)_2$ occurs when the solution approaches pH 10 as the immersion solution hits the saturation limit of $Mg(OH)_2$. With the stabilisation of the amount of the protective oxide layer, the degradation and therefore the pH is also gradually stabilised. This corresponds to the results observed in Figure 35 and Figure 36. While the corrosion of the magnesium sample will slowly continue, the pH will remain at the same approximate value as the rate of OH^- production becomes roughly equal to the rate

of OH^- consumption in the formation of $Mg(OH)_2$. The stabilisation of the pH in the corrosion of magnesium represents a natural limiting factor in the alkalinisation process of Mg degradation and is well-documented in the literature [116], [117], [118], [124], [172], [224], [225]

Figure 36 shows that there was a slower and more gradual increase in pH values over time for the OCP-coated WE43 samples compared to the uncoated WE43 samples. As the increase in pH corresponds to the degradation of magnesium, it also confirms the results shown in Figure 35 that the presence of the OCP coating reduces the initial rate of magnesium degradation. As well as acting as a physical barrier between the magnesium surface and the surrounding environment, OCP ($Ca_8H_2(PO_4)_6{\cdot}5H_2O$) can act as a buffering agent and neutralise OH^- ions:

$$PO_{43}{}^{-} + OH^{-} \leftrightarrow HPO_{42}{}^{-} + H_2O$$

This buffering effect is reflected in the slower increase in pH for the coated WE43 samples in the first four days of sample immersion. After this time point, the pH of the immersion solution of the OCP-coated samples mirrors that of the uncoated samples due to the physical breakdown of the OCP coating and the conversion to hydroxyapatite overtime [217], [218], [219], [220]

3.4.4 SEM

The SEM images of the OCP-coated and uncoated WE43 samples at each degradation time point as well as the OCP-coated samples before degradation are shown Figure 37-44.

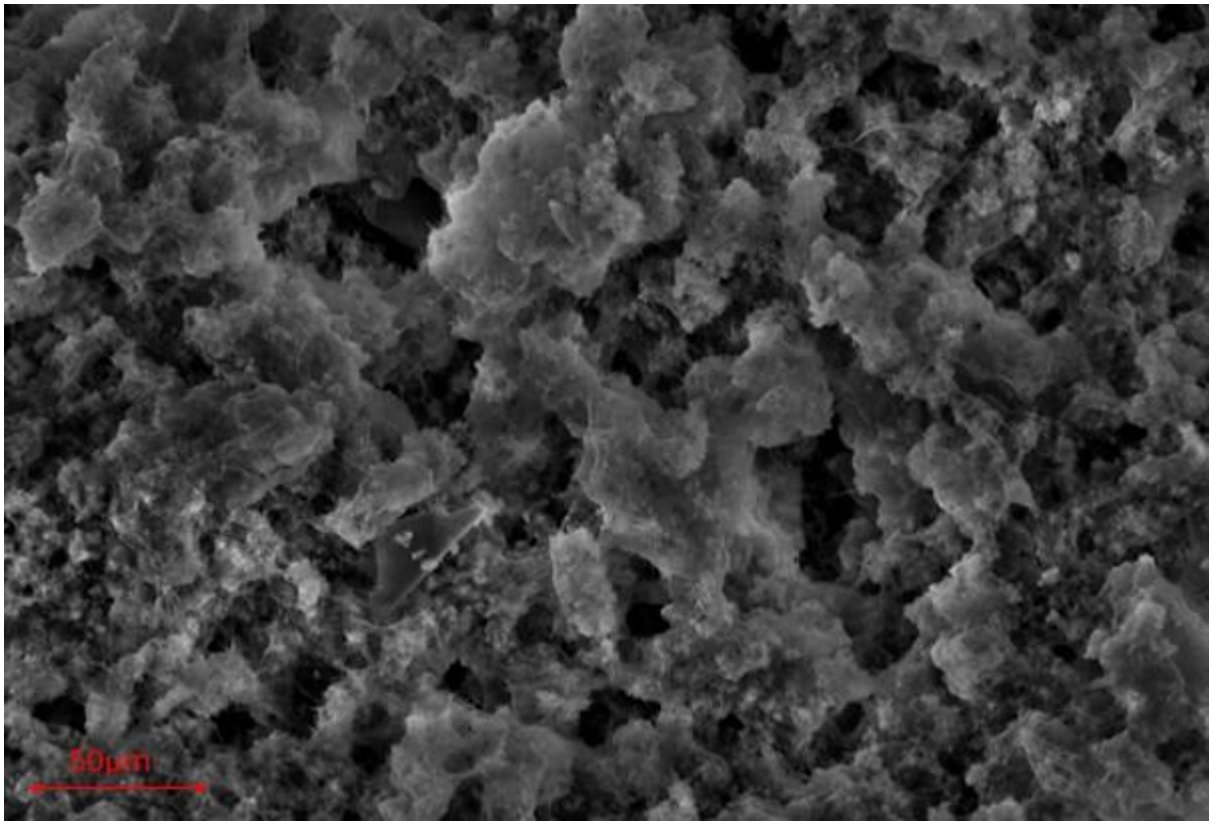

Figure 37: SEM image at 400x of OCP-coated WE43 before degradation (scale bar 50 µm).

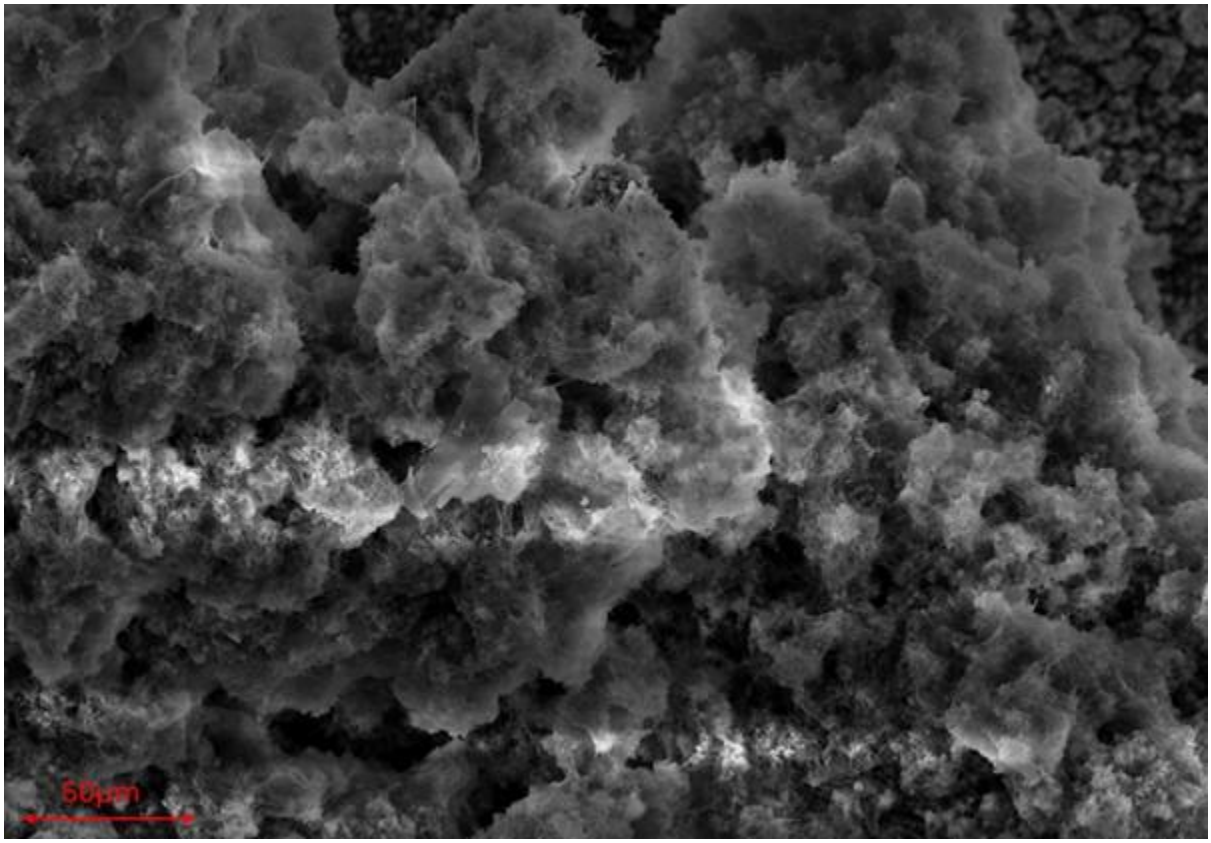

Figure 38: SEM image at 400x of OCP-coated WE43 samples after 1 day of immersion in HBSS (scale bar 50 µm).

The SEM image of the as coated OCP-coated WE43 sample prior to degradation in Figure 37 show a combination of plate and needle-like crystals, as is typical for OCP. Figure 38 shows the SEM image of OCP-coated WE43 samples after one day of immersion in HBSS. Plate and needle-like crystals remain visible, however, some amorphous particles have formed as aggregates on the surface of the surface of the samples.

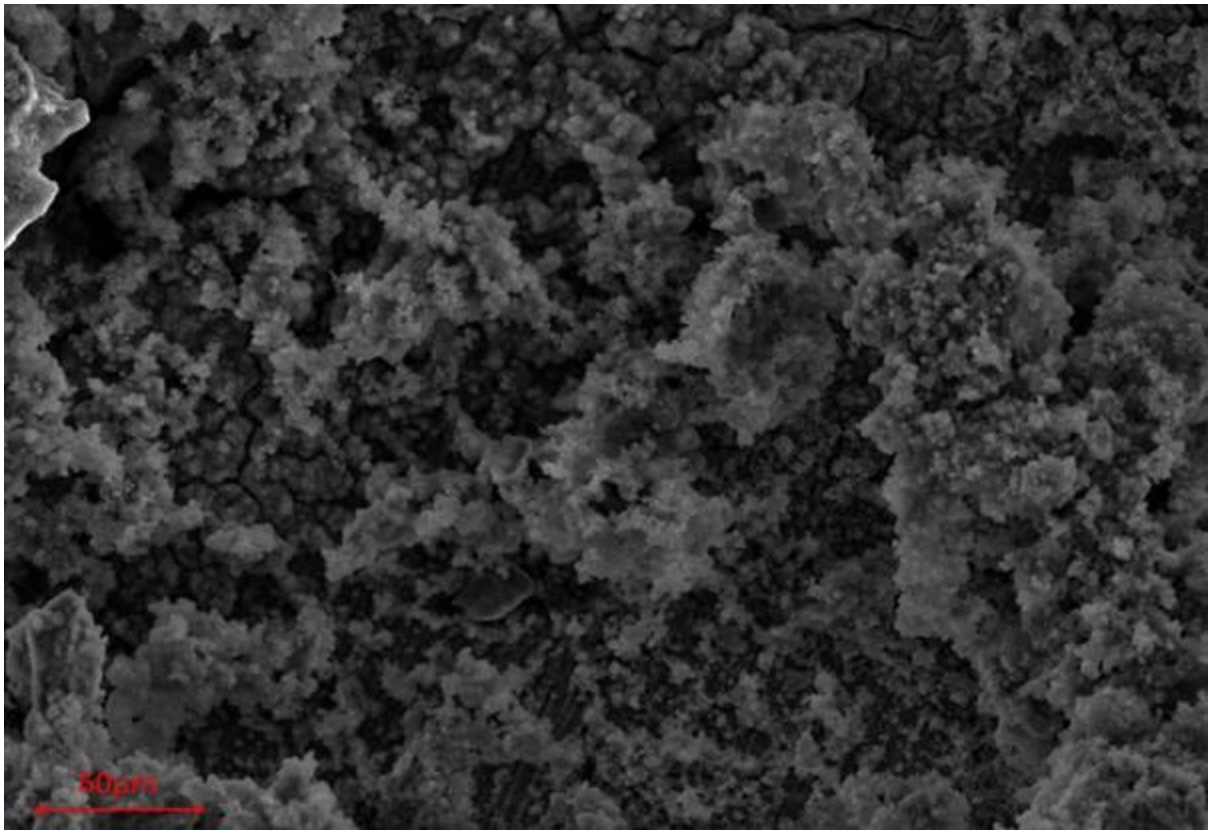

Figure 39: SEM image at 400x of OCP-coated WE43 after 4 days of immersion in HBSS (scale bar 50 µm).

Figure 39 shows an SEM image of OCP-coated WE43 after four days of immersion in HBSS. The morphology of the coating has slightly changed compared to the images for the Day 0 and Day 1 time points. The coating now consists of aggregates of spherical and amorphous particles as well as some plate crystals. There are more gaps in the coating at this time point due to the breakdown of the OCP coating in the immersion medium over time.

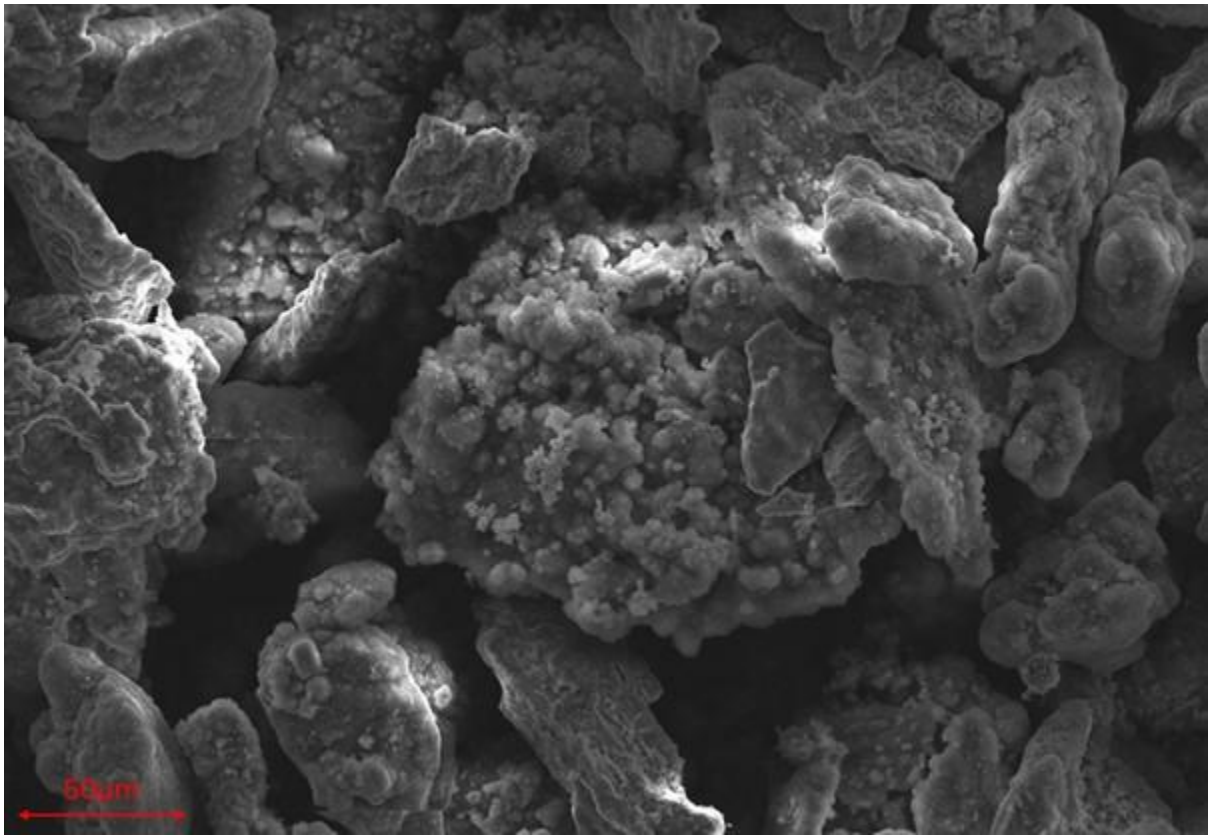

Figure 40: SEM image at 400x of OCP-coated WE43 samples after 7 days of immersion in HBSS (scale bar 50 µm).

Figure 40 shows the SEM image of OCP-coated WE43 after seven days of immersion in HBSS. The coating in this image is significantly different to the previous images. The coating at this time point consists of large irregular-shaped particles as well as some small spherical particles and some plate crystals. The large particles are likely magnesium corrosion products that have precipitated on the WE43 surface, as similar SEM results have been shown in other studies. The smaller particles and plate crystals are hydroxyapatite formation on the WE43 surface, which have a similar appearance to that seen in other studies. The presence of hydroxyapatite was confirmed using XRD spectrometry [226], [227].

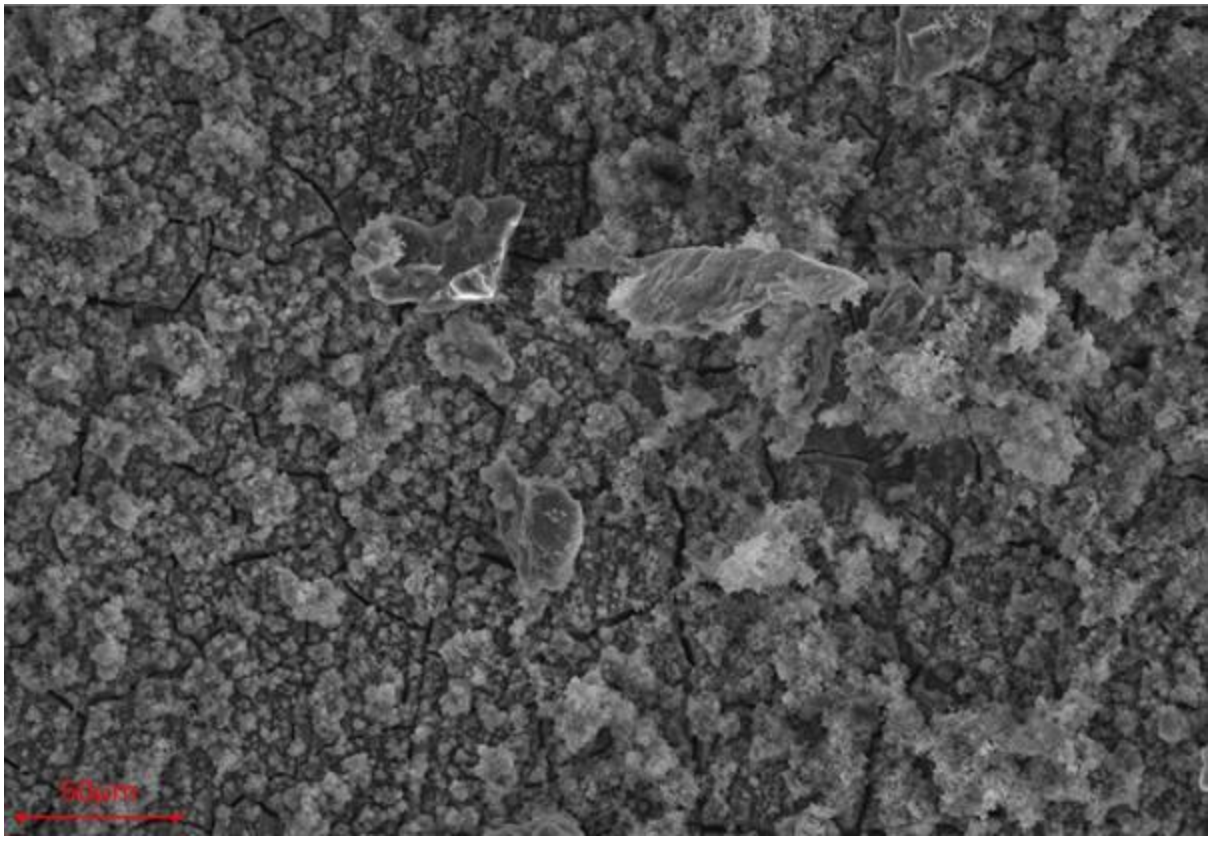

Figure 41: SEM image at 400x of uncoated WE43 samples after 1 day of immersion in HBSS (scale bar 50 µm).

The image in Figure 41 shows the SEM image of the surface of an uncoated WE43 samples after one day of immersion in HBSS. The image shows amorphous particles, and some plate crystals formed on the surface of the WE43 sample. The particles observed are likely WE43 corrosion products formed in HBSS such as $Mg(OH)_2$, MgCl, $MgCO_3$, $Mg_3(PO_4)_2$, or calcium phosphate phases that precipitated out of the immersion solution.

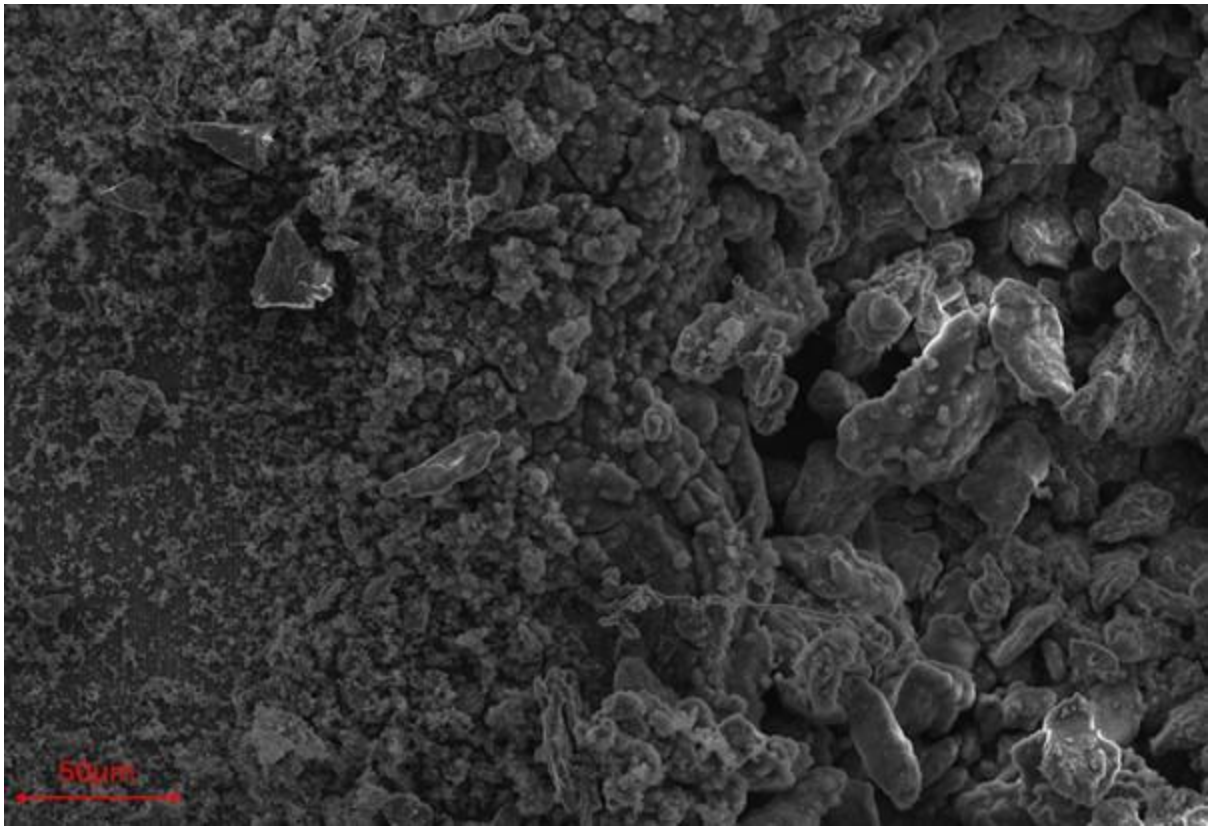

Figure 42: SEM image at 400x of uncoated WE43 samples after 4 days of immersion in HBSS (scale bar 50 µm).

Figure 42 shows an SEM image of uncoated WE43 after four days of immersion in HBSS. The image shows pitting corrosion in the right half of the image with large, irregular-shaped corrosion particles. The left side of the image shows small amorphous particles.

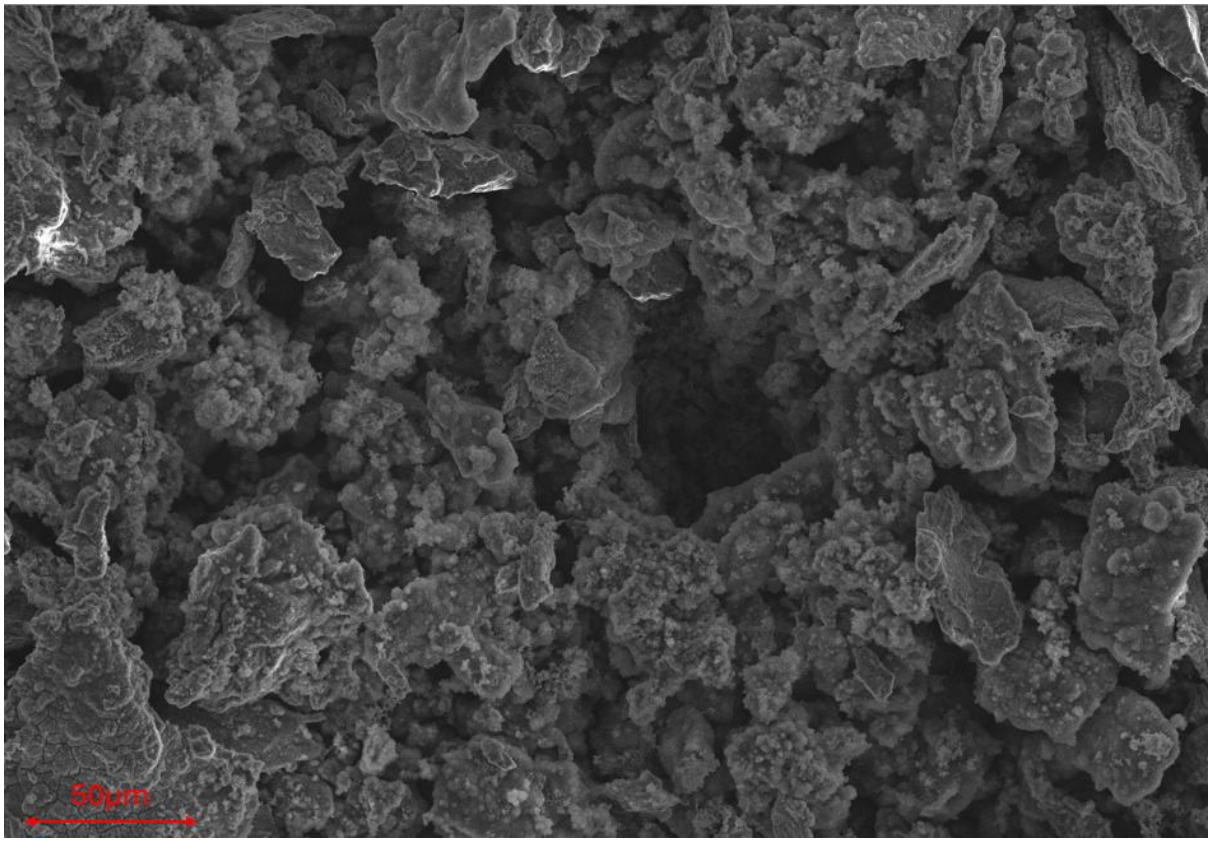

Figure 43: SEM image at 400x of uncoated WE43 samples after 7 days of immersion in HBSS (scale bar 50 µm).

The image in Figure 43 shows the uncoated WE43 sample after 7 days of immersion in HBSS. The image shows large corrosion particles and significant pitting corrosion.

3.4.5 XRD

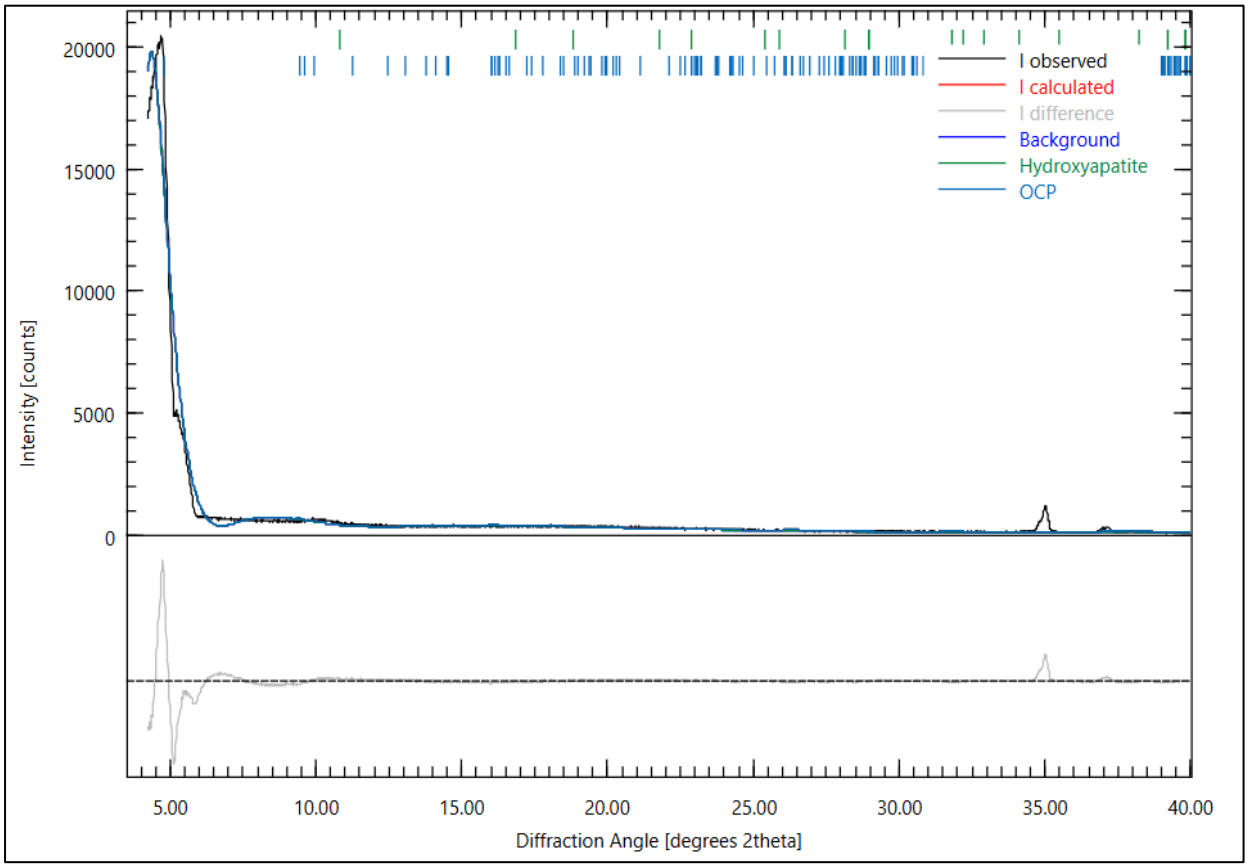

Figure 44: XRD spectrum of OCP-coated WE43 prior to immersion in HBSS.

Table 13: XRD results of OCP-coated WE43 prior to immersion in HBSS.

Parameter	Value
OCP	0.1
Hydroxyapatite	0.0

Figure 44 and Table 13 depict the XRD results of OCP-coated WE43 before being immersed in HBSS, showing that the OCP coating produced using the optimal method developed in this project consists of 100% OCP.

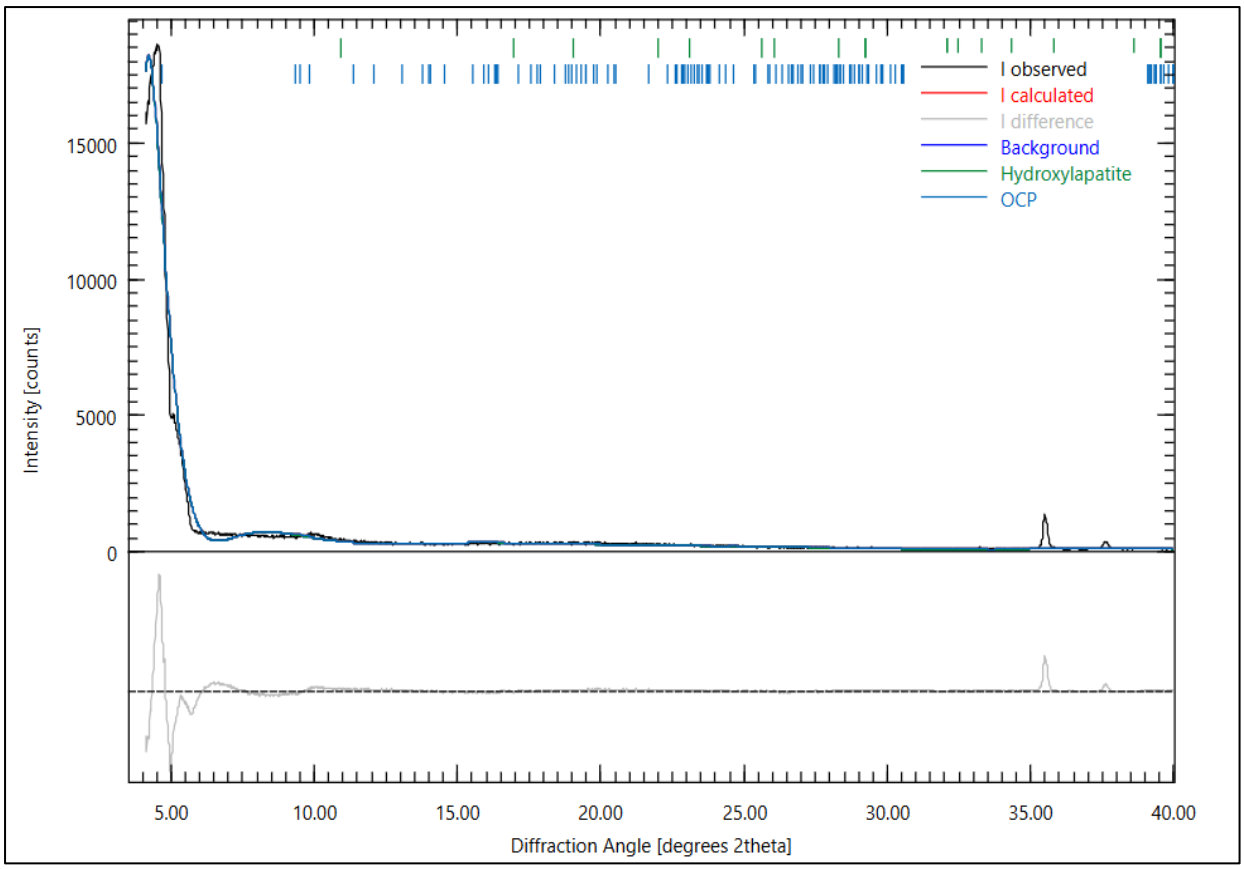

Figure 45: XRD spectrum of OCP-coated WE43 after 1 day of immersion in HBSS.

Table 14: XRD results of OCP-coated WE43 after 1 day of immersion in HBSS.

Parameter	Value
OCP	0.99
Hydroxyapatite	0.01

Figure 45 and Table 14 show the XRD results of the OCP-coated WE43 sample after one day of immersion in HBSS. The results show that the coating consists of 99% octacalcium phosphate and 1% hydroxyapatite, as the OCP coating has begun to degrade and convert into HAp.

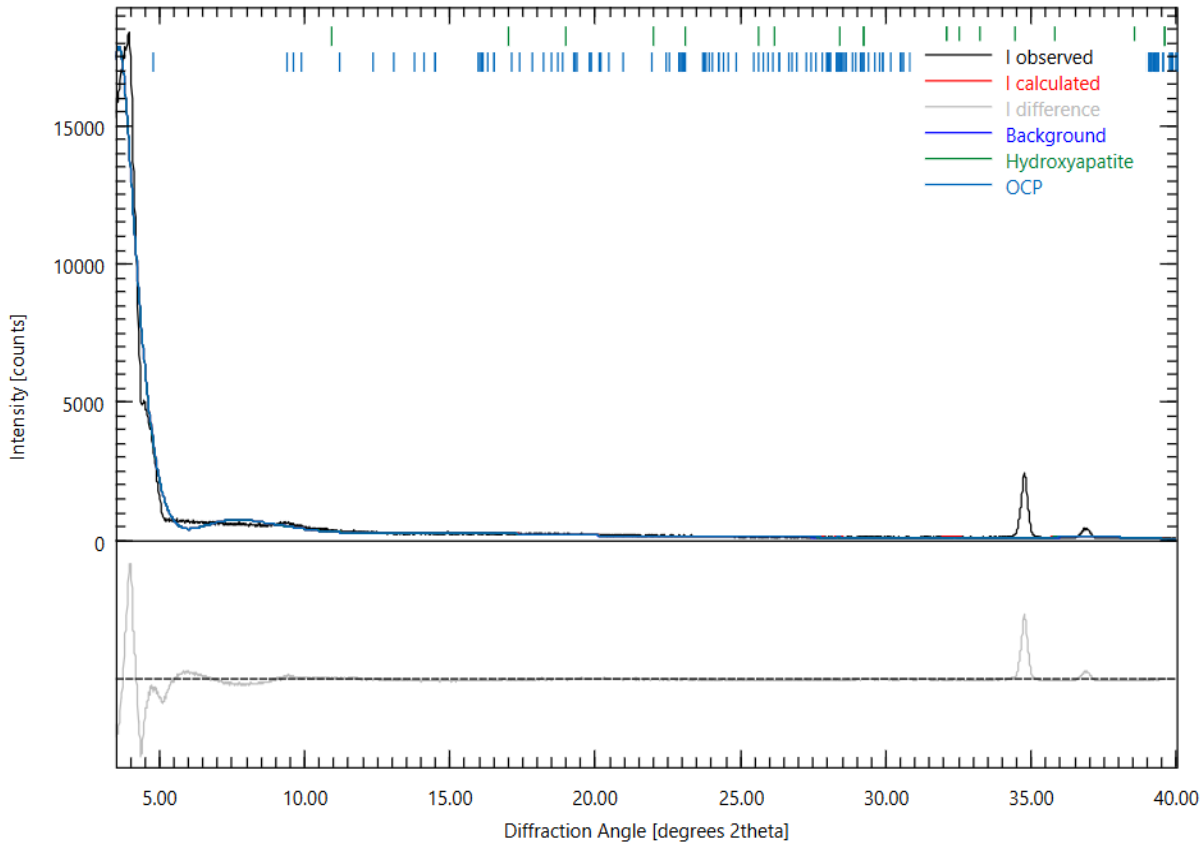

Figure 46: XRD spectrum of OCP-coated WE43 after 4 days of immersion in HBSS.

Table 15: XRD results of OCP-coated WE43 after 4 days of immersion in HBSS.

Parameter	Value
OCP	0.4
Hydroxyapatite	0.6

Figure 46 and Table 15 show the XRD results for OCP-coated WE43 after four days of immersion in HBSS. At this time point, the coating consists of 40% OCP and 60% HAp, indicating that the OCP coating is more than half-way through its conversion to HAp. This corresponds to the pH and mass loss results, as at the four-day time point significant degradation has taken place. This is because HAp is not as effective at protecting against magnesium degradation.

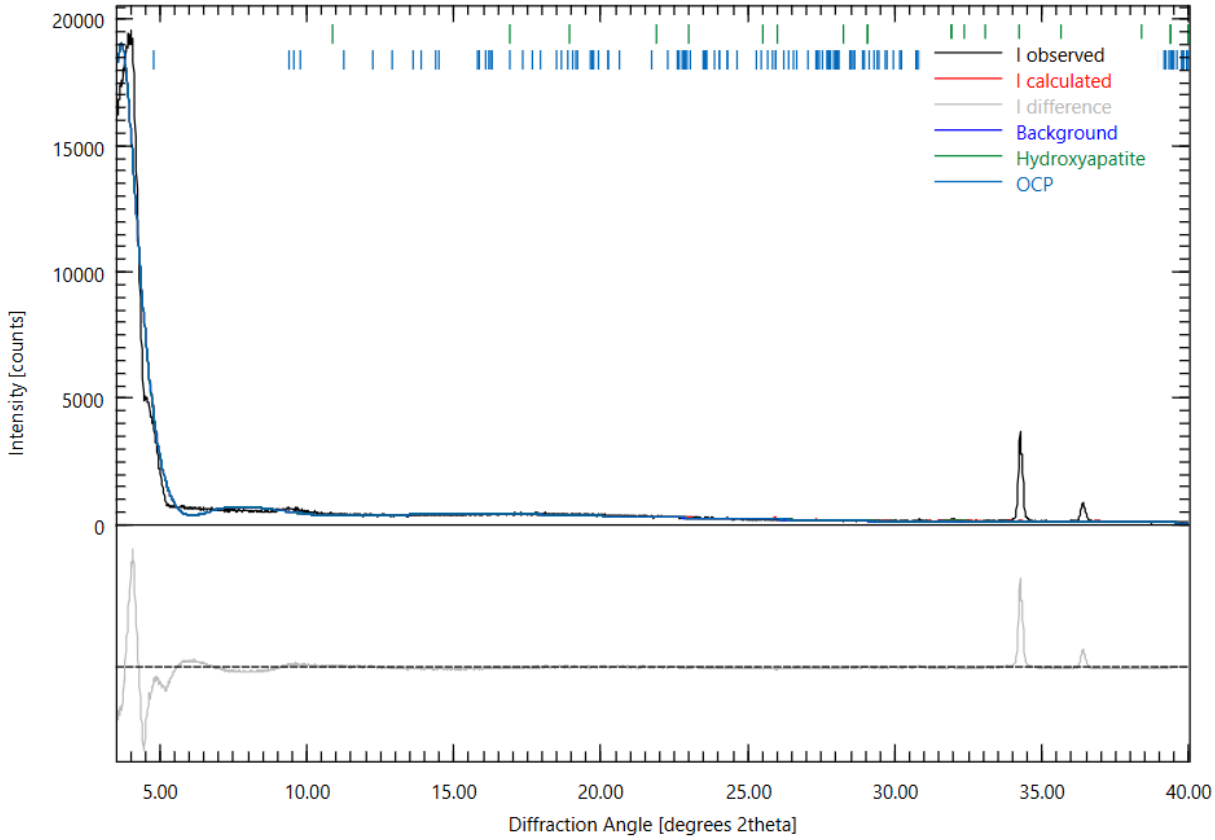

Figure 47: XRD spectrum of OCP-coated WE43 after 7 days of immersion in HBSS.

Table 16: XRD results of OCP-coated WE43 after 7 days of immersion in HBSS.

Parameter	Value
OCP	0.3
Hydroxyapatite	0.7

Figure 47 and Table 16 show the XRD results for OCP-coated WE43 after seven days of immersion in HBSS. The amount of OCP in the coating has decreased by 10%, from 40% to 30% between the four-day and seven-day time points. This slower conversion rate corresponds to the plateau of pH values and Mg mass loss at these time points as the degradation reaction approaches equilibrium and the immersion solution becomes supersaturated with respect to OCP.

3.5 Summary

In this study, OCP was successfully synthesised using the dropwise addition of a calcium acetate solution to a stirred sodium phosphate solution. The presence of OCP was confirmed using ATR-FTIR and SEM. Following the success of the OCP synthesis, 316L samples were coated by immersion in the OCP reaction vessel. A DOE approach was employed to investigate the reaction parameters that result in an optimal coating with high coating thickness, high OCP phase purity, and a Ca/P ratio of 1.33. Using the data obtained from 51 runs, the DOE software determined the optimal parameters to be a temperature of 63.083 °C, a pH of 6.986, a concentration of 0.06 mol/L, a flow rate of 4.706, a digestion time of 0.941 hours, and a surface roughness of 0.294 µm. These optimal conditions were replicated as accurately as possible on 316L samples which were analysed using XRD, SEM, EDX, and optical profilometry. It was found that while the DOE model was able to accurately predict the resulting Ca/P ratio, it slightly underestimated the percentage of OCP in the resulting coating and greatly overestimated the coating thickness. The optimal coating was applied to magnesium alloy WE43 samples in order to investigate the ability of the OCP coating to reduce the degradation of magnesium *in vitro*. It was determined that the coating noticeably reduced the degradation of magnesium while converting to hydroxyapatite after seven days of immersion in HBSS.

4 Conclusions and Further Research

The overall aim of this project was to produce an OCP-based coating that effectively controlled the degradation of magnesium implants using an immersion technique proposed by PBC Biomed Ltd based on the method described by LeGeros [181]. In this study, a DOE approach was employed to investigate the optimal parameters of the coating method to produce a coating with a high percentage of OCP, a Ca:P ratio of 1.33 and high coating thickness. While the DOE model failed to accurately predict the coating thickness, the optimal parameters deduced by the DOE software resulted in a coating consisting of 100% OCP with a Ca:P ratio of close to the desired 1.33. The coating was also found to have good adhesion to the substrate. To investigate the ability of the OCP coating to control the degradation of magnesium, samples of the WE43 Mg alloy were coated with the optimal OCP coating and were subject to immersion in HBSS. The samples were analysed at one, four, and seven days against a control group. It was determined from the mass loss of magnesium over time that the OCP coating successfully reduced the rate of degradation of the WE43 Mg alloy samples in the first four days before plateauing as the degradation reaction approached equilibrium. The SEM analysis showed the conversion of plate and needle-like crystals consistent with the OCP coating to the more spherical morphology of HaP, which was confirmed by the XRD results. The SEM results also showed the corrosion of the WE43 samples.

While the coatings developed in this study successfully reduced the degradation rate of magnesium, further research on this topic is necessary in order to develop this method for use on commercially available orthopaedic implants. In particular, the coating thickness model developed in the DOE poorly predicted the thickness of the coating produced for the optimal run. A more detailed DOE study should be performed to accurately control the thickness of the OCP coating produced by this method. As it is evident that different coating methods produce different results, it may be beneficial to conduct a detailed comparative study of different coating methods to determine what exactly impacts the thickness of the resulting calcium phosphate coating [168]. It is also possible that the DOE would be able to produce more accurate results when using magnesium as a substrate instead of 316L. However, as 316L has been extensively researched as a suitable orthopaedic implant material

and is relatively inert, it is unlikely that using 316L for the DOE had a significant impact on the results [108], [178]. A direct comparison between the two materials could be made in the future to determine this. As there is no specific value for the optimal thickness of an OCP coating on a metallic orthopaedic implant presented in the literature, it would be beneficial to conduct studies that examine the coating thickness value that produces the most favourable results. OCP coatings with a variety of different thicknesses have been synthesised and reported. It has been suggested that coatings of a higher thickness could potentially delaminate due to stress accumulation within the coating, and thinner coatings may be insufficient to allow sustained bioactivity and bone resorption [228], [229]

Also, a more accurate method of determining the adhesion strength of the coating should be implemented to better understand the properties of the coating. The ASTM F1044 method can be used to accurately test the shear strength of a calcium phosphate coating bonded to a metallic substrate. In this thesis, test method A in ASTM D3359-22 was used to determine the adhesion strength of the OCP coating on magnesium samples. Other methods such as scratch tests, hardness tests, and pin-on-disc wear tests could also provide useful quantitative results for the coating adhesion. The samples used in this testing were standard disc shapes. Hardness testing could also provide valuable information about the coating thickness across different regions of the coating surface. Orthopaedic implants can have more complex and irregular shapes depending on their specific clinical applications and fracture sites. Therefore, the coating method developed in this project should be tested with orthopaedic implants of an irregular shape.

Here degradation was assessed using a simplified static degradation study. A more detailed study of the degradation properties of OCP-coated Mg samples over a longer period of time and using dynamic flow immersion conditions to more accurately represent the physiological environment would provide greater insight into the potential degradation behaviour of OCP-coated implants *in vivo*. Finally, biocompatibility and cell studies can be implemented to analyse the biological performance of the coated implants.

Overall, this project has led to the successful development of an OCP coating that protects against magnesium degradation. The study led to new knowledge relating to the influence of process parameters on the properties of OCP coting deposited using this immersion coating technique. The results presented in this thesis provide a promising approach for the fabrication of OCP-coated magnesium orthopaedic implants.

References

[1] J. A. Kanis *et al.*, 'SCOPE 2021: A New Scorecard for Osteoporosis in Europe', Nyon, Switzerland, 2022. [Online]. Available: https://www.osteoporosis.foundation/scope-2021

[2] P. Hickey *et al.*, 'Irish Hip Fracture Database National Report 2022', National Office of Clinical Audit, Dublin, Nov. 2023. [Online]. Available: https://www.noca.ie/publications

[3] Fortune Business Insights, 'Orthopedic Implants Market Size, Share & Industry Analysis, By Product (Joint Reconstruction (Knee, Hip, and Extremities), Spinal Implants (Spinal Fusion Devices, and Spinal Non-fusion Devices), Trauma Implants, and Others), By End-user (Hospitals & Ambulatory Surgery Centers and Orthopedic Clinics & Others), and Regional Forecast, 2024-2032', 2023. Accessed: Nov. 03, 2024. [Online]. Available: https://www.precedenceresearch.com/orthopedic-implant-market#:~:text=The%20global%20orthopedic%20implant%20market,forecast%20period%202023%20to%202032.

[4] 'About Osteoporosis', Irish Osteoporosis Society. Accessed: Nov. 03, 2024. [Online]. Available: https://www.irishosteoporosis.ie/information-support/about-osteoporosis/#accordion-2-10

[5] J. Mr Cashman *et al.*, 'Irish National Orthopaedic Register: First Report', Dublin, Nov. 2021. [Online]. Available: https://www.noca.ie/publications

[6] N. Li and Y. Zheng, 'Novel Magnesium Alloys Developed for Biomedical Application: A Review', *J Mater Sci Technol*, 2013, doi: 10.1016/j.jmst.2013.02.005.

[7] C. Liu, Z. Ren, Y. Xu, S. Pang, X. Zhao, and Y. Zhao, 'Biodegradable Magnesium Alloys Developed as Bone Repair Materials: A Review', 2018, *Hindawi Ltd. and John Wiley and Sons, Inc.* doi: 10.1155/2018/9216314.

[8] S. Sakai, T. Anada, K. Tsuchiya, H. Yamazaki, H. C. Margolis, and O. Suzuki, 'Comparative study on the resorbability and dissolution behavior of octacalcium phosphate, β-tricalcium phosphate, and hydroxyapatite under physiological conditions', *Dent Mater J*, vol. 35, no. 2, pp. 216–224, Mar. 2016, doi: 10.4012/dmj.2015-255.

[9] H. Gray, 'Anatomy of the Human Body', in *Anatomy of the Human Body*, 20th ed., W. H. Lewis, Ed., Philadelphia: Lea & Febiger, 1918, ch. Bone.

[10] ‘Anatomy & Physiology’, in *Anatomy & Physiology*, Houston, Texas: OpenStax College, Rice University, 2013, ch. Bone Tissu.

[11] R. L. Drake, A. Wayne Vogl, and A. W. M. Mitchell, ‘Skeletel System’, in *Gray’s Anatomy for Students*, 2nd ed., Elsevier, 2009, ch. Body Syste.

[12] A. Y. Yeung and R. Garg, ‘Sesamoid Bones’, *National Center for Biotechnology Information*, no. Anatomy, 2022, [Online]. Available: https://www.ncbi.nlm.nih.gov/books/NBK578171/#:~:text=A sesamoid bone is a,that particular muscle or tendon.

[13] J. A. Buckwalter and H. J. Mankin, ‘Articular cartilage: degeneration and osteoarthritis, repair, regeneration, and transplantation.’, *Instr Course Lect*, vol. 47, pp. 487–504, Jan. 1998.

[14] X. Wang *et al.*, ‘Topological Design and Additive Manufacturing of Porous Metals for Bone Scaffolds and Orthopaedic Implants: A Review’, *Biomaterials*, vol. 83, pp. 127–141, Mar. 2016.

[15] C. F. Guimaraes, L. Gasperini, A. P. Marques, and R. L. Reis, ‘The Stiffness of Living Tissues and its Implications for Tissue Engineering’, *Nat Rev Mater*, vol. 5, pp. 351–370, 2020.

[16] J. Young Rho, R. B. Ashman, and C. H. Turner, ‘Young’s Modulus of Trabecular and Cortical Bone Material: Ultrasonic and Microtensile Measurements’, *J Biomech*, vol. 26, no. 2, pp. 111–119, Feb. 1993.

[17] L. H. Trammell and A. M. Kroman, *Bone and Dental Histology*. Elsevier Inc., 2013. doi: 10.1016/B978-0-12-385189-5.00013-3.

[18] M. A. Adams, ‘Cells, Tissues, and Systems’, in *Gray’s Anatomy : The Anatomical Basis of Clinical Practice*, 41st ed., S. Standring and C. B. Wigley, Eds., London: Elsevier, 2021, ch. 1.5, pp. 85–127.

[19] A. R. Gillies and R. L. Lieber, ‘Structure and function of the skeletal muscle extracellular matrix’, *Muscle Nerve*, vol. 44, no. 3, pp. 318–331, 2011, doi: 10.1002/mus.22094.

[20] R. K. Fuchs, S. J. Warden, and C. H. Turner, ‘Bone anatomy, physiology and adaptation to mechanical loading’, *Bone Repair Biomaterials*, pp. 25–68, Jan. 2009, doi: 10.1533/9781845696610.1.25.

[21] A. I. Caplan, ‘Mesenchymal Stem Cells’, *Journal of Orthopaedic Research*, vol. 9, no. 5, pp. 641–650, 1991, doi: 10.1016/B978-0-12-809880-6.00014-X.

[22] E. Garcia *et al.*, ‘Cell-Line-Based Studies of Nanotechnology Drug-Delivery Systems: A Brief Review’, in *Nanocarriers for Drug Delivery: Nanoscience and Nanotechnology in Drug Delivery*, S. S. Mohapatra, S. Ranjan, N. Dasgupta, R. K. Mishra, and S. Thomas, Eds., Elsevier, 2019, ch. 12, pp. 375–393. Accessed: Aug. 21, 2024. [Online]. Available: https://www.sciencedirect.com/topics/engineering/mesenchymal-stem-cell

[23] W. Chen, Y. Shao, X. Li, G. Zhao, and J. Fu, ‘Nanotopographical surfaces for stem cell fate control: Engineering mechanobiology from the bottom’, Dec. 01, 2014, *Elsevier B.V.* doi: 10.1016/j.nantod.2014.12.002.

[24] H. K. Väänänen and T. Laitala-Leinonen, ‘Osteoclast lineage and function’, May 15, 2008. doi: 10.1016/j.abb.2008.03.037.

[25] A. E. Grigoriadis *et al.*, ‘Directed differentiation of hematopoietic precursors and functional osteoclasts from human ES and iPS cells’, *Blood*, vol. 115, no. 14, pp. 2769–2776, Apr. 2010, doi: 10.1182/blood-2009-07-234690.

[26] J. S. Kenkre and J. H. D. Bassett, ‘The bone remodelling cycle’, May 01, 2018, *SAGE Publications Ltd*. doi: 10.1177/0004563218759371.

[27] P. Bosch *et al.*, ‘Osteoprogenitor cells within skeletal muscle’, *Journal of Orthopaedic Research*, vol. 18, no. 6, pp. 933–944, Jan. 2000, doi: 10.1002/JOR.1100180613.

[28] M. E. Joyce, A. B. Roberts, M. B. Sporn, and M. E. Bolander, ‘Transforming growth factor-β and the initiation of chondrogenesis and osteogenesis in the rat femur’, *Journal of Cell Biology*, vol. 110, no. 6, pp. 2195–2207, 1990, doi: 10.1083/jcb.110.6.2195.

[29] M. R. Urist, R. J. Delange, G. A. M. Finerman, S. Science, N. Series, and N. May, ‘Bone Cell Differentiation and Growth Factors’, *Science (1979)*, vol. 220, no. 4598, pp. 680–686, 1983, [Online]. Available: https://www.jstor.org/stable/pdf/1690047.pdf?casa_token=GyH2JOZTWl8AAAAA:sLm6WFbPhZPTd5ppSyrWZgqZlNOdZBI58fbTA-yJKrsOuDYLRYWQtkGVC9vMHHzCqPgGorncX1LJrv2hPM3OXWRaE9MT9UP3wHCQ-IFZYem1IovIGQo3

[30] E. Bonucci, ‘Bone Mineralization’, *Frontiers in Biosceince*, no. 17, pp. 100–128, 2012.

[31] D. V. Novack and S. L. Teitelbaum, 'The osteoclast: Friend or foe?', *Annual Review of Pathology: Mechanisms of Disease*, vol. 3, pp. 457–484, 2008, doi: 10.1146/annurev.pathmechdis.3.121806.151431.

[32] L. F. Bonewald, 'The Amazing Osteocyte', *Journal of Bone and Mineral Research*, vol. 26, no. 2, pp. 229–238, 2011, doi: 10.1002/jbmr.320.

[33] L. F. Bonewald, 'Osteocytes', *Marcus and Feldman's Osteoporosis*, pp. 135–163, Jan. 2021, doi: 10.1016/B978-0-12-813073-5.00007-1.

[34] H. Gray, *Gray's Anatomy: The Anatomical Basis of Clinical Practice*, 41st ed. Philadelphia, PA: Elsevier, 2016.

[35] M. H. Ross and W. Pawlina, *Histology: A Text and Atlas*, 5th ed. Lippincott Williams & Wilkins, 2006.

[36] W. A. N. Dorland, *Dorland's Illustrated Medical Dictionary*, 32nd ed. Philadelphia, PA: Elsevier Saunders, 2011.

[37] C. Jerome, B. Hoch, and C. S. Carlson, 'Skeletal System', in *Comparative Anatomy and Histology*, 2nd ed., P. M. Treuting and S. M. Dintzis, Eds., Elsevier, 2018, ch. 5, pp. 67–88.

[38] S. G. D. Hegarty-Cremer *et al.*, 'How osteons form: A quantitative hypothesis-testing analysis of cortical pore filling and wall asymmetry', *Bone*, vol. 180, Mar. 2024, doi: 10.1016/j.bone.2023.116998.

[39] B. Chang and X. Liu, 'Osteon: Structure, Turnover, and Regeneration', Apr. 01, 2022, *Mary Ann Liebert Inc.* doi: 10.1089/ten.teb.2020.0322.

[40] B. Clarke, 'Normal Bone Anatomy and Physiology', *Clinical Journal of the American Society of Nephrology*, vol. 3, Nov. 2008, Accessed: Aug. 15, 2024. [Online]. Available: https://www.ncbi.nlm.nih.gov/pmc/articles/PMC3152283/

[41] H. M. Frost, *Bone Remodelling Dynamics*. Springfield IL: Charles C. Thomas, 1963.

[42] P. Rowe, A. Koller, and S. Sharma, 'Physiology, Bone Remodelling', in *StatPearls*, Treasure Island, Florida: StatPearls Publishing, 2023. Accessed: Nov. 03, 2024. [Online]. Available: https://www.ncbi.nlm.nih.gov/books/NBK499863/

[43] A. C. Ahn and A. J. Grodzinsky, 'Relevance of collagen piezoelectricity to "Wolff's Law": A critical review', Sep. 2009. doi: 10.1016/j.medengphy.2009.02.006.

[44] S. Bolamperti, I. Villa, and A. Rubinacci, 'Bone remodeling: an operational process ensuring survival and bone mechanical competence', Dec. 01, 2022, *Springer Nature*. doi: 10.1038/s41413-022-00219-8.

[45] N. A. Sims and T. J. Martin, 'Coupling the activities of bone formation and resorption: a multitude of signals within the basic multicellular unit', *Bonekey Rep*, vol. 3, Jan. 2014, doi: 10.1038/bonekey.2013.215.

[46] X. G. Borggaard, J. P. Roux, J. M. Delaisse, P. Chavassieux, C. M. Andreasen, and T. L. Andersen, 'Alendronate prolongs the reversal-resorption phase in human cortical bone remodeling', *Bone*, vol. 160, Jul. 2022, doi: 10.1016/j.bone.2022.116419.

[47] P. R. Jensen, T. L. Andersen, E. M. Hauge, J. Bollerslev, and J. M. Delaissé, 'A joined role of canopy and reversal cells in bone remodeling - Lessons from glucocorticoid-induced osteoporosis', *Bone*, vol. 73, pp. 16–23, Apr. 2015, doi: 10.1016/j.bone.2014.12.004.

[48] M. E. Abdelgawad *et al.*, 'Early reversal cells in adult human bone remodeling: osteoblastic nature, catabolic functions and interactions with osteoclasts', *Histochem Cell Biol*, vol. 145, no. 6, pp. 603–615, Jun. 2016, doi: 10.1007/s00418-016-1414-y.

[49] T. L. Andersen *et al.*, 'Understanding coupling between bone resorption and formation: Are reversal cells the missing link?', *American Journal of Pathology*, vol. 183, no. 1, pp. 235–246, Jul. 2013, doi: 10.1016/j.ajpath.2013.03.006.

[50] R. Marsell and T. A. Einhorn, 'The Biology of Fracture Healing', *Injury*, vol. 42, no. 6, pp. 551–555, 2011, doi: 10.1016/j.injury.2011.03.031.

[51] L. E. Claes and K. Ito, 'Biomechanics of Fracture Fixation and Fracture Healing', in *Basic Orthopaedic Biomechanics and Mechano-Biology*, 3rd ed., V. C. Mow and R. Huiskes, Eds., Wolters Kluwer Health, 2004, ch. 13.

[52] B. K. Hall, 'Repair of Fractures and Regeneration of Growth Plates', in *Bones and Cartilage: Developmental and Evolutionary Skeletal Biology*, 1st ed., Elsevier Science and Technology, 2005, ch. 29.

[53] A. Longoni, L. Utomo, A. Robinson, R. Levato, A. J. W. P. Rosenberg, and D. Gawlitta, 'Acceleration of Bone Regeneration Induced by a Soft-Callus Mimetic Material', *Advanced Science*, vol. 9, no. 6, Feb. 2022, doi: 10.1002/advs.202103284.

[54] H. Schell, G. N. Duda, A. Peters, S. Tsitsilonis, K. A. Johnson, and K. Schmidt-Bleek, 'The haematoma and its role in bone healing', *J Exp Orthop*, vol. 4, no. 1, Dec. 2017, doi: 10.1186/s40634-017-0079-3.

[55] T. A. Einhorn, 'The Cell and Molecular Biology of Fracture Healing', *Clinical Orthopaedic and Related Research*, vol. 355, pp. s7–s21, Oct. 1998.

[56] T. A. Einhorn and L. C. Gerstenfeld, 'Fracture healing: Mechanisms and interventions', Jan. 01, 2015, *Nature Publishing Group*. doi: 10.1038/nrrheum.2014.164.

[57] B. Furie, 'Bleeding and Blood Clotting', Encyclopaedia Britannica. Accessed: Nov. 08, 2024. [Online]. Available: https://www.britannica.com/science/bleeding

[58] C. S. Bahney *et al.*, 'Cellular biology of fracture healing', Jan. 01, 2019, *John Wiley and Sons Inc.* doi: 10.1002/jor.24170.

[59] B. I. Oladapo, S. O. Ismail, J. F. Kayode, and O. M. Ikumapayi, 'Piezoelectric effects on bone modeling for enhanced sustainability', *Mater Chem Phys*, vol. 305, Sep. 2023, doi: 10.1016/j.matchemphys.2023.127960.

[60] F. Shapiro, 'Bone Development and its Relation to Fracture Repair. The Role of Mesenchymal Osteoblasts and Surface Osteoblasts', *Eur Cell Mater*, vol. 15, pp. 53–76, 2008.

[61] K. J. Rambhia and P. X. Ma, 'Biomineralization and Bone Regeneration', in *Principles of Regenerative Medicine*, 3rd ed., A. Atala, R. Lanza, A. G. Mikos, and R. Nerem, Eds., Ann Arbor, MI: Elsevier, 2019, ch. 48, pp. 853–866. doi: 10.1016/B978-0-12-809880-6.00048-5.

[62] D. Saul and S. Khosla, 'Fracture Healing in the Setting of Endocrine Diseases, Aging, and Cellular Senescence', Dec. 01, 2022, *Endocrine Society*. doi: 10.1210/endrev/bnac008.

[63] P. Giannoudis, C. Tzioupis, T. Almalki, and R. Buckley, 'Fracture healing in osteoporotic fractures: Is it really different? - A basic science perspective', *Injury, Int. J Care Injured*, vol. 38, Mar. 2007, doi: 10.1016/j.injury.2007.02.014.

[64] P. Vestergaard, L. Rejnmark, and L. Mosekilde, 'Increased mortality in patients with a hip fracture-effect of pre-morbid conditions and post-fracture complications', *Osteoporosis International*, vol. 18, no. 12, pp. 1583–1593, Dec. 2007, doi: 10.1007/s00198-007-0403-3.

[65] J. R. Sheen, A. Mabrouk, and V. V Garla, 'Fracture Healing Overview', StatPearls. Accessed: Oct. 30, 2024. [Online]. Available: https://www.ncbi.nlm.nih.gov/books/NBK551678/

[66] R. A. Kayal *et al.*, 'Diminished bone formation during diabetic fracture healing is related to the premature resorption of cartilage associated with increased osteoclast activity', *Journal of Bone and Mineral Research*, vol. 22, no. 4, pp. 560–568, Apr. 2007, doi: 10.1359/jbmr.070115.

[67] J. E. Hellwinkel, Z. M. Working, L. Certain, A. J. García, J. C. Wenke, and C. S. Bahney, 'The intersection of fracture healing and infection: Orthopaedics research society workshop 2021', Mar. 01, 2022, *John Wiley and Sons Inc*. doi: 10.1002/jor.25261.

[68] M. T. Clayer and R. J. Bauze, 'Morbidity and mortality following fractures of the femoral neck and trochanteric region: Analysis of risk factors', *Journal of Trauma - Injury, Infection and Critical Care*, vol. 29, no. 12, pp. 1673–1678, 1989, doi: 10.1097/00005373-198912000-00016.

[69] E. J. Cheal, K. A. Mansmann, A. M. Digioia, W. C. Hayes, and S. M. Perren, 'Role of interfragmentary strain in fracture healing: Ovine model of a healing osteotomy', *Journal of Orthopaedic Research*, vol. 9, no. 1, pp. 131–142, 1991, doi: 10.1002/jor.1100090116.

[70] P. Brzozowski, C. Inculet, E. H. Schemitsch, and R. Zdero, 'Biomechanical testing of a computationally optimized far cortical locking plate versus traditional implants for distal femur fracture repair', *Clinical Biomechanics*, vol. 117, Jul. 2024, doi: 10.1016/j.clinbiomech.2024.106296.

[71] G. Rouhi and M. A. Hamedani, 'A Brief Introduction into Orthopaedic Implants', *Researchgate, Chapter*, no. january, pp. 1–19, 2012, Accessed: Apr. 08, 2020. [Online]. Available: https://www.researchgate.net/publication/309923041_A_BRIEF_INTRODUCTION_INTO_ORTHOPAEDIC_IMPLANTS_SCREWS_PLATES_AND_NAILS

[72] W. Jin and P. K. Chu, 'Orthopedic implants', *Encyclopedia of Biomedical Engineering*, vol. 1–3. Elsevier, pp. 425–439, Jan. 01, 2019. doi: 10.1016/B978-0-12-801238-3.10999-7.

[73] B. Abrahamsen, T. Van Staa, R. Ariely, M. Olson, and C. Cooper, 'Excess mortality following hip fracture: A systematic epidemiological review', Oct. 2009. doi: 10.1007/s00198-009-0920-3.

[74] M. S. Taljanovic, M. D. Jones, J. T. Ruth, J. B. Benjamin, J. E. Sheppard, and T. B. Hunter, 'Fracture Fixation', *RadioGraphics*, vol. 23, Nov. 2003.

[75] F. F. Buechel and M. J. Pappas, 'The Knee', in *Principals of Human Joint Replacement*, 2nd ed., Springer International Publishing AG, 2015, ch. 6.

[76] F. F. Buechel and M. J. Pappas, 'The Hip', in *Principles of Human Joint Replacement*, 2nd ed., Springer International Publishing, 2015, ch. 5, pp. 171–262. doi: 10.1007/978-3-319-15311-7_5.

[77] V. C. Mow and R. Huiskes, 'A Brief History of Science and Orthopaedic Biomechanics', in *Basic Orthopaedic Biomechanics and Mechano-Biology*, 3rd ed., V. C. Mow and R. Huiskes, Eds., Wolters Kluwer Health, 2004, ch. 1.

[78] S. Yang, L. M. Andras, G. J. Redding, and D. L. Skaggs, 'Early-onset scoliosis: A review of history, current treatment, and future directions', Jan. 01, 2016, *American Academy of Pediatrics*. doi: 10.1542/peds.2015-0709.

[79] H. Hassanzadeh and K. M. Kebaish, 'Surgery for Adult Spinal Deformity', in *Spinal Deformities: The Essentials*, 2nd ed., R. F. Heary and T. J. Albert, Eds., Thieme Medical Publishers, Inc, 2014. [Online]. Available: http://ebookcentral.proquest.com/lib/dcu/detail.action?docID=1831164.

[80] R. W. Tracey, J. P. Cody, R. A. Lehman, and L. G. Lenke, 'Posterior Approach in Thoracic Deformity', in *Spinal Deformities: The Essentials*, 2nd ed., R. F. Heary and T. J. Albert, Eds., Thieme Medical Publishers, Inc, 2014, ch. 6. [Online]. Available: http://ebookcentral.proquest.com/lib/dcu/detail.action?docID=1831164.

[81] P. Gauthier, P. Slulitel, A. Speirs, F. Laude, W. T. Gofton, and P. E. Beaule, 'Cerclage wire or positional cortical screw for the treatment of intraoperative calcar fractures during primary total hip arthroplasty? A biomechanical study', *Clinical Biomechanics*, vol. 101, Jan. 2023, doi: 10.1016/j.clinbiomech.2022.105848.

[82] Z. Chen, R. Luo, F. Xing, and Z. Xiang, 'External fixation versus intramedullary nailing for the treatment of open tibial shaft fractures: A meta-analysis of randomized controlled

trials', *Health Sciences Review*, vol. 10, p. 100152, Mar. 2024, doi: 10.1016/j.hsr.2024.100152.

[83] A. Sedmak *et al.*, 'Fatigue life assessment of orthopedic plates made of Ti6Al4V', *Eng Fail Anal*, vol. 137, Jul. 2022, doi: 10.1016/j.engfailanal.2022.106259.

[84] Y. Xie *et al.*, 'A biodegradable, osteo-regenerative and biomechanically robust polylactide bone screw for clinical orthopedic surgery', *Int J Biol Macromol*, vol. 283, Dec. 2024, doi: 10.1016/j.ijbiomac.2024.137477.

[85] L. A. Pruitt and A. M. Chakravartula, 'Metals for medical implants', in *Mechanics of Biomaterials: Fundamental Principles for Implant Design*, 1st ed., L. A. Pruitt and A. M. Chakravartula, Eds., Cambridge University Press, 2011, ch. 1.2. [Online]. Available: http://ebookcentral.proquest.com/lib/dcu/detail.action?docID=774986.

[86] M. Hamadouche and L. Sedel, 'Ceramics in orthopaedics', *Journal of Bone and Joint Surgery - Series B*, vol. 82, no. 8, pp. 1095–1099, 2000, doi: 10.1302/0301-620X.82B8.11744.

[87] G. Szczęsny, M. Kopec, D. J. Politis, Z. L. Kowalewski, A. Łazarski, and T. Szolc, 'A Review on Biomaterials for Orthopaedic Surgery and Traumatology: From Past to Present', *Materials*, vol. 15, no. 10, 2022, doi: 10.3390/ma15103622.

[88] S. Bose and A. Bandyopadhyay, 'Introduction to Biomaterials', in *Characterization of Biomaterials*, Elsevier Inc., 2013, ch. 1, pp. 1–9. doi: 10.1016/B978-0-12-415800-9.00001-2.

[89] E. J. Heard, 'Simple Stress and Strain', in *Mechanics of Materials 1*, 1st ed., E. J. Hearn, Ed., Butterworth-Heinemann, 1997, ch. 1, pp. 1–26.

[90] D. L. Millis, 'Responses of Musculoskeletal Tissues to Disuse and Remobilization', in *Canine Rehabilitation and Physical Therapy*, 2nd ed., D. L. Millis and D. Levine, Eds., Saunders, 2014, ch. 7.

[91] M. M. Soliman *et al.*, 'Stress transfer, stress shielding, and micro-movement analysis in the implanted femoral bone region with various hip implant stem materials: A finite element approach', *Mater Today Commun*, vol. 41, Dec. 2024, doi: 10.1016/j.mtcomm.2024.110932.

[92] L. A. Pruitt and A. M. Chakravartula, 'Part II: Mechanics', in *Mechanics of Biomaterials: Fundamental Principles for Implant Design*, 1st ed., L. A. Pruitt and A. M. Chakravartula, Eds., Cambridge University Press, 2011, ch. 2, pp. 165–394.

[93] Y. Murakami, 'Effect of Surface Roughness on Fatigue Strength', in *Metal Fatigue*, 2nd ed., Y. Murikami, Ed., Academic Press, 2019, ch. 16, pp. 407–430.

[94] Y. C. Fung, 'Bone and Cartilage', in *Biomechanics: Mechanical Properties of Living Tissue*, 2nd ed., Y. C. Fung, Ed., Springer, 1993, ch. 12, pp. 499–543.

[95] D. R. H. Jones and M. F. Ashby, 'Yield Strength, Tensile Strength, and Ductility', in *Engineering and Materials 1*, 5th ed., D. R. H. Jones and M. F. Ashby, Eds., Butterworth-Heinemann, 2019, ch. 9, pp. 137–156.

[96] W. Abd-Elaziem, M. A. Darwish, A. Hamada, and W. M. Daoush, 'Titanium-Based alloys and composites for orthopedic implants Applications: A comprehensive review', *Mater Des*, vol. 241, May 2024, doi: 10.1016/j.matdes.2024.112850.

[97] A. Vaidya and K. Pathak, 'Mechanical Stability of Dental Materials', in *Applications of Nanocomposite Materials in Dentistry*, A. M. Asiri Inamuddin and A. Mohammad, Eds., Woodhead Publishing, 2018, ch. 17, pp. 285–305.

[98] S. Papavinasam, 'Mechanisms', in *Corrosion Control in the Oil and Gas Industry*, S. Papavinasam, Ed., Gulf Professional Publishing, 2014, ch. 5.

[99] 'Glossary of Biocompatibility Terms', U.S. Food and Drug Administration. Accessed: Dec. 01, 2024. [Online]. Available: https://www.fda.gov/medical-devices/biocompatibility-assessment-resource-center/glossary-biocompatibility-terms#:~:text=%22The%20ability%20of%20a%20device,Materials%3A%20Fundamentals%20of%20Biocompatibility.%22

[100] C. Zidrou, A. Kapetanou, and S. Rizou, 'The effect of drugs on implant osseointegration-A narrative review', Aug. 01, 2023, *Elsevier Ltd*. doi: 10.1016/j.injury.2023.110888.

[101] V. Perrotti, A. Piattelli, A. Quaranta, G. Gómez-Moreno, and G. Iezzi, 'Biocompatibility of dental biomaterials', in *Biocompatibility of Dental Biomaterials*, Woodhead Publishing, 2016, ch. 1, pp. 1–7. doi: 10.1016/B978-0-08-100884-3.00001-1.

[102] M. M. Germaini, S. Belhabib, S. Guessasma, R. Deterre, P. Corre, and P. Weiss, 'Additive manufacturing of biomaterials for bone tissue engineering – A critical review of the

state of the art and new concepts', Oct. 01, 2022, *Elsevier Ltd*. doi: 10.1016/j.pmatsci.2022.100963.

[103] S. Ramakrishna and Z. M. Huang, 'Biocomposites', vol. 9, I. Milne, B. Karihaloo, and R. O. Ritchie, Eds., Elsevier Science, 2003, ch. 9.6.

[104] A. Goharian, 'Fundamentals in Loosening and Osseointegration of Orthopedic Implants', in *Osseointegration of Orthopaedic Implants*, A. Goharian, Ed., Academic Press, 2019, ch. 1, pp. 1–26. doi: https://doi.org/10.1016/C2016-0-04956-2.

[105] P.-I. Branemark, 'Osseointegration and its Experimental Background', *J Prosthet Dent*, vol. 50, no. 3, pp. 399–410, Sep. 1983.

[106] K. C. Walley Bcs, M. B. Bcs, T. Gonzalez, and A. Nazarian, 'The Chronicle of a Stainless Steel Orthopaedic Implant', *Orthop J Harv Med Sch*, vol. 17, pp. 68–74, Jun. 2016.

[107] S. Yadav, 'A Review on Surface Treatment of Stainless Steel Orthopedic Implants', 2016. [Online]. Available: www.globalresearchonline.net

[108] K.-K. Chew, S. H. S. Zein, and A. L. Ahmad, 'The corrosion scenario in human body: Stainless steel 316L orthopaedic implants', *Nat Sci (Irvine)*, vol. 04, no. 03, pp. 184–188, 2012, doi: 10.4236/ns.2012.43027.

[109] A. A. Ahmed, M. Mhaede, M. Basha, M. Wollmann, and L. Wagner, 'The effect of shot peening parameters and hydroxyapatite coating on surface properties and corrosion behavior of medical grade AISI 316L stainless steel', *Surf Coat Technol*, vol. 280, pp. 347–358, 2015, doi: 10.1016/j.surfcoat.2015.09.026.

[110] K. Moghadasi *et al.*, 'A review on biomedical implant materials and the effect of friction stir based techniques on their mechanical and tribological properties', Mar. 01, 2022, *Elsevier Editora Ltda*. doi: 10.1016/j.jmrt.2022.01.050.

[111] M. Long and H. J. Rack, 'Titanium alloys in total joint replacement-a materials science perspective', 1998.

[112] H. J. Rack and J. I. Qazi, 'Titanium alloys for biomedical applications', *Materials Science and Engineering C*, vol. 26, no. 8, pp. 1269–1277, Sep. 2006, doi: 10.1016/j.msec.2005.08.032.

[113] K. A. Mann and M. J. Allen, 'Biomaterials in Orthopaedic Practice', in *Orthopaedic Basic Science: Foundations of Clinical Practice, Fourth Edition*, 5th ed., no. 2020, Wolters Kluwer Health, 2018, ch. 6, pp. 69–85.

[114] F. A. Rodriguez-Gonzalez, 'Selected Applications of Biomaterials in Orthopaedic Surgery', in *Biomaterials in Orthopaedic Surgery*, 1st ed., ASM International, 2009, ch. 6.

[115] M. P. Staiger, A. M. Pietak, J. Huadmai, and G. Dias, 'Magnesium and its alloys as orthopedic biomaterials: A review', Mar. 2006. doi: 10.1016/j.biomaterials.2005.10.003.

[116] E. Ghali, 'Activity and passivity of magnesium (Mg) and its alloys', in *Corrosion of Magnesium Alloys*, G. Song, Ed., Woodhead Publishing, 2011, ch. 2, pp. 66–114. doi: 10.1533/9780857091413.1.66.

[117] D. Bairagi and S. Mandal, 'A comprehensive review on biocompatible Mg-based alloys as temporary orthopaedic implants: Current status, challenges, and future prospects', Mar. 01, 2022, *National Engg. Reaserch Center for Magnesium Alloys*. doi: 10.1016/j.jma.2021.09.005.

[118] V. Tsakiris, C. Tardei, and F. M. Clicinschi, 'Biodegradable Mg alloys for orthopedic implants – A review', Nov. 15, 2021, *National Engg. Reaserch Center for Magnesium Alloys*. doi: 10.1016/j.jma.2021.06.024.

[119] J. Song, J. Chen, X. Xiong, X. Peng, D. Chen, and F. Pan, 'Research advances of magnesium and magnesium alloys worldwide in 2021', *Journal of Magnesium and Alloys*, vol. 10, no. 4, pp. 863–898, Apr. 2022, doi: 10.1016/j.jma.2022.04.001.

[120] P. Kumar Rout, S. Roy, and D. Rathore, 'Recent advances in the development of Mg-Ca-Zn alloys as biodegradable orthopedic implants', *Mater Today Proc*, Jul. 2023, doi: 10.1016/j.matpr.2023.06.341.

[121] C. A. Niranjan *et al.*, 'Magnesium alloys as extremely promising alternatives for temporary orthopedic implants – A review', Aug. 01, 2023, *KeAi Communications Co.* doi: 10.1016/j.jma.2023.08.002.

[122] J. Liu *et al.*, 'Biodegradable magnesium alloy WE43 porous scaffolds fabricated by laser powder bed fusion for orthopedic applications: Process optimization, in vitro and in vivo investigation', *Bioact Mater*, vol. 16, no. January, pp. 301–319, 2022, doi: 10.1016/j.bioactmat.2022.02.020.

[123] J. E. Park *et al.*, 'Corrosion properties and biocompatibility of strontium doped calcium phosphate coated magnesium prepared by electrodeposition', *Mater Today Commun*, vol. 31, p. 103759, Jun. 2022, doi: 10.1016/J.MTCOMM.2022.103759.

[124] Y. Zhang, G. Zhang, and M. Wei, 'Controlling the biodegradation rate of magnesium using biomimetic apatite coating', *J Biomed Mater Res B Appl Biomater*, vol. 89, no. 2, pp. 408–414, May 2009, doi: 10.1002/jbm.b.31228.

[125] J. Eschweiler *et al.*, 'High-Performance Ceramics in Musculoskeletal Surgery: Current Use and Future Perspectives', Mar. 01, 2024, *Multidisciplinary Digital Publishing Institute (MDPI)*. doi: 10.3390/ceramics7010020.

[126] M. Bittner-Frank, A. G. Reisinger, O. G. Andriotis, D. H. Pahr, and P. J. Thurner, 'Cortical and trabecular mechanical properties in the femoral neck vary differently with changes in bone mineral density', *JBMR Plus*, vol. 8, no. 6, Jun. 2024, doi: 10.1093/jbmrpl/ziae049.

[127] AZO Materials, 'Alumina as a Biomaterial (99.5% Alumina)', AZO Materials. Accessed: Jul. 28, 2025. [Online]. Available: https://www.azom.com/properties.aspx?ArticleID=105

[128] R. A. Maier, A. J. Allen, B. Cox, and I. Levin, 'Interlaboratory study of flexural strength in additively manufactured alumina', *Journal of the American Ceramic Society*, vol. 108, no. 2, Feb. 2025, doi: 10.1111/jace.20133.

[129] E. F. Morgan, G. U. Unnikrisnan, and A. I. Hussein, 'Bone Mechanical Properties in Healthy and Diseased States', Jun. 04, 2018, *Annual Reviews Inc.* doi: 10.1146/annurev-bioeng-062117-121139.

[130] M. R. Senra and M. de F. Vieira Marques, 'Synthetic polymeric materials for bone replacement', 2020, *MDPI AG*. doi: 10.3390/jcs4040191.

[131] P. Ducheyne, K. Healy, D. W. Hutmacher, D. W. Grainger, and C. J. Kirkpatrick, *Comprehensive Biomaterials*, 1st ed. Elsevier Science, 2011.

[132] A. Mehjabeen, T. Song, W. Xu, H. P. Tang, and M. Qian, 'Zirconium Alloys for Orthopaedic and Dental Applications', Sep. 01, 2018, *Wiley-VCH Verlag*. doi: 10.1002/adem.201800207.

[133] Y. Zhu *et al.*, '3D printed zirconia ceramic hip joint with precise structure and broad-spectrum antibacterial properties', *Int J Nanomedicine*, vol. 14, pp. 5977–5987, 2019, doi: 10.2147/IJN.S202457.

[134] E. Meier, K. Gelse, K. Trieb, M. Pachowsky, F. F. Hennig, and A. Mauerer, 'First clinical study of a novel complete metal-free ceramic total knee replacement system', *J Orthop Surg Res*, vol. 11, no. 1, Feb. 2016, doi: 10.1186/s13018-016-0352-7.

[135] A. H. De Aza, J. Chevalier, G. Fantozzi, M. Schehl, and R. Torrecillas, 'Crack growth resistance of alumina, zirconia and zirconia toughened alumina ceramics for joint prostheses', 2002.

[136] P. Massin, R. Lopes, B. Masson, and D. Mainard, 'Does Biolox® Delta ceramic reduce the rate of component fractures in total hip replacement?', Oct. 01, 2014, *Elsevier Masson SAS*. doi: 10.1016/j.otsr.2014.05.010.

[137] S. F. Hulbert, J. J. Klawitter, and L. S. Bowman, 'History of Ceramic Orthopedic Implants', *Mater Res Bull*, vol. 7, pp. 1239–1246, Aug. 1979.

[138] J. van Loon *et al.*, 'Ceramic-on-ceramic vs ceramic-on-polyethylene, a comparative study with 10-year follow-up', *World J Orthop*, vol. 12, no. 1, pp. 14–23, Jan. 2021, doi: 10.5312/WJO.V12.I1.14.

[139] R. Z. LeGeros, 'Calcium phosphate-based osteoinductive materials', Nov. 2008. doi: 10.1021/cr800427g.

[140] P. W. Brown, 'Calcium Phosphates in Biomedical Engineering', *Encyclopedia of Materials: Science and Technology*. Pergammon Press, pp. 893–897, 2001.

[141] T. KANAZAWA and H. MONMA, 'Bioceramics. Especially calcium phosphates biomaterials.', *Shigen-to-Sozai*, vol. 111, no. 4, pp. 199–204, 1995, doi: 10.2473/shigentosozai.111.199.

[142] J. Jones, 'Bioactive ceramics and glasses', 2007. doi: 10.1533/B978-1-84569-176-9.50003-4.

[143] S. Saber-Samandari, K. Alamara, and S. Saber-Samandari, 'Calcium phosphate coatings: Morphology, micro-structure and mechanical properties', *Ceram Int*, vol. 40, no. 1, pp. 563–572, Jan. 2014, doi: 10.1016/J.CERAMINT.2013.06.038.

[144] Y. Su, I. Cockerill, Y. Zheng, L. Tang, Y. X. Qin, and D. Zhu, 'Biofunctionalization of metallic implants by calcium phosphate coatings', *Bioact Mater*, vol. 4, pp. 196–206, Dec. 2019, doi: 10.1016/J.BIOACTMAT.2019.05.001.

[145] N. Eliaz and N. Metoki, 'Calcium phosphate bioceramics: A review of their history, structure, properties, coating technologies and biomedical applications', *Materials*, vol. 10, no. 4, Mar. 2017, doi: 10.3390/ma10040334.

[146] R. I. M. Asri, W. S. W. Harun, M. A. Hassan, S. A. C. Ghani, and Z. Buyong, 'A review of hydroxyapatite-based coating techniques: Sol-gel and electrochemical depositions on biocompatible metals', Apr. 01, 2016, *Elsevier Ltd*. doi: 10.1016/j.jmbbm.2015.11.031.

[147] J. L. Bystrom and M. Pujari-Palmer, 'Phosphoserine functionalized cements preserve metastable phases, and reprecipitate octacalcium phosphate, hydroxyapatite, dicalcium phosphate, and amorphous calcium phosphate, during degradation, in vitro', *J Funct Biomater*, vol. 10, no. 4, 2019, doi: 10.3390/jfb10040054.

[148] P. Habibovic, F. Barrère, C. A. Van Blitterswijk, K. De Groot, and P. Layrolle, 'Biomimetic hydroxyapatite coating on metal implants', *Journal of the American Ceramic Society*, vol. 85, no. 3, pp. 517–522, 2002, doi: 10.1111/j.1151-2916.2002.tb00126.x.

[149] N. Ito, M. Kamitakahara, M. Yoshimura, and K. Ioku, 'Importance of nucleation in transformation of octacalcium phosphate to hydroxyapatite', *Materials Science and Engineering C*, vol. 40, pp. 121–126, 2014, doi: 10.1016/j.msec.2014.03.034.

[150] M. C. Tronco, J. B. Cassel, and L. A. dos Santos, 'α-TCP-based calcium phosphate cements: A critical review', Oct. 01, 2022, *Acta Materialia Inc*. doi: 10.1016/j.actbio.2022.08.040.

[151] S. Sakai, T. Anada, K. Tsuchiya, H. Yamazaki, H. C. Margolis, and O. Suzuki, 'Study on Dissolution Behaviour of HA, TCP, OCP', *Dent Mater J*, vol. 35, no. 2, pp. 216–224, 2018.

[152] W. E. Brown, J. P. Smith, J. R. Lehr, and A. W. Frazier, 'Octacalcium phosphate and hydroxyapatite: crystallographic and chemical relations between octacalcium phosphate and hydroxyapatite', *Nature*, vol. 196, no. 4859, pp. 1050–1055, 1962, doi: 10.1038/1961050a0.

[153] P. Kasten *et al.*, 'Comparison of human bone marrow stromal cells seeded on calcium-deficient hydroxyapatite, β-tricalcium phosphate and demineralized bone matrix',

Biomaterials, vol. 24, no. 15, pp. 2593–2603, 2003, doi: 10.1016/S0142-9612(03)00062-0.

[154] D. Xidaki *et al.*, 'Synthesis of hydroxyapatite, β-Tricalcium phosphate and biphasic calcium phosphate particles to act as local delivery carriers of curcumin: Loading, release and in vitro studies', *Materials*, vol. 11, no. 4, 2018, doi: 10.3390/ma11040595.

[155] J. Xie and B. L. Luan, 'Formation of hydroxyapatite coating using novel chemo-biomimetic method', *J Mater Sci Mater Med*, vol. 19, no. 10, pp. 3211–3220, Oct. 2008, doi: 10.1007/s10856-008-3451-0.

[156] J. Chen *et al.*, 'Recent advances on development of hydroxyapatite coating on biodegradable magnesium alloys: A review', Oct. 01, 2021, *MDPI*. doi: 10.3390/ma14195550.

[157] O. Suzuki, M. Nakamura, Y. Miyasaka, M. Kagayama, and M. Sakurai, 'Bone Formation on Synthetic Precursors of Hydroxyapatite', 1991.

[158] S. Rujitanapanich, P. Kumpapan, and P. Wanjanoi, 'Synthesis of hydroxyapatite from oyster shell via precipitation', in *Energy Procedia*, Elsevier Ltd, 2014, pp. 112–117. doi: 10.1016/j.egypro.2014.07.138.

[159] K. Matsunaga, T. Kubota, K. Toyoura, and A. Nakamura, 'First-principles calculations of divalent substitution of Ca2+ in tricalcium phosphates', *Acta Biomater*, vol. 23, pp. 329–337, Sep. 2015, doi: 10.1016/j.actbio.2015.05.014.

[160] E. Davies *et al.*, 'Citrate bridges between mineral platelets in bone', *Proc Natl Acad Sci U S A*, vol. 111, no. 14, 2014, doi: 10.1073/pnas.1315080111.

[161] O. Suzuki, 'Octacalcium phosphate (OCP)-based bone substitute materials', *Japanese Dental Science Review*, vol. 49, no. 2, pp. 58–71, 2013, doi: 10.1016/j.jdsr.2013.01.001.

[162] O. Suzuki and T. Anada, 'Effect of octacalcium phosphate-based bone substitute materials on oriented bone regeneration', in *Key Engineering Materials*, Trans Tech Publications Ltd, 2017, pp. 223–227. doi: 10.4028/www.scientific.net/KEM.758.223.

[163] O. Suzuki, Y. Shiwaku, and R. Hamai, 'Octacalcium Phosphate Bone Substitute Materials: Comparison Between Properties of Biomaterials and Other Calcium Phosphate Materials', *Dent Mater J*, no. 39, pp. 187–199, 2020.

[164] G. W. Bernard and D. C. Pease, 'An Electron Microscopic Study of Initial lntramembranous Osteogenesis', *American Journal of Anatomy*, vol. 125, Jul. 1969.

[165] K. Okuyama *et al.*, 'Differentiation of committed osteoblast progenitors by octacalcium phosphate compared to calcium-deficient hydroxyapatite in Lepr-cre/Tomato mouse tibia', *Acta Biomater*, vol. 142, pp. 332–344, Apr. 2022, doi: 10.1016/J.ACTBIO.2022.02.016.

[166] O. Suzuki, Y. Shiwaku, and R. Hamai, 'Octacalcium phosphate bone substitute materials: Comparison between properties of biomaterials and other calcium phosphate materials', *Dent Mater J*, vol. 39, no. 2, pp. 187–199, 2020, doi: 10.4012/dmj.2020-001.

[167] V. C. Misra, Y. Chakravarthy, N. Khare, K. Singh, and S. Ghorui, 'Strongly adherent Al2O3 coating on SS 316L: Optimization of plasma spray parameters and investigation of unique wear resistance behaviour under air and nitrogen environment', *Ceram Int*, vol. 46, no. 7, pp. 8658–8668, 2020, doi: 10.1016/j.ceramint.2019.12.099.

[168] R. Chaharmahali, A. Fattah-alhosseini, and K. Babaei, 'Surface characterization and corrosion behavior of calcium phosphate (Ca-P) base composite layer on Mg and its alloys using plasma electrolytic oxidation (PEO): A review', Jan. 15, 2021, *National Engg. Reaserch Center for Magnesium Alloys*. doi: 10.1016/j.jma.2020.07.004.

[169] J. E. Gray and B. Luan, 'Protective coatings on magnesium and its alloys - A critical review', Apr. 18, 2002. doi: 10.1016/S0925-8388(01)01899-0.

[170] K. A. Prosolov *et al.*, 'RF magnetron-sputtered coatings deposited from biphasic calcium phosphate targets for biomedical implant applications', *Bioact Mater*, vol. 2, no. 3, pp. 170–176, Sep. 2017, doi: 10.1016/j.bioactmat.2017.07.003.

[171] R. A. Surmenev, A. A. Ivanova, M. Epple, V. F. Pichugin, and M. A. Surmeneva, 'Physical principles of radio-frequency magnetron sputter deposition of calcium-phosphate-based coating with tailored properties', *Surf Coat Technol*, vol. 413, May 2021, doi: 10.1016/j.surfcoat.2021.127098.

[172] S. Keim, J. G. Brunner, B. Fabry, and S. Virtanen, 'Control of magnesium corrosion and biocompatibility with biomimetic coatings', *J Biomed Mater Res B Appl Biomater*, vol. 96 B, no. 1, pp. 84–90, Jan. 2011, doi: 10.1002/jbm.b.31742.

[173] F. Baino and S. Yamaguchi, 'The use of simulated body fluid (SBF) for assessing materials bioactivity in the context of tissue engineering: Review and challenges', *Biomimetics*, vol. 5, no. 4, pp. 1–19, 2020, doi: 10.3390/biomimetics5040057.

[174] Á. Re, P. Layrolle, C. a V. a N. Blitterswijk, and K. D. E. Groot, 'Biomimetic coatings on titanium: a crystal growthstudy of octacalcium phosphate', *J Mater Sci Mater Med*, vol. 12, pp. 529–534, 2001.

[175] F. Barrère, P. Layrolle, C. A. Van Blitterswijk, and K. De Groot, 'Biomimetic coatings on titanium: A crystal growth study of octacalcium phosphate', *J Mater Sci Mater Med*, vol. 12, no. 6, pp. 529–534, 2001, doi: 10.1023/A:1011271713758.

[176] S. Leeuwenburgh *et al.*, 'Osteoclastic resorption of biomimetic calcium phosphate coatings in vitro', *J Biomed Mater Res*, 2001, doi: 10.1002/1097-4636(200108)56:2<208::AID-JBM1085>3.0.CO;2-R.

[177] R. Hu, C. Lin, H. Shi, and H. Wang, 'Electrochemical deposition mechanism of calcium phosphate coating in dilute Ca-P electrolyte system', *Mater Chem Phys*, vol. 115, no. 2–3, pp. 718–723, Jun. 2009, doi: 10.1016/j.matchemphys.2009.02.022.

[178] D. T. M. Thanh *et al.*, 'Controlling the electrodeposition, morphology and structure of hydroxyapatite coating on 316L stainless steel', *Materials Science and Engineering C*, vol. 33, no. 4, pp. 2037–2045, May 2013, doi: 10.1016/j.msec.2013.01.018.

[179] G. Yang, 'Effect of Electrochemically Deposited Nanohydroxyapatite on Bone Bonding of Sandblasted/Dual Acid-Etched Titanium Implant', *Int J Oral Maxillofac Implants*, vol. 27, no. 5, pp. 790–799, Sep. 2009, [Online]. Available: https://www.researchgate.net/publication/38044642

[180] R. Hu, C. Lin, H. Shi, and H. Wang, 'Electrochemical deposition mechanism of calcium phosphate coating in dilute Ca-P electrolyte system', *Mater Chem Phys*, vol. 115, no. 2–3, pp. 718–723, Jun. 2009, doi: 10.1016/j.matchemphys.2009.02.022.

[181] R. LeGeros, 'Rapid Communication Preparation of Octacalcium Phosphate (OCP): A Direct Fast Method', *Calcif Tissue Int*, pp. 194–197, 1985.

[182] M. Stefanic, K. Krnel, I. Pribosic, and T. Kosmac, 'Rapid biomimetic deposition of octacalcium phosphate coatings on zirconia ceramics (Y-TZP) for dental implant applications', *Appl Surf Sci*, vol. 258, no. 10, pp. 4649–4656, Mar. 2012, doi: 10.1016/j.apsusc.2012.01.048.

[183] E. D. Eanes, I. H. Gillessen, and A. S. Posner, 'Intermediate States in the Precipitation of Hydroxyapatite', in *Nature*, vol. 208, 1965, pp. 365–367. doi: 10.1038/208365a0.

[184] J. Walker, S. Shadanbaz, and G. J. Dias, 'Magnesium alloys : Predicting in vivo corrosion with in vitro immersion testing Acta Biomaterialia Calcium phosphate coatings on magnesium alloys for biomedical applications : A review', *Acta Biomater*, vol. 8, no. 1, pp. 20–30, 2012, doi: 10.1016/j.actbio.2011.10.016.

[185] E. Gemelli, C. X. Resende, and G. D. De Almeida Soares, 'Nucleation and growth of octacalcium phosphate on treated titanium by immersion in a simplified simulated body fluid', *J Mater Sci Mater Med*, vol. 21, no. 7, pp. 2035–2047, 2010, doi: 10.1007/s10856-010-4074-9.

[186] M. Stefanic, K. Krnel, I. Pribosic, and T. Kosmac, 'Rapid biomimetic deposition of octacalcium phosphate coatings on zirconia ceramics (Y-TZP) for dental implant applications', *Appl Surf Sci*, vol. 258, no. 10, pp. 4649–4656, Mar. 2012, doi: 10.1016/j.apsusc.2012.01.048.

[187] 'ASTM G31-72: Guide for Laboratory Immersion Corrosion Testing of Metals', Jul. 01, 2012, *ASTM International, West Conshohocken, PA*. doi: 10.1520/G0031-12A.

[188] 'ASTM D3359-22: Test Methods for Rating Adhesion by Tape Test', Jul. 01, 2022, *ASTM International, West Conshohocken, PA*. doi: 10.1520/D3359-22.

[189] L. Liu *et al.*, 'Degradation rates of pure zinc, magnesium, and magnesium alloys measured by volume loss, mass loss, and hydrogen evolution', *Applied Sciences (Switzerland)*, vol. 8, no. 9, Aug. 2018, doi: 10.3390/app8091459.

[190] 'Magnesium Elektron WE43 Alloy (UNSM18430)', Jun. 2013. [Online]. Available: https://www.azom.com/article.aspx?ArticleID=9279

[191] M. Sahadat Hossain and S. Ahmed, 'FTIR spectrum analysis to predict the crystalline and amorphous phases of hydroxyapatite: a comparison of vibrational motion to reflection', *RSC Adv*, vol. 13, no. 21, pp. 14625–14630, May 2023, doi: 10.1039/d3ra02580b.

[192] J. Coates, 'Interpretation of Infrared Spectra, A Practical Approach'.

[193] L. Berzina-Cimdina and N. Borodajenko, 'Research of Calcium Phosphates Using Fourier Transform Infrared Spectroscopy', in *Infrared Spectroscopy - Materials Science, Engineering and Technology*, InTech, 2012. doi: 10.5772/36942.

[194] I. V. Smirnov *et al.*, 'Structural modification of titanium surface by octacalcium phosphate via pulsed laser deposition and chemical treatment', *Bioact Mater*, vol. 2, no. 2, pp. 101–107, Jun. 2017, doi: 10.1016/j.bioactmat.2017.03.002.

[195] F. Barrère, P. Layrolle, C. a V. a N. Blitterswijk, and K. D. E. Groot, 'Biomimetic coatings on titanium: a crystal growth study of octacalcium phosphate', *J Mater Sci Mater Med 12*, vol. 2, pp. 529–534, 2001.

[196] A. Bigi *et al.*, 'Morphological and Structural Modifications of Octacalcium Phosphate Induced by Poly-L-Aspartate', *Cryst Growth Des*, vol. 4, no. 1, pp. 141–146, Jan. 2004, doi: 10.1021/cg034078d.

[197] Y. Liu, R. M. Shelton, and J. E. Barralet, 'Homogeneous Octacalcium Phosphate Precipitation: Effect of Temperature and pH', in *Key Engineering Materials*, Trans Tech Publications Ltd, 2004, pp. 79–82. doi: 10.4028/www.scientific.net/kem.254-256.79.

[198] J. F. De Rooij, J. C. Heughebaert, and G. H. Nancollas, 'A pH Study of Calcium Phosphate Seeded Precipitation', 1984.

[199] W. Wu and G. H. Nancollas, 'Nucleation and Crystal Growth of Octacalcium Phosphate on Titanium Oxide Surfaces', 1997.

[200] T. Hayakawa, M. Yoshinari, K. Nemoto, J. G. C. Wolke, and J. A. Jansen, 'Effect of surface roughness and calcium phosphate coating on the implant/bone response.', *Clin Oral Impl Res*, vol. 11, pp. 296–304, 2000.

[201] M. H. Fernandes, 'Effect of Stainless Steel Corrosion Products on In Vitro Biomineralization', *J Biomater Appl*, vol. 14, no. 2, Oct. 1999.

[202] D. G. A. Nelson and J. D. Mclean, 'High-Resolution Electron Microscopy of Octacalcium Phosphate and its Hydrolysis Products', *Calcif Tissue Int*, vol. 36, pp. 219–232, 1984.

[203] S. Swain and T. R. Rautray, 'Effect of Surface Roughness on Titanium Medical Implants', in *Nanostructured Materials and their Applications.*, B. P. Swain, Ed., Springer, 2021, ch. 3.

[204] K. Y. Hung, H. C. Lai, and H. P. Feng, 'Characteristics of RF-sputtered thin films of calcium phosphate on titanium dental implants', *Coatings*, vol. 7, no. 8, Aug. 2017, doi: 10.3390/coatings7080126.

[205] N. Ferraa, M. Ouakki, H. El Harmouchi, M. Cherkaoui, and M. Bennani Ziatni, 'Investigation of the inhibition behavior of an octacalcium phosphate as a green

corrosion inhibitor against carbon steel in 3 % NaCl medium', *Inorg Chem Commun*, vol. 157, Nov. 2023, doi: 10.1016/j.inoche.2023.111343.

[206] H. Zeng and W. R. Lace, 'XPS, EDX and FTIR analysis of pulsed laser deposited calcium phosphate bioceramic coatings: the effects of various process parameters', 2000.

[207] L. Zhou, X. Ge, C. Ren, and G. Chen, 'In-situ high temperature XRD and TEM study of the thermal stability and sintering behavior of octacalcium phosphate', *J Alloys Compd*, vol. 778, pp. 72–76, Mar. 2019, doi: 10.1016/j.jallcom.2018.11.124.

[208] N. Ohtsu, S. Hiromoto, M. Yamane, K. Satoh, and M. Tomozawa, 'Chemical and crystallographic characterizations of hydroxyapatite-and octacalcium phosphate-coatings on magnesium synthesized by chemical solution deposition using XPS and XRD', *Surf Coat Technol*, vol. 218, no. 1, pp. 114–118, 2013, doi: 10.1016/j.surfcoat.2012.12.037.

[209] N. Ohtsu, S. Hiromoto, M. Yamane, K. Satoh, and M. Tomozawa, 'Chemical and crystallographic characterizations of hydroxyapatite-and octacalcium phosphate-coatings on magnesium synthesized by chemical solution deposition using XPS and XRD', *Surf Coat Technol*, vol. 218, no. 1, pp. 114–118, 2013, doi: 10.1016/j.surfcoat.2012.12.037.

[210] M. K. Hassan, T. A. Elkhooly, A. S. Elmezayyen, N. El-Wassefy, M. M. Mansour-Gabr, and N. A. Abdel Ghany, 'Enhancement of Adhesion Strength and In-Vivo Evaluation of Electrodeposited Calcium Phosphate/Chitosan Biocoatings on Titanium Substrate', *Surfaces and Interfaces*, vol. 42, Nov. 2023, doi: 10.1016/j.surfin.2023.103475.

[211] D. Horkavcová, B. Plesingerová, A. Helebrant, M. Vojtko, and V. Procházka, 'Adhesion of the Bioactive Layer on Titanium Alloy Substrate by Tape-Test', *Ceramics*, vol. 52, no. 3, pp. 130–138, May 2008.

[212] J. Valli, 'A review of adhesion test methods for thin hard coatings', *Journal of Vacuum Science & Technology A: Vacuum, Surfaces, and Films*, vol. 4, no. 6, pp. 3007–3014, Nov. 1986, doi: 10.1116/1.573616.

[213] 'ASTM F1044-05: Test Method for Shear Testing of Calcium Phosphate Coatings and Metallic Coatings', Dec. 01, 2017, *ASTM International, West Conshohocken, PA*. doi: 10.1520/F1044-05R17E01.

[214] ‘ASTM C1624-22: Test Method for Adhesion Strength and Mechanical Failure Modes of Ceramic Coatings by Quantitative Single Point Scratch Testing’, Mar. 21, 2022, *ASTM International, West Conshohocken, PA*. doi: 10.1520/C1624.

[215] S. T. Gonczy and N. Randall, ‘An ASTM Standard for Quantitative Scratch Adhesion Testing of Thin, Hard Ceramic Coatings’. [Online]. Available: http://www.csm-instruments.com

[216] J. Gao, Y. Su, and Y. X. Qin, ‘Calcium phosphate coatings enhance biocompatibility and degradation resistance of magnesium alloy: Correlating in vitro and in vivo studies’, *Bioact Mater*, vol. 6, no. 5, pp. 1223–1229, May 2021, doi: 10.1016/J.BIOACTMAT.2020.10.024.

[217] S. Hiromoto, M. Inoue, T. Taguchi, M. Yamane, and N. Ohtsu, ‘In vitro and in vivo biocompatibility and corrosion behaviour of a bioabsorbable magnesium alloy coated with octacalcium phosphate and hydroxyapatite’, *Acta Biomater*, vol. 11, no. 1, pp. 520–530, Jan. 2015, doi: 10.1016/j.actbio.2014.09.026.

[218] M. Tomozawa and S. Hiromoto, ‘Microstructure of hydroxyapatite- and octacalcium phosphate-coatings formed on magnesium by a hydrothermal treatment at various pH values’, *Acta Mater*, vol. 59, no. 1, pp. 355–363, Jan. 2011, doi: 10.1016/J.ACTAMAT.2010.09.041.

[219] S. Hiromoto, ‘Self-healing property of hydroxyapatite and octacalcium phosphate coatings on pure magnesium and magnesium alloy’, *Corros Sci*, vol. 100, pp. 284–294, Nov. 2015, doi: 10.1016/j.corsci.2015.08.001.

[220] M. Omasta, B. Hadzima, and C. Farrugia, ‘Evaluation of Octacalcium Phosphate Coating on the Corrosion Resistance of Elektron 21 Magnesium Alloy’, in *Materials Today: Proceedings*, Elsevier Ltd, Jan. 2016, pp. 1108–1113. doi: 10.1016/j.matpr.2016.03.057.

[221] P. C. Banerjee, S. Al-Saadi, L. Choudhary, S. E. Harandi, and R. Singh, ‘Magnesium implants: Prospects and challenges’, Jan. 03, 2019, *MDPI AG*. doi: 10.3390/ma12010136.

[222] R. Willumeit-Römer, ‘The Interface Between Degradable Mg and Tissue’, *JOM*, vol. 71, no. 4, pp. 1447–1455, Apr. 2019, doi: 10.1007/s11837-019-03368-0.

[223] H. K. Uhthoff, P. Poitras, and D. S. Backman, ‘Internal plate fixation of fractures: Short history and recent developments’, 2006, *Springer Japan*. doi: 10.1007/s00776-005-0984-7.

[224] J. Gonzalez, R. Q. Hou, E. P. S. Nidadavolu, R. Willumeit-Römer, and F. Feyerabend, ‘Magnesium degradation under physiological conditions – Best practice’, Jun. 01, 2018, *KeAi Communications Co.* doi: 10.1016/j.bioactmat.2018.01.003.

[225] G. Song, A. Atrens, and D. St John, ‘An hydrogen evolution method for the estimation of the corrosion rate of magnesium alloys’, *TMS Annual Meeting*, no. 51731008, pp. 255–262, 2001, doi: 10.1002/9781118805497.ch44.

[226] B. Wu *et al.*, ‘Effects of friction stir processing and nano-hydroxyapatite on the microstructure, hardness, degradation rate and in-vitro bioactivity of WE43 alloy for biomedical applications’, *Journal of Magnesium and Alloys*, vol. 12, no. 1, pp. 209–224, Jan. 2024, doi: 10.1016/j.jma.2023.10.010.

[227] L. Guo, X. Zhang, Z. Zhang, and Z. Hao, ‘Degradation characteristics of high-purity magnesium implants under single static and cyclic compressive loads in vivo and in vitro’, *Journal of Magnesium and Alloys*, 2025, doi: 10.1016/j.jma.2024.12.014.

[228] J. A. Toque, M. Hamdi, A. Ide-Ektessabi, and I. Sopyan, ‘Effect of the Processing Parameters on the Integrity of Calcium Phosphate Coatings Produced by RF-Magnetron SPUTTERING’, 2009. [Online]. Available: www.worldscientific.com

[229] K. K. A. Mosas, A. R. Chandrasekar, A. Dasan, A. Pakseresht, and D. Galusek, ‘Recent Advancements in Materials and Coatings for Biomedical Implants’, May 01, 2022, *MDPI*. doi: 10.3390/gels8050323.

Appendix

Design of Experiment Solutions

	Temp (°C)	pH	Conc. (mol/L)	Flow Rate (mL/min)	Digestion Time (hr)	Surface Roughness (µm)	%OCP	Ca:P Ratio	Coating Thickness	Desirability
1	69.668	6.950	0.060	5.289	1.000	0.280	81.098	1.330	22.775	0.948
2	69.998	6.828	0.060	5.796	1.000	0.293	80.910	1.328	20.716	0.947
3	70.000	6.922	0.060	5.420	0.977	0.326	80.711	1.330	21.855	0.946
4	68.224	7.000	0.060	4.885	1.000	0.280	80.246	1.330	23.921	0.945
5	69.745	6.753	0.060	6.000	0.911	0.280	79.730	1.323	18.423	0.941
6	70.000	6.775	0.060	5.809	0.878	0.280	79.299	1.330	18.511	0.941
7	67.211	7.000	0.060	4.760	0.994	0.368	79.103	1.330	24.030	0.940
8	68.843	6.726	0.060	5.857	0.923	0.280	78.997	1.330	19.044	0.940
9	69.996	6.719	0.058	5.790	1.000	0.363	78.901	1.330	18.891	0.939
10	69.995	6.763	0.060	5.756	0.798	0.291	78.345	1.330	17.670	0.937
11	69.970	7.000	0.060	5.179	1.000	0.831	78.070	1.330	21.605	0.936
12	67.394	6.757	0.060	5.457	1.000	0.404	78.025	1.330	21.534	0.936
13	69.562	6.862	0.057	4.669	1.000	0.301	77.847	1.330	21.735	0.935
14	65.915	6.815	0.060	5.040	1.000	0.314	77.811	1.330	23.060	0.935

15	69.349	6.769	0.057	4.954	0.995	0.280	77.530	1.330	20.655	0.934
16	69.998	6.999	0.056	4.244	1.000	0.371	77.795	1.322	22.298	0.933
17	69.711	6.945	0.056	4.303	1.000	0.395	77.225	1.330	22.197	0.933
18	69.235	6.989	0.060	4.714	0.672	0.282	77.193	1.330	19.874	0.932
19	70.000	6.991	0.060	4.681	0.634	0.280	77.059	1.327	19.503	0.931
20	62.118	7.000	0.060	4.211	1.000	0.323	76.627	1.331	25.596	0.930
21	70.000	6.638	0.060	5.976	0.674	0.280	76.449	1.330	14.753	0.929
22	61.489	6.992	0.059	3.956	0.999	0.280	75.738	1.330	25.375	0.927
23	60.679	7.000	0.060	4.187	0.926	0.280	75.700	1.330	24.496	0.926
24	63.610	6.984	0.060	4.399	1.000	0.650	75.461	1.330	24.631	0.925
25	69.250	7.000	0.058	4.843	1.000	1.139	74.943	1.330	20.423	0.923
26	70.000	6.986	0.060	5.738	1.000	1.532	75.017	1.327	19.640	0.923
27	69.980	6.996	0.057	4.033	0.603	0.280	74.498	1.330	18.832	0.922
28	70.000	6.605	0.060	5.563	0.573	0.280	74.369	1.330	14.759	0.921
29	69.923	7.000	0.059	5.550	1.000	1.582	74.292	1.330	19.301	0.921
30	70.000	6.906	0.060	4.542	0.532	0.297	74.947	1.317	18.465	0.920
31	70.000	6.861	0.060	6.000	0.840	0.484	79.004	1.245	17.210	0.919
32	69.069	7.000	0.056	3.933	0.667	0.345	73.936	1.330	18.937	0.919
33	69.944	7.000	0.060	4.479	0.627	0.773	73.788	1.330	18.615	0.919

34	64.958	6.868	0.059	4.458	0.645	0.280	73.490	1.330	18.804	0.917
35	56.027	7.000	0.060	3.761	0.955	0.312	73.352	1.330	25.803	0.917
36	70.000	6.976	0.060	3.824	0.425	0.315	73.179	1.330	19.649	0.916
37	69.582	6.989	0.050	2.635	1.000	0.280	73.170	1.330	24.082	0.916
38	59.181	7.000	0.056	3.397	0.929	0.280	72.544	1.330	23.835	0.913
39	53.910	7.000	0.060	3.421	0.999	0.316	72.308	1.330	27.330	0.912
40	61.795	6.992	0.060	4.174	0.581	0.380	72.158	1.330	18.980	0.912
41	69.693	7.000	0.060	3.477	0.357	0.280	72.144	1.330	19.912	0.912
42	68.981	6.403	0.058	6.000	0.590	0.363	71.947	1.330	11.381	0.911
43	60.892	6.562	0.060	5.235	1.000	0.280	74.182	1.288	21.333	0.910
44	70.000	6.378	0.059	6.000	0.479	0.281	71.767	1.330	10.570	0.910
45	68.471	6.372	0.060	6.000	0.514	0.307	71.728	1.330	11.811	0.910
46	69.999	6.872	0.050	2.376	1.000	0.308	71.597	1.330	25.195	0.909
47	56.911	7.000	0.060	4.108	0.608	0.280	71.294	1.330	19.069	0.908
48	37.864	6.983	0.060	5.573	1.000	0.280	70.876	1.330	15.602	0.906
49	54.015	6.823	0.059	3.617	1.000	0.280	70.839	1.330	25.313	0.906
50	62.298	7.000	0.054	3.362	0.773	0.367	70.695	1.330	19.753	0.906
51	69.999	6.995	0.058	3.058	0.333	0.280	70.564	1.330	19.936	0.905
52	70.000	6.895	0.050	2.095	1.000	0.376	70.691	1.331	25.335	0.905

53	56.393	6.997	0.060	4.083	0.550	0.280	70.497	1.330	18.153	0.905
54	61.769	7.000	0.057	3.631	1.000	1.028	70.457	1.332	23.250	0.904
55	70.000	6.751	0.051	3.479	1.000	0.280	72.924	1.275	21.470	0.902
56	70.000	6.788	0.052	2.508	1.000	0.591	69.813	1.330	23.833	0.902
57	69.958	6.323	0.060	5.230	0.433	0.280	69.759	1.330	14.078	0.902
58	55.416	7.000	0.060	3.360	1.000	0.606	71.002	1.343	27.336	0.901
59	62.215	6.944	0.060	4.146	0.711	1.007	69.331	1.330	20.071	0.900
60	63.013	7.000	0.058	3.799	0.568	0.706	69.288	1.330	17.912	0.900
61	61.122	6.999	0.060	3.817	0.301	0.280	69.349	1.323	16.176	0.898
62	70.000	6.970	0.048	2.267	0.695	0.280	68.866	1.330	21.152	0.898
63	70.000	6.999	0.053	2.753	0.360	0.280	68.845	1.330	18.818	0.898
64	38.821	6.901	0.060	5.997	0.823	0.421	68.737	1.330	12.240	0.897
65	69.998	6.622	0.053	2.642	0.778	0.280	68.729	1.330	24.089	0.897
66	58.866	6.999	0.052	2.000	1.000	0.311	68.687	1.330	25.872	0.897
67	64.410	6.414	0.060	6.000	1.000	1.432	68.606	1.330	19.786	0.897
68	54.332	7.000	0.060	4.213	0.530	0.282	69.856	1.305	16.904	0.896
69	69.932	6.976	0.060	4.688	0.631	1.722	68.376	1.330	15.181	0.896
70	67.693	7.000	0.056	4.673	1.000	2.007	68.326	1.330	16.793	0.895
71	69.968	6.864	0.060	2.002	0.339	0.280	68.058	1.330	26.000	0.894

72	70.000	5.977	0.046	6.000	0.996	0.280	68.454	1.321	7.088	0.894
73	48.646	6.997	0.060	2.188	0.951	0.280	67.888	1.330	30.753	0.893
74	39.299	6.714	0.060	5.915	0.832	0.280	67.858	1.330	11.789	0.893
75	70.000	6.559	0.054	2.002	0.827	0.283	67.725	1.330	28.258	0.893
76	39.277	6.600	0.060	5.568	1.000	0.280	67.653	1.330	15.893	0.892
77	70.000	6.485	0.057	2.739	0.638	0.280	67.561	1.330	25.010	0.892
78	69.239	7.000	0.059	2.000	0.203	0.281	67.460	1.330	22.898	0.892
79	47.830	6.931	0.060	2.177	0.995	0.330	67.109	1.330	31.416	0.890
80	70.000	6.045	0.050	4.521	1.000	0.378	67.023	1.330	15.717	0.890
81	70.000	6.177	0.052	6.000	0.600	0.600	66.983	1.330	7.371	0.889
82	69.999	6.640	0.060	5.732	0.628	1.795	66.650	1.330	13.467	0.888
83	65.716	6.929	0.060	6.000	0.947	2.607	66.625	1.330	19.392	0.888
84	40.141	7.000	0.058	5.995	0.403	0.280	66.605	1.330	3.617	0.888
85	68.528	7.000	0.047	2.095	1.000	0.582	69.130	1.280	21.626	0.887
86	69.884	7.000	0.049	2.564	1.000	1.048	68.313	1.294	18.206	0.887
87	67.263	6.999	0.056	4.798	1.000	2.336	66.285	1.330	15.557	0.886
88	68.114	7.000	0.044	2.000	0.584	0.285	65.630	1.329	19.132	0.883
89	39.516	6.775	0.060	4.135	0.871	0.280	65.540	1.330	19.849	0.883
90	45.413	6.828	0.060	2.000	0.999	0.282	65.258	1.330	31.856	0.882

91	38.050	6.994	0.054	5.518	0.591	0.280	65.104	1.330	4.323	0.881
92	44.591	6.906	0.060	3.912	0.673	0.283	66.310	1.301	18.602	0.880
93	69.996	7.000	0.055	5.825	1.000	3.007	64.829	1.330	12.495	0.880
94	58.760	7.000	0.054	2.388	1.000	1.286	64.362	1.330	22.000	0.878
95	66.720	7.000	0.044	2.597	0.354	0.280	64.156	1.330	14.838	0.877
96	67.185	6.265	0.060	2.002	0.647	0.280	64.147	1.330	30.380	0.877
97	70.000	7.000	0.051	2.401	0.623	1.279	63.988	1.330	14.791	0.876
98	44.993	6.236	0.060	5.217	1.000	0.280	65.437	1.299	18.380	0.876
99	49.584	6.896	0.055	4.048	0.367	0.280	63.877	1.330	10.841	0.875
100	61.563	7.000	0.051	3.557	0.052	0.280	63.839	1.330	9.305	0.875

Design of Experiment Factors

Factor	Name	Level	Low Level	High Level	Std. Dev.	Coding
A	Temperature	69.67	37.00	70.00	0.0000	Actual
B	pH	6.95	4.00	7.00	0.0000	Actual
C	Concentration	0.0600	0.0200	0.0600	0.0000	Actual
D	Flow Rate	5.29	2.00	6.00	0.0000	Actual
E	Digestion Time	0.9999	0.0000	1.0000	0.0000	Actual
F	Surface Roughness	0.2800	0.2800	3.50	0.0000	Actual

Design of Experiment Point Prediction

Solution 1 of 100 Response	Predicted Mean	Predicted Median	Observed	Std Dev	SE Mean	95% CI low for Mean	95% CI high for Mean	95% TI low for 99% Pop	95% TI high for 99% Pop
%OCP	81.0981	81.0981		25.3743	12.4525	56.0017	106.194	-19.2616	181.458
Ca:P Ratio	1.33	1.33		0.0850691	0.14587	1.00498	1.65502	0.664392	1.99561
Coating Thickness	22.7749	22.7749		8.60772	6.21233	10.2288	35.321	-14.8386	60.3884

Design of Experiment Build Information

File Version	13.0.5.0		
Study Type	Response Surface	Subtype	Randomized
Design Type	Box-Behnken	Runs	51.00
Design Model	Quadratic	Blocks	No Blocks
Build Time (ms)	8.00		

Factor	Name	Units	Type	SubType	Minimum	Maximum	Coded Low	Coded High	Mean	Std. Dev.
A	Temperature	C	Numeric	Continuous	37.00	70.00	-1 ↔ 37.00	+1 ↔ 70.00	53.50	11.43
B	pH		Numeric	Continuous	4.00	7.00	-1 ↔ 4.00	+1 ↔ 7.00	5.50	1.04
C	Concentration	mol/L	Numeric	Continuous	0.0200	0.0600	-1 ↔ 0.02	+1 ↔ 0.06	0.0400	0.0139
D	Flow Rate	ml/min	Numeric	Continuous	2.00	6.00	-1 ↔ 2.00	+1 ↔ 6.00	4.00	1.39
E	Digestion Time	Hour	Numeric	Continuous	0.0000	1.0000	-1 ↔ 0.00	+1 ↔ 1.00	0.5000	0.3464
F	Surface Roughness	um	Numeric	Continuous	0.2800	3.50	-1 ↔ 0.28	+1 ↔ 3.50	1.89	1.12

Response	Name	Units	Observations	Minimum	Maximum	Mean	Std. Dev.	Ratio
R1	%OCP		51.00	0	95.2	38.29	27.66	N/A
R2	Ca:P Ratio		51.00	0	1.4	0.9581	0.3003	N/A
R3	Coating Thickness	um	51.00	0.537	52.7703	9.51	10.44	98.27